The Dissertation Committee for Erik Michael Anciaux certifies that this is the approved version of the following dissertation:

A Complex Atom Lens

Committee:

Mark G. Raizen, Supervisor

Alex Demkov

Greg Sitz

Xiaoqin (Elaine) Li

Ed Yu

A Complex Atom Lens

by

Erik Michael Anciaux

Dissertation
Presented to the Faculty of the Graduate School of
The University of Texas at Austin
in Partial Fulfillment
of the Requirements
for the degree of
Doctor of Philosophy

The University of Texas at Austin
May, 2018

For Mom and Dad.

Acknowledgements

First, I would like to thank my adviser, Dr. Mark Raizen. Mark is a brilliant scientist and an even better person. Mark has a penchant for grand ideas that are off the beaten path of science. I admire his pursuit of challenging and meaningful problems that have been overlooked by the greater scientific community. He has a keen eye for identifying various hurdles that must be overcome and the experience to know how to overcome them. Beyond his impeccable scientific acumen, what makes Mark stand out is his understanding of the non-scientific aspects of being a scientist. Mark truly cares about his students, and is driven to make sure that we succeed both as scientists and as human beings. He is currently working on growing The Pointsman Foundation, a non-profit foundation dedicated to producing medical isotopes necessary for cancer therapy. From his passion for using science for the betterment of humanity to his genuine care for the people around him, Dr. Mark Raizen represents everything that is right about science and I could not have asked for a better Ph.D. adviser.

This project would not have been possible without Dr Jamie Gardner. Jamie was the senior graduate student on the focusing project when I arrived at UT and was my lab partner for three and a half years until his graduation. Jaime was an extremely gifted physicist with a deep understanding of experimental methods as well as the overarching mission of the project. I will be forever grateful for his scientific training, his patience, and his friendship. Nearly all of the scientific skills I have learned in graduate school from ultra-high vacuum to laser locking to figuring out the correct combination of screw tightening, nozzle opening parameters, and swearing in other languages to operate a supersonic nozzle, I learned because of Jamie Gardner., Over the course of many passionate discussions regarding how best to overcome obstacles in our experiment, analyzing fundamentally non-scientific aspects of life using scientific viewpoints and jargon, and arguing about politics (mostly arguing about how much we agree with each other,) Jamies friendship made the lab a fun and exciting place to work. For three and a half years, I didnt have to go to work in the morning, I had the privilege of experimenting with magnets and lasers with my best friend.

Georgios Stratis (Γ$) worked on the microscope aspect of the experiment. Despite a very challenging project and often broken equipment, Georgios has persevered and developed a means to analyze the energy spectra of electrons produced through metastable atom electron spectroscopy, a piece of technology that will be combined

with the complex atom lens to form a true atom microscope. Georgios has an incredible work ethic that will make him successful in anything he tries to do. He has been a great friend and holds the rare distinction of being (slightly) to my political left. Whenever I have needed anything, whether it be scientific help or emotional support, Georgios has always been there. He is one of the most kind hearted and reliable people I have ever met and for anyone who has ever known him, our lives are better because of Georgios Stratis.

Dr. Rodrigo Castillo Garza was a postdoc on the focusing project for the first two years of my graduate career. Rodrigo brought an aura of optimism to the experiment, even when the project was at its points of greatest despair. He never gave up hope that the project would be eventually be successful, despite times of overwhelming evidence to the contrary. When I was an incoming student, he took the time to teach me many areas of atomic physics as well as how to perform various aspects of research.

Zoe de Beurs is an undergraduate student who has worked on the atomic microscope project for one year. She joined the group as a first year undergraduate and made immediate contributions to the project, designing and building Helmholtz coils for optical pumping as well as a controller for the electron analyzer. Zoe is an incredibly talented and motivated scientist and has already presented her research at multiple conferences. As a person, Zoe cares deeply for social equality, especially within the sciences and has been incredibly active in making a more equitable science community through her work with Natural Sciences Council and 314 action.

Igal Bucay has had the desk next to mine since he joined the lab four years ago. He has made incredible progress on his isotope separation project in a relatively short time. He has been an incredibly helpful resource for myself and the rest of the lab, providing expertise on a wide range of areas of physics. He has been a great friend and labmate with a very positive approach to science as well as life. I am grateful that we share our similar perspectives on academic research and science as a whole. Igal is an incredibly diligent worker, but also knows how to make scientific research fun. We have shared many jokes over the years, each one more hilarious than the last.

Jordan Zesch recently joined the atomic lens project and has quickly picked up the mechanics of the experiment.

Dr. Ahmed Helal is a postdoc on the isotope separation project and has brought

a plethora of expertise in optics to the experiment and to the lab.

Kevin Melin, Yu Lu, Logan Hillberry, Yi Xu, Dr. Pavel Nagonykh, and Dr. Harry Ha are working on the magnetic slowing experiment and have made great progress slowing and cooling a beam of lithium atoms. Kevin is the only other student whose time has overlapped completely with my own and has been an extremely helpful resource for troubleshooting electronics. In addition to having a hilarious sense of humor, Yu is a gifted scientist and has helped us with many electronics issue. Logan and I have shared many great conversations regarding respective challenges in our experiments as well as challenges navigating graduate school, usually over Cabo Bobs burritos. Yi worked on the atomic focusing experiment for several months and built an interferometer for calibration of our nanoscale atom detection system. Pavel and Harry both bring a plethora of knowledge regarding the field of atomic physics and have been great resources for discussions of current developments in the field.

Dr. Jianyong Mo, Dr. Simon Kheifets, and Dr. Akarsh Simha were graduate students when I joined the lab and built an experiment analyzing Brownian motion, achieving remarkable results.

Dr. Tom Mazur and Dr. Bruce Klappauf were a graduate student and research scientist respectively, who designed and built MAGIS, a means of isotope separation that will serve as the backbone for The Pointsman Foundation.

Karl Burkhardt, Isaac Chavez, and Alina Blinova all earned master's degrees during my early years in the Raizen lab. Together, they laid the foundation for the magnetic slowing experiment.

David Reigler, Lukas Gradl, and Melina Armer were visiting students from the University of Würzberg and worked on various research projects in the Raizen Lab.

Whitney Seifert, Tharon Morrison, Daniel Raimi-Zlatic, David Dunsky, Will Plusnick, Will Yager, Jimmy Kennington, Salman Sarwar, Marie Schoelch, Ravi Goparaju, Alec Eickbusch have performed undergraduate level research in our group, while Beck Goodloe performed research as a high school student.

The Raizen lab, nor the rest of the Center for Nonlinear Dynamics, would not be able to function without Olga Vera. Olga handles our purchasing, payroll, travel, office supplies, and just about everything else that needs to happen for the CNLD to run smoothly.

A tremendous resource for our lab and our department has been the machine shop on the third floor. They have built many parts for us over the years, often with

difficult and precise requirements. The shop manager, Allan Schroeder, has been great to work with as he has helped us gain crucial understanding of what can and cant be machined and how we can improve our machine drawings accordingly. The student shop manager, Jack Clifford, has been an incredible teacher, teaching hundreds if not thousands of students over the years on how to operate the equipment in the machine shop. The cryo shop manager, Ed Baez, has been a helpful resource providing liquid nitrogen and servicing vacuum equipment. Danny Boyd, Herb Boehl, Jeff Boney, Jay Campbell, Terry Cole, Richard Goodwin, Bryan McDonald, George Sandefur, Kenny Schneider, and Flint Flisher have all done amazing work in the machine shop.

I would be remiss if I did not thank my Ph.D. committee, Dr. Alex Demkov, Dr. Greg Sitz, Dr. Elaine Li, and Dr. Ed Yu for reading this entire dissertation, for attending my thesis defense and for agreeing to serve on my committee.

I would also like to thank my friends in Austin both inside and outside the physics community for making my time in Austin such a memorable experience. From Democratic campaigns to Monday Movie Madness to Scotch Nights to three kickball championships, I am incredibly lucky to have shared so many great memories with so many great people.

Lastly, I would like to thank my parents for their unconditional love and support. They have instilled in me the values of kindness, passion for learning, and dedication and have supported me through every step of my journey from birth until now. I know that they will continue to support me as I enter the next phase of my life and beyond. I am so eternally grateful for everything they have done for me and could not even imagine having two better role models as parents.

A Complex Atom Lens

Erik Michael Anciaux, Ph.D.
The University of Texas at Austin, 2018

Supervisor: Mark G. Raizen

This dissertation presents progress on an atomic beam brightening and focusing experiment that has been shown to create a beam with higher brightness and greater resolution than that of any previous atomic focusing experiment. Our method of beam brightening relies upon using a permanent magnetic hexapole as a lens in conjunction with transverse laser cooling to focus and collimate a supersonic beam of metastable neon atoms. We then use an adjustable electromagnetic hexapole as a lens to focus the brightened atomic beam.

Neutral atom beams have long been used as a tool to spectroscopically probe two dimensional surfaces, however the lack of a means to create bright, high-resolution neutral atom beams has limited their utility as a nanoscale resolution probing mechanism. While optical and electron microscopy have been the workhorses of microscopy for decades, we believe that our scheme for beam brightening and focusing will unleash the promise of neutral atom microscopy.

Our scheme of beam brightening and focusing can be repeated in series and reveals a pathway to true high density nanoscale neutral atom focusing. Simulations suggest that when combined with aberration correction, our scheme will be able to produce an atomic beam with sufficient brightness and resolution to be useful as a surface sensitive nanoscale probe.

Contents

List of Figures

Chapter One: Introduction

Neutral atom beams have been a useful tool for many areas of scientific research beginning with the famous Stern-Gerlach experiment, verifying the quantization of angular momentum [1]. Since, neutral atom beams have been used as a mechanism to load atoms in stationary traps [2], as well as a tool for studying cold chemistry [3] among many other uses including but not limited to isotope separation [4] and atom interferometry [5].

While advances in electron beam and photon beam technologies have allowed for advancements in e-beam lithography [6, 7] and XUV photolithography [8, 9], atom beams have also been proposed as a mechanism for nanoscale fabrication [10, 11, 12, 13]. E-beam lithography and XUV photolithography both rely upon damaging a resist prior to etching or depositing material onto the damaged region. In principle atomic beams could be used to directly deposit material onto a sample, potentially eliminating the need for a separate etching and resist removal process.

Atom beams have also been used as a probing mechanism, analogously to electron beams and light beams in scanning electron microscopy and optical microscopy [14, 15]. A potential benefit of using atoms as a probe is their short deBroglie wavelength and relatively low kinetic energies. This lowers the fundamental spatial resolution limit and allows for greater surface sensitivity than available from traditional e-beam and optical methods.

Metastable atom electron spectroscopy in particular is an exciting probing mechanism using metastable atoms to analyze surface states of two dimensional structures [16, 17]. While it has shown great promise as a tool for spectroscopy, there is currently no means of creating a beam of metastable atoms sufficiently small and dense to realize the promise of metastable atom electron spectroscopy at the local level.

Three parameters that describe atomic beams are resolution, density, and brightness. The resolution of a beam travelling along the z axis is the standard deviation of the distribution of atomic positions along an axis perpendicular to the direction of travel, σ_x. The density is defined as $\rho \equiv \frac{2I}{\sigma_x \sigma_y}$ where I is the atom current (atoms per second). The brightness is defined as $B \equiv \frac{2I}{\pi \epsilon_x \epsilon_y}$ where ϵ_x and ϵ_y are the emittances in the x and y directions respectively. $\epsilon_x = \sqrt{\sigma_x^2 \sigma_{x'}^2 - \sigma_{xx'}^2}$ where $\sigma_{x'}$ is the standard de-

viation of atom divergence angles along the x direction. A major goal of atomic beam experiments is to optimize one of resolution, density or brightness without sacrificing the others.

At present time, a major roadblock preventing atom beams from being a useful tool for nanofabrication and microscopy is the lack of a method for creating a bright, dense atomic beam with nanoscale resolution. Further development of atom optics techniques are necessary to create an atom beam that can truly realize the promise of atomic beam nanofabrication and neutral atom microscopy.

1.1 Atom lenses

Over the past century, several tools have been developed for the manipulation and control of atomic motion analogous to optical elements for control of light including atomic mirrors and lenses [18, 19].

The development of atom lenses in particular has been a great challenge for atomic physicists. Many techniques have been tried including passive lenses based on the camera obscura effect [20, 21] or matter wave diffraction from Fresnel zone plates [22, 23] and active lenses based on optical [24, 25] and magnetic forces on neutral atoms.

Each type of lens comes with its own advantages and disadvantages when it comes to resolution, density, and brightness. Certain lenses can also image two dimensional shapes, while others are limited to specific patterns or focusing to a point or a line.

A major challenge for any atom lens experiment is the problem of aberration correction. Often, the types of aberrations found in atom lenses are analogous to the types of aberrations found in optical lenses including geometric aberration and chromatic aberration.

1.1.1 Pinhole lens

An atom pinhole lens is exactly analogous to an optical pinhole camera. In both cases, a beam passes through an object plane prior to passing through a much smaller pinhole. The resulting image can be calculated using simple ray tracing methods.

The image will be inverted and demagnified by a factor $M = \frac{l}{L}$. The resolution will be on the order of the size of the pinhole, however the flux is severely limited due

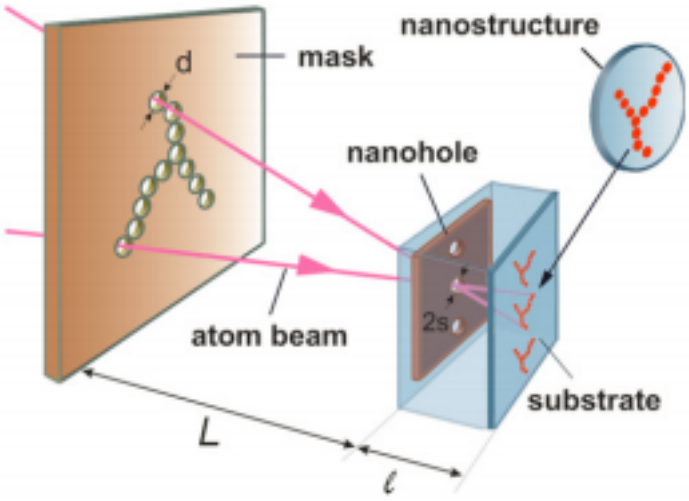

Figure 1.1: A diagram of the beamline of a pinhole lens. The object plane consists of a thin film, with a specific pattern cut out. A portion of the beam then propagates through the pinhole lens toward a substrate that serves as an image plane. Source: Melentiev, et al. [20]

to the size of the pinhole and the relatively few atoms that can be passed through a pinhole without an active focusing element. The focusing ability is also fundamentally limited by diffraction inherent in the atomic beam. These barriers limit the utility of pinhole lenses in atom nanofabrication and microscopy applications. Pinhole lenses are not limited to specific geometries and can image arbitrary two dimensional shapes. A diagram of a pinhole atom lens is shown in Figure 1.1.

1.1.2 Fresnel zone plates

A second type of passive lens, a Fresnel zone plate, has been used as a focusing element. Both optical and atomic Fresnel zone plate imaging rely on diffraction to achieve a small spot size. When considering wave phenomena of massive particles like atoms, we consider the atom to have wavelike properties according to its deBroglie wavelength. $\lambda_{\mathrm{dB}} = \frac{h}{p}$ where h is Planck's constant and p is the momentum of the atom. A zone plate consists of a series of alternating opaque and transmissive rings designed such that waves that diffract from the zone boundaries will constructively interfere at a point downstream on the axis of the zone plate. The zero order section is opaque, thus blocking the densest portion of the beam.

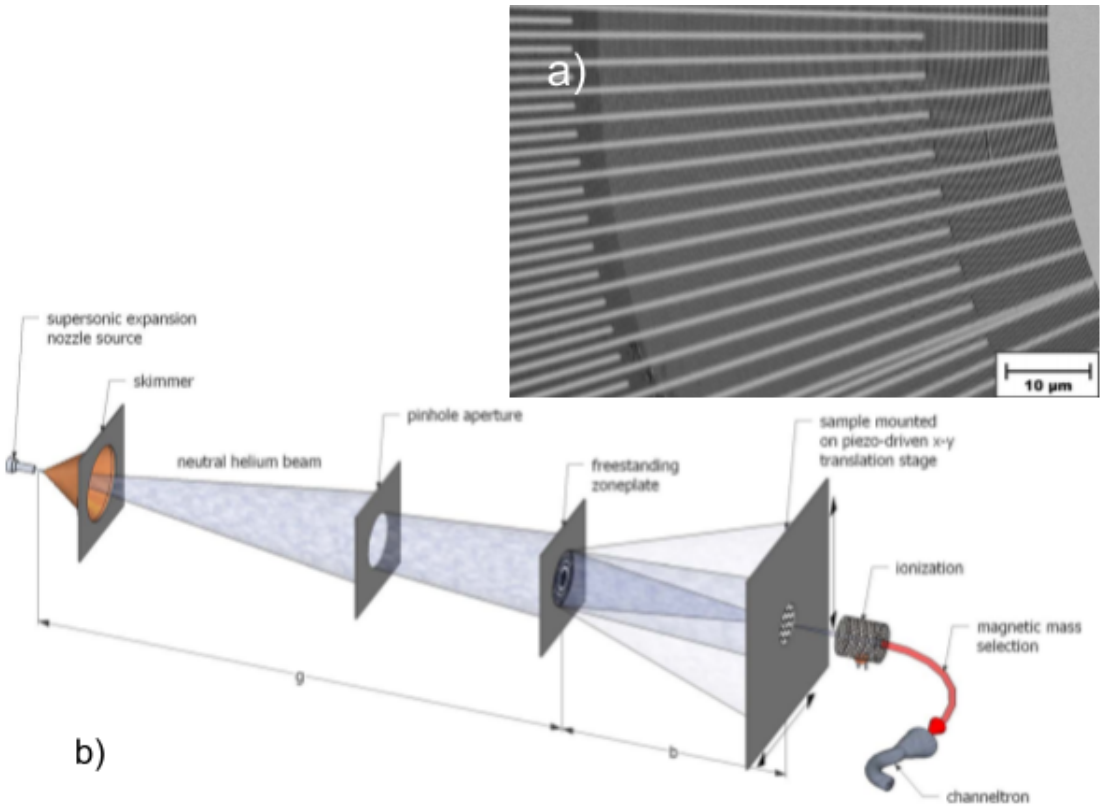

Figure 1.2: a) A close up image of a plate used in Fresnel zone plate imaging. The central opaque zone is the large region in the top right of the image. The radial opaque regions provide structural support for the sub micron width freestanding zones. b)A diagram of a method of Fresnel zone plate imaging A collimated supersonic beam partially passes through a Fresnel zone plate. Portions of the beam passing through transmissive zones will diffract and constructively interfere at a central point. Source: [22]

.

The effectiveness of Fresnel zone plate imaging is limited by the loss in flux due to blocking the brightest portion of the beam. The width of the central peak of the image scales inversely with the area of the central opaque zone, requiring further tradeoffs between beam density and flux. As the beam has finite temperature, different atoms will have different momenta and will thus have different deBroglie wavelengths. This will cause different atoms to come into focus at different positions, an effect analogous to chromatic aberration. A recent experiment has shown focusing down to a spot size of 4 µm however there is no obvious mechanism to reduce chromatic aberration for

true nanoscale focusing[23]. Fresnel zone plates can be used to image two dimensional objects. A cutout of a Fresnel zone plate and a diagram for the beamline of Fresnel zone plate imaging are shown in Figure 1.2.

1.1.3 Standing light waves

Most optical focusing elements rely on matter to focus beams of light. Standing wave focusing relies on standing waves of light to focus beams of atoms. A standing light wave can be produced with a monochromatic source and optical cavity. If the cavity is aligned along the x-axis, the electric field will be up to phase factors and direction $E = E_0(y)\cos(kx)\cos(\omega t)$, where k is the wavenumber and ω is the angular frequency. The intensity will therefore be given by $I \propto \cos^2(kx)$ If the standing wave is slightly detuned from the resonance frequency of a two level atomic transition, the potential energy of atoms in the standing wave will be proportional to the intensity of the beam. Atoms moving transversely to the standing wave will feel a force proportional to the derivative of the intensity, $F_x \propto -\frac{\partial}{\partial x}\cos^2(kx)$. Up to a phase factor this force is $F_x \propto -\sin(2kx)$. For blue detuned light, this force will be towards the anti-nodes of the standing wave and for red detuned light, this force will be towards the nodes of the standing wave. Atoms within an intensity period of the standing wave will be focused towards a focal line parallel to the y axis downstream from the standing wave.

The sinusoidal focusing force $F_x \propto -\sin(2kx)$ matches the ideal harmonic focusing force $F_x \propto -x$ to first order, however far from the nodes (for red detuned light) or antinodes (for blue detuned light) the first order approximation breaks down, causing an aberration analogous to geometric aberration in optical imaging. It also has no means of accounting for chromatic aberration as the focal plane will be dependent on the velocity of the atoms and will not be the same for all atoms. As no part of the beam is blocked, standing wave focusing does not suffer from the problem of lack of flux, however it is limited to focusing only periodic patterns and cannot directly image a two dimensional object. A cartoon of standing wave atom focusing is shown in Figure 1.3.

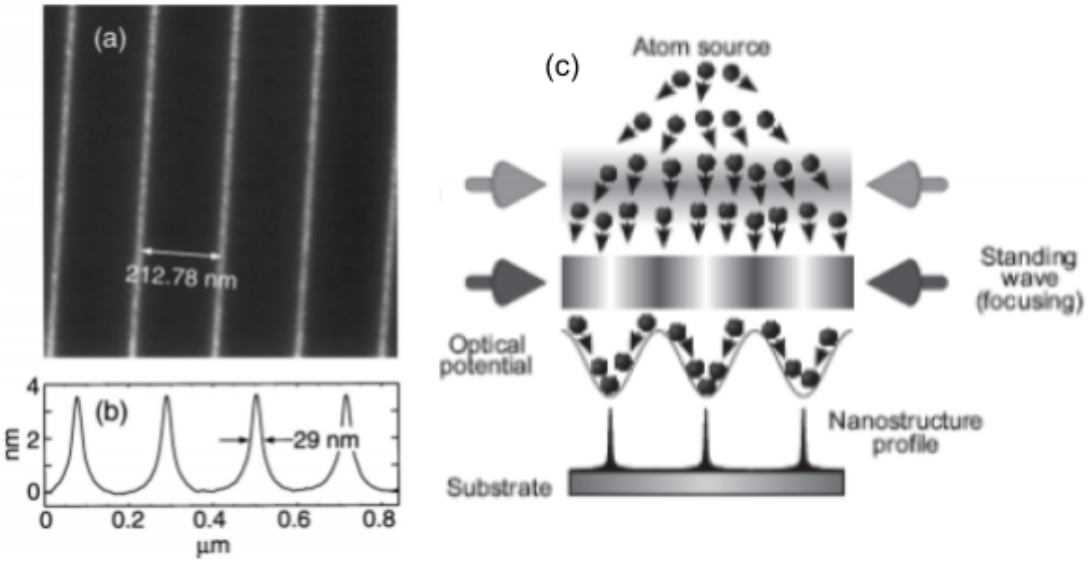

Figure 1.3: a) Lines of chromium atoms deposited onto a substrate from standing wave atom nanofabrication. b) A quantitative measurement of the of chromium deposition onto a substrate. Source: Anderson et al. [26] c) A cartoon of the beamline a standing wave atom nanofabrication experiment. Atoms inside the standing wave feel a potential well and a focusing force toward lines on a focal plane downstream from the optical cavity. Source: Zhang et al. [27]

1.1.4 Permanent magnetic hexapole

A permanent magnetic hexapole is a cylindrical device with a cross section consisting of six magnetic sections, with alternating in-out-in-out-in-out magnetization and a central bore along the axis of an atomic beam. Inside the central bore of the hexapole, the magnitude of the magnetic field increases with the square of the distance from the axis. On low field seeking atoms, this causes a harmonic force field $F_\rho \propto -\rho$, which is the ideal field profile for focusing and imaging. Magnetic hexapoles have long been proposed as a means for focusing beams of neutral atoms [12, 28, 29]. A hexapole cross section built by Kaenders et al. is shown in Figure 1.4.

Kaenders et al. developed a means of true imaging of a complex two dimensional shape using a permanent magnetic hexapole as a lens to image a beam of cesium atoms. Their technique also employs a counterpropagating slowing laser that reduces the velocity spread of their thermal atomic beam, thus reducing but not eliminating chromatic aberrations. While their magnification factor was of order of unity and the

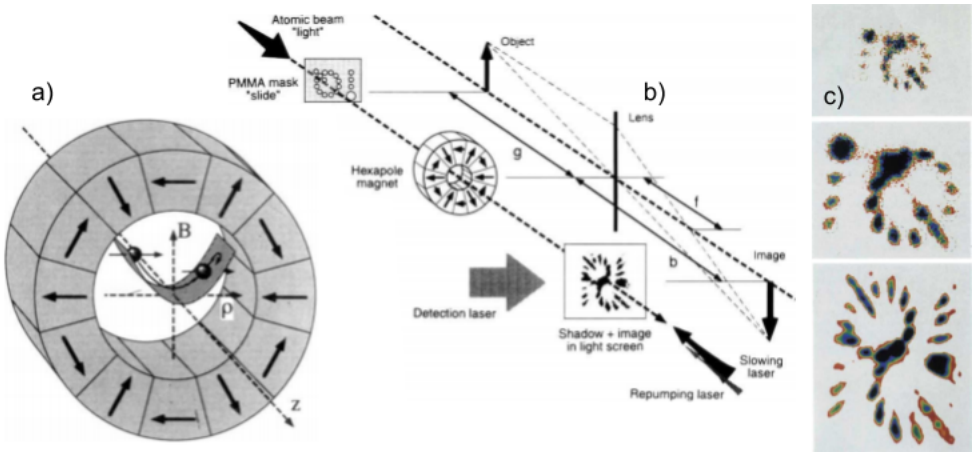

Figure 1.4: a) The orientation of magnets used in a permanent magnetic hexapole lens in an experiment done by Kaenders et al. [28]. b) A diagram of the beamline used in the Kaenders experiment. c) The resulting image plane showing inversion and reconstruction of the original object.

resolution of 200 µm, their method shows promise in both imaging a two dimensional object and focusing a beam to a single spot.

A decade later, Chaustowski et al.[30] developed a similar method of atom focusing using a permanent magnetic hexapole to focus a beam of metastable helium atoms to a small spot. This experiment yielded $3.3 \times 10^{11}\,\mathrm{cm}^{-2}\,\mathrm{s}^{-1}$ with a spot size on the order of 1 mm. The detected images are shown in Figure 1.5.

While permanent magnetic lenses have yet to achieve the small feature sizes demonstrated by standing light wave focusing, their ability to image complex patterns and focus beams to a single spot give a much more promising starting point for future atom lens development. Permanent magnetic lenses are still subject to chromatic aberrations as atoms with different momenta will be focused to different image planes, while geometric aberrations persist as atoms will feel a non-ideal focusing force due to the fringing magnetic fields through which they pass upon entering and exiting the bore of the hexapole.

1.1.5 Pulsed magnetic hexapole

In 2013, our group proposed a novel method for neutral atom focusing relying on a pulsed, tapered, electromagnetic hexapole lens[31]. Our method attempts to elim-

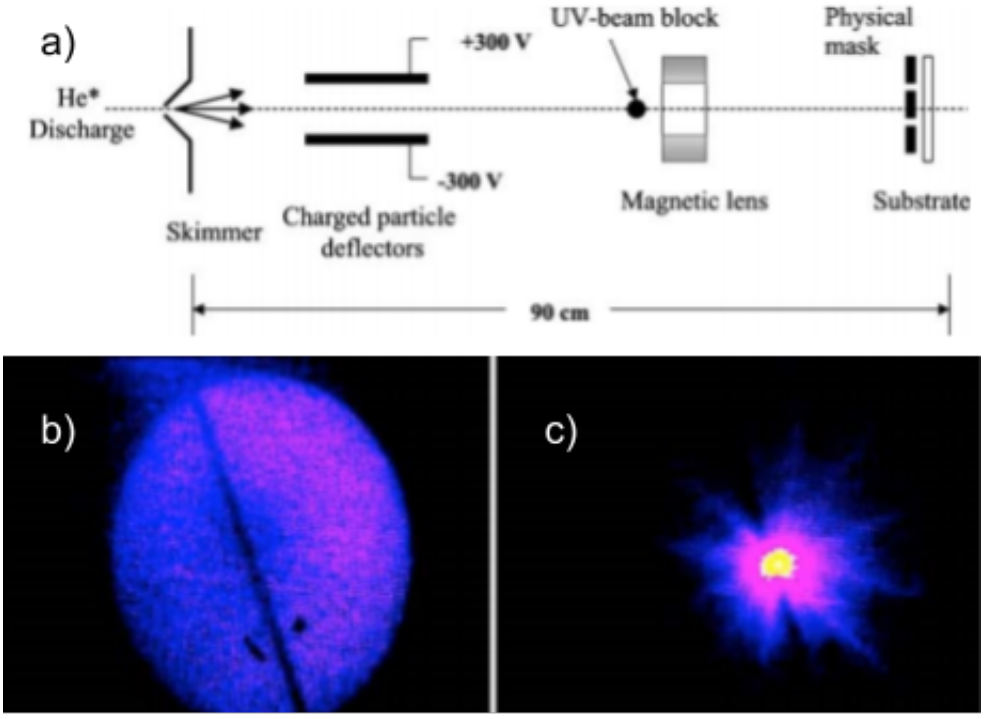

Figure 1.5: a) A diagram of the beamline used in the experiment done by Chaustowski et al. [30] b) A microchannel plate image of an unfocused beam. c) A microchannel plate image of a beam of metastable helium focused by a permanent magnetic lens.

inate geometric aberrations inherent in permanent magnetic lenses by pulsing the magnetic lens on after the atomic beam has entered the bore of the hexapole and pulsing the lens off prior to the beam exiting from the hexapole. Simulations also show that we can reduce chormatic aberration by employing a slight taper in the lens, such that atoms towards the front of the beam feel a stronger focusing force and atoms towards the back of the beam feel a weaker focusing force, allowing all atoms in the beam to be focused to the same focal plane. Simulations suggest that for given initial beam conditions, the pulsed tapered magnetic hexapole lens can image a beam of atoms with sub-10 nm resolution.

In 2016, in the first experimental iteration of the pulsed electromagnetic hexapole, we designed and built a prototype lens that imaged an atomic beam with greater resolution and higher image fidelity than shown in any previous atom imaging experiment [32]. A diagram of the beamline we used is shown in Figure 1.6 and the resulting images are shown in Figure 1.7.

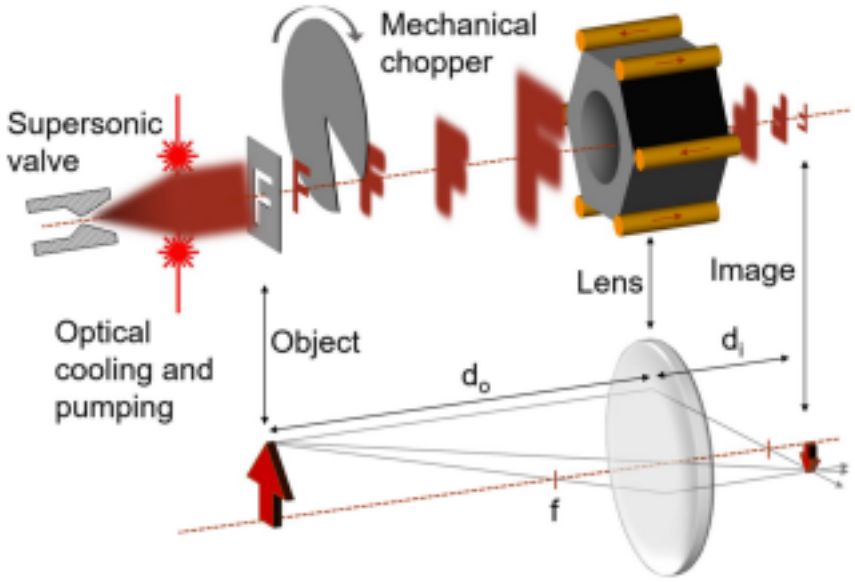

Figure 1.6: A diagram of the beamline for the first iteration of the pulsed magnetic hexapole lens. A supersonic beam is optically pumped and laser cooled prior to being passed through an object plane. It then propagates toward the magnetic lens before being imaged on a microchannel plate and phosphor screen. A mechanical chopper is employed to reduce the longitudinal extent of the beam, thus reducing chromatic aberration.

The prototype lens was effective for imaging millimeter size objects down to the 100 µm scale, however further refinement of the process is necessary to reach the nanoscale. Like any other focusing mechanism, our lens has a magnification factor equal to the ratio of the image distance to the object distance. At a realistic ratio of 1:10, in order to reach a 10 nm spot size, we would have to start with a beam size on the order of 100 nm. This would require passing a millimeter size atomic beam through a 100 nm slit, causing a reduction of flux of at least four orders of magnitude in one dimension or eight orders of magnitude in two dimensions. A single lens imaging system cannot achieve both the resolution and flux necessary to be useful for atom nanofabrication or neutral atom microscopy.

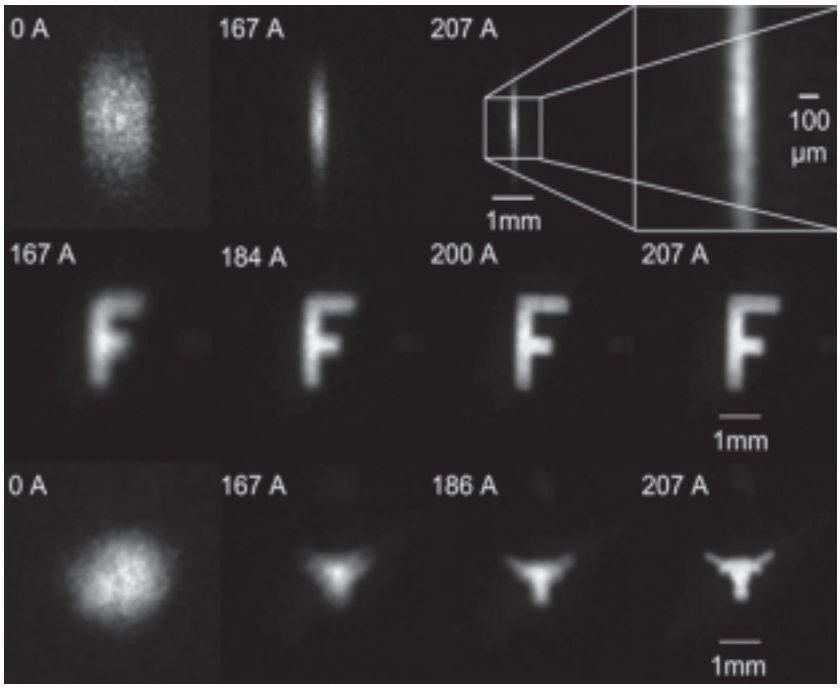

Figure 1.7: The imaged atomic beam focused by a prototype magnetic hexapole lens. The top row shows the focusing of a slit as the lens is brought into focus. The 150 µm resolution beats that of any previous atom focusing experiment. The middle and bottom row show two series of two-dimensional shapes being brought into focus to demonstrate the ability of the lens to image two-dimensional structures.

1.2 A complex atom lens

The body of this dissertation will focus on the second iteration of the magnetic focusing experiment in the Raizen lab. This iteration expands on the progress made by the prototype pulsed electromagnetic hexapole lens, demonstrating a mechanism for enhancing the brightness and density of an atomic beam by a factor of 20 through the use of a permanent magnetic hexapole, laser cooling and a pulsed magnetic hexapole lens. In principle, this method of beam brightening can be repeated in stages to create a sufficiently bright beam that can be focused to the nanoscale using an aberration-corrected atom lens while maintaining levels of atom flux necessary for efficient neutral atom nanofabrication and microscopy. A diagram of our experimental beamline is shown in Figure 1.8.

The experimental beamline begins with a pulsed Even-Lavie supersonic nozzle with a dielectric barrier discharge attachment. This supersonic nozzle provides for a

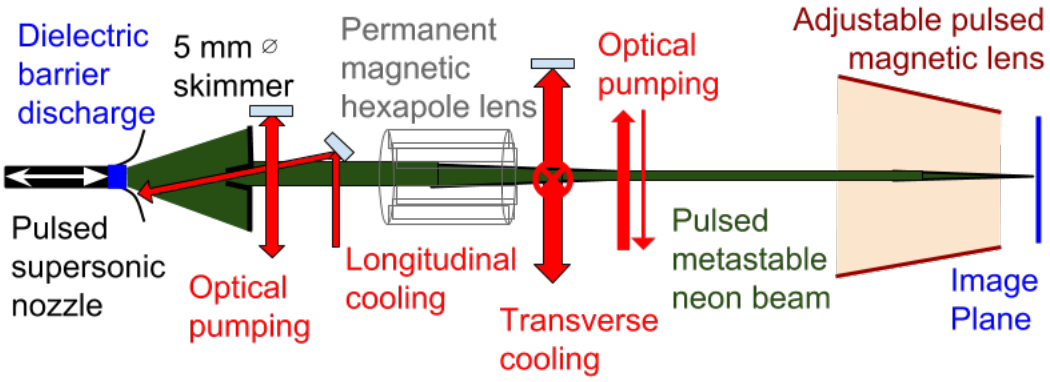

Figure 1.8: A diagram of the experimental beamline of our complex magnetic lens. A supersonic nozzle creates a pulsed beam of cold metastable neon atoms, which is optically pumped and longitudinally cooled, prior to being focused by a permanent magnetic hexapole lens. It is transversely cooled at the focus, prior to a second round of optical pumping before it is focused via pulsed magnetic hexapole lens onto a detector.

pulsed high density cold beam of metastable neutral atoms. This nozzle can create significantly brighter and colder beams than those created from thermal sources, allowing for higher density beams with less potential chromatic aberration. Upon exiting the nozzle, the atomic beam is collimated using a conical skimmer. Chapter 2 of this work will cover the Even-Lavie nozzle in further detail.

We then optically prepare the atom beam by optically pumping the atoms to a low field seeking magnetic state and longitudinally laser cooling the atomic beam in its moving frame to reduce longitudinal beam temperature. Chapter 3 will cover all optical elements of this experiment.

The beam then passes through a permanent magnetic hexapole that serves as a collector lens to focus the divergent atomic beam to a spot downstream from the lens. The theoretical framework for magnetic forces on atoms including hexapole lenses will be discussed in Chapter 4.

At the focus of the permanent magnetic hexapole, we employ transverse laser cooling to collimate and brighten the atomic beam. The beam is then optically pumped back into the low field seeking magnetic state. Focusing and collimating in conjunction form a sort of funnelling effect on the atomic beam, which will be discussed in Chapter 5.

The beam then propagates towards a final pulsed electromagnetic hexapole lens, which focuses the beam onto a detector downstream. Chapter 6 covers the properties of the pulsed lens including sources of aberration that we must overcome in order to achieve true nanoscale focusing.

Phase space, including preserving and enhancing phase space density is an important aspect of any imaging system. I will describe the framework of the experiment in the phase space picture in Chapter 7.

I will cover the the experimental results including performance of the permanent magnetic lens, beam brightening through transverse cooling and focusing using the pulsed electromagnetic hexpole lens at different object and image distances in Chapter 8.

The final chapter, Chapter 9 will summarize the work presented in this document and examine pathways towards true nanoscale atomic focusing with a complex atom lens.

Chapter Two: Supersonic nozzle

The starting point for the experiment is the Even-Lavie supersonic nozzle with dielectric barrier attachment [33] [34] [35]. The Even-Lavie valve is a common tool used in the Raizen lab due to its ability to create cold, dense supersonic beams and has been discussed in many Raizen lab theses [36] [37].

2.1 Supersonic expansion

Due to the excellent work quantitatively describing supersonic expansion by several of my former colleagues, I will qualitatively describe the features of our nozzle that give rise to our supersonic neon beam.

Our nozzle is backed by a reservoir of neon gas at 20 bar and cooled with a dewar of liquid nitrogen. At equilibrium, the velocity distribution of atoms in a gas is given by the standard Maxwell-Boltzmann distribution:

$$f(v) = \left(\frac{m}{2\pi k_B T}\right)^{\frac{3}{2}} e^{-\frac{mv^2}{2k_B T}}. \tag{2.1}$$

When a gas passes through an aperture, if the mean free path of the atoms in the gas is much larger than the size of the aperture, the resulting beam will have a thermal distribution. If the mean free path is much smaller than the aperture, the atoms will be able to collide and thermally equilibrate upon expansion resulting in a cold mono-directional beam. In this case, the average velocity of the atoms will be much greater than their velocity spread. This regime is known as the supersonic regime.

The mean free path is given by

$$l = \frac{1}{\sqrt{2}\sigma\rho}, \tag{2.2}$$

where l is the mean free path, σ is the collisional cross section and ρ is the number density of atoms.

To calculate σ, we use the Lennard-Jones parameter $d_{\mathrm{LJ}} \approx 0.278\,\mathrm{nm}$ as a stand in for collisional diameter. $\sigma = \pi d_{\mathrm{LJ}}^2$ [38]. To calculate ρ, we use the ideal gas law. $\rho = \frac{P}{k_B T}$.

Plugging in values gives

$$l = \frac{k_B T}{\sqrt{2}\pi d_{\mathrm{LJ}}^2 P} \approx 2.5\,\mathrm{nm}. \tag{2.3}$$

The diameter of our nozzle is 200 µm, five orders of magnitude larger than the mean free path, thus our beam will be in the supersonic regime.

In addition to the size of the aperture, the shape of the nozzle also plays an important role in the parameters of the beam as it exits the nozzle. The ideal nozzle shape for creating a supersonic beam is that of the de Laval nozzle shown in Figure 2.1 in which the gas passes through a tube of smoothly decreasing diameter before reaching a chokepoint (the aperture) and expanding through a tube of smoothly increasing diameter. For ease of opening and closing the aperture, the Even-Lavie valve does not have the converging tube prior to the aperture, but uses a trumpet shaped opening for controlled adiabatic expansion of the beam exiting the nozzle.

As the beam passes through the nozzle, it will adiabatically expand and its initial thermal energy will be converted into mono-directional kinetic energy. From the first law of thermodynamics in a system with no heat transfer

$$U_f + (PV)_f = U_i + (PV)_i, \tag{2.4}$$

where U is the internal energy, P is the pressure and V is the volume. Although V is poorly defined in this case, we know that $P_f = 0$ and $(PV)_i = nk_BT$ from the ideal gas law. We also know that initial internal $U_i = \frac{3}{2}nk_BT$ is the thermal energy of the system. Putting these together gives

$$U_f = \frac{3}{2}nk_BT + nk_BT = \frac{5}{2}nk_BT \tag{2.5}$$

The expectation value of the atomic beam velocity far from the nozzle will be given by

$$v = \sqrt{\frac{2U_f}{mn}} = \sqrt{\frac{5k_BT}{m}} \approx 490\,\mathrm{m\,s^{-1}}. \tag{2.6}$$

Two other relevant parameters for describing a supersonic beam are speed ratio and divergence angle. The speed ratio is defined as the ratio between the velocity of the beam in the lab frame and the velocity spread of the beam. $S = \frac{v}{\Delta v}$. We calculate this by measuring the time of flight (TOF), τ, of the beam from nozzle to detector and the full width at half maximum (FWHM) of the signal in time as it reaches the detector.

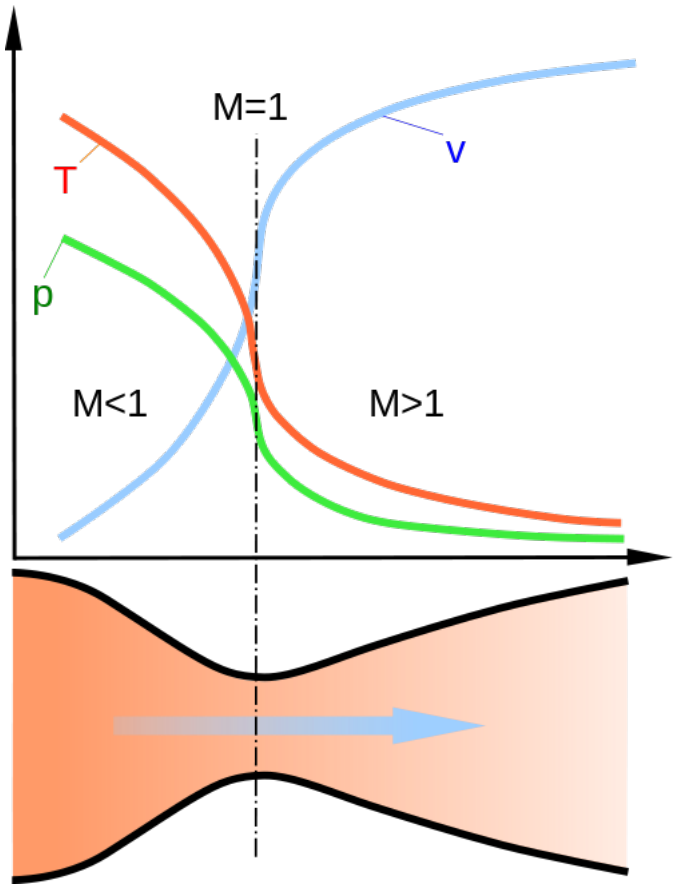

Figure 2.1: A diagram showing the pressure, temperature, velocity of atoms as they pass through a de Laval nozzle. The Even-Lavie valve has a flat plane at its choke-point, but has a similar trumpet shape upon its exit. Source: wikimedia [39]

While the Even-Lavie nozzle has been shown to cool large moleucules below 1 K, smaller lighter elements such as helium and neon will produce the coldest beams [40].

$$S \equiv 2\sqrt{2\ln 2}\frac{\tau}{\Delta\tau_{\mathrm{FWHM}}}. \tag{2.7}$$

Depending on the exact nozzle parameters used, this ratio can reach as high as 30. This speed ratio is also known as the Mach number.

The Even-Lavie valve boasts a beam with a full angle at half maximum of 10 degrees [34]. We do not experimentally verify this as we use a 5 mm diameter skimmer 20 cm from the nozzle. This ratio corresponds to an angle of 1.43 degrees, significantly smaller than the full angle at half maximum of the beam produced by the nozzle.

The relatively tight divergence of the beam does help in passing a larger proportion of atoms through the skimmer and along to the rest of the experiment.

2.2 Even-Lavie valve structure

At its essence, the Even-Lavie valve is a solenoid valve. The seal of the valve is a stainless steel plunger held with a spring against a 200 micron hole in a kapton gasket. A current pulse is passed through a solenoid outside the body of the plunger, creating a force on the plunger away from the kapton gasket, allowing gas to escape through the hole in the gasket and into the vacuum chamber. A cutout of the nozzle is shown in Figure 2.2.

The nozzle has a 40 degree opening so as to optimize the atom number, divergence angle, and speed ratio of the resulting beam. We operate the nozzle with a pulse opening time of 30 µ and a repetition rate of 4 Hz.

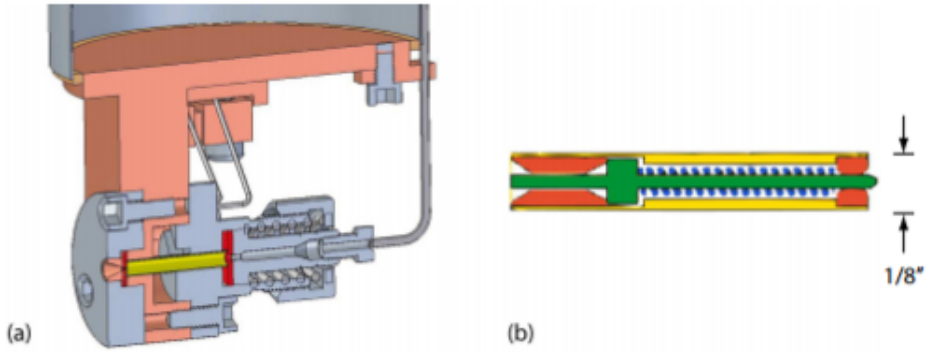

Figure 2.2: (a) A cutout of the Even-Lavie Valve attached to a dewar filled with liquid nitrogen. Gas enters the nozzle through a 1/16 in. OD stainless steel tube pressurized at 20 bar. A stainless steel tube (shown in gold) held between two kapton gaskets (shown in red) houses the plunger and restoring spring. (b) Inside the stainless steel tube lies a plunger shown in green that, when the valve is closed, is pressed against a hole in the front kapton gasket with a small spring (shown in blue.) The plunger is kept in place with two ceramic spacers (shown in orange.)

2.2.1 Dielectric barrier discharge

In order to create a beam of metastable neon atoms, we must excite the atoms exiting the nozzle to the metastable state. To accomplish this we use a dielectric barrier discharge (DBD) attachment to the nozzle. Upon exiting the nozzle, a short burst (10 cycles) of high voltage (1000 V) RF (750 kHz) current is sent to a dielectric material that forms the nozzle exit. The DBD creates an electron discharge from which electrons bombard ground state neon atoms, exciting them to higher energy states, a photograph of which is shown in Figure 2.3.

Figure 2.3: A photograph of the Even-Lavie valve with DBD upon nozzle opening. Electrons bombard the neutral neon atoms, exciting them to higher energy states. The orange glow is a result of emitted photons as atoms decay between higher and lower energy states. Source: Luria et al. [34]

A small fraction, roughly a part in 10^4, will be excited to the desired metastable $^3P_2$ state. (This metastable state will be discussed in detail in Chapter 3.1.) An

added benefit of the DBD is its minimal heating of the atomic beam, allowing us to produce a cold, mostly collimated supersonic beam of metastable neon.

2.2.2 Skimmer

In order to further collimate the atomic beam, we use a 5 mm skimmer 20 cm from the opening of the nozzle. This gives the beam a maximum divergence angle of 1.43 degrees, compared to a 10 degree full angle at half maximum coming out of the nozzle. The skimmer has the shape of a sharp cone with a removed tip for an aperture. The sharp tip points toward the nozzle. The walls of the skimmer must be as thin as possible so as to avoid heating the beam and clogging the aperture, as would occur if one used a flat hole in an attempt to collimate a supersonic beam. The temperature profile of an atomic beam passing through a skimmer is shown in Figure 2.4.

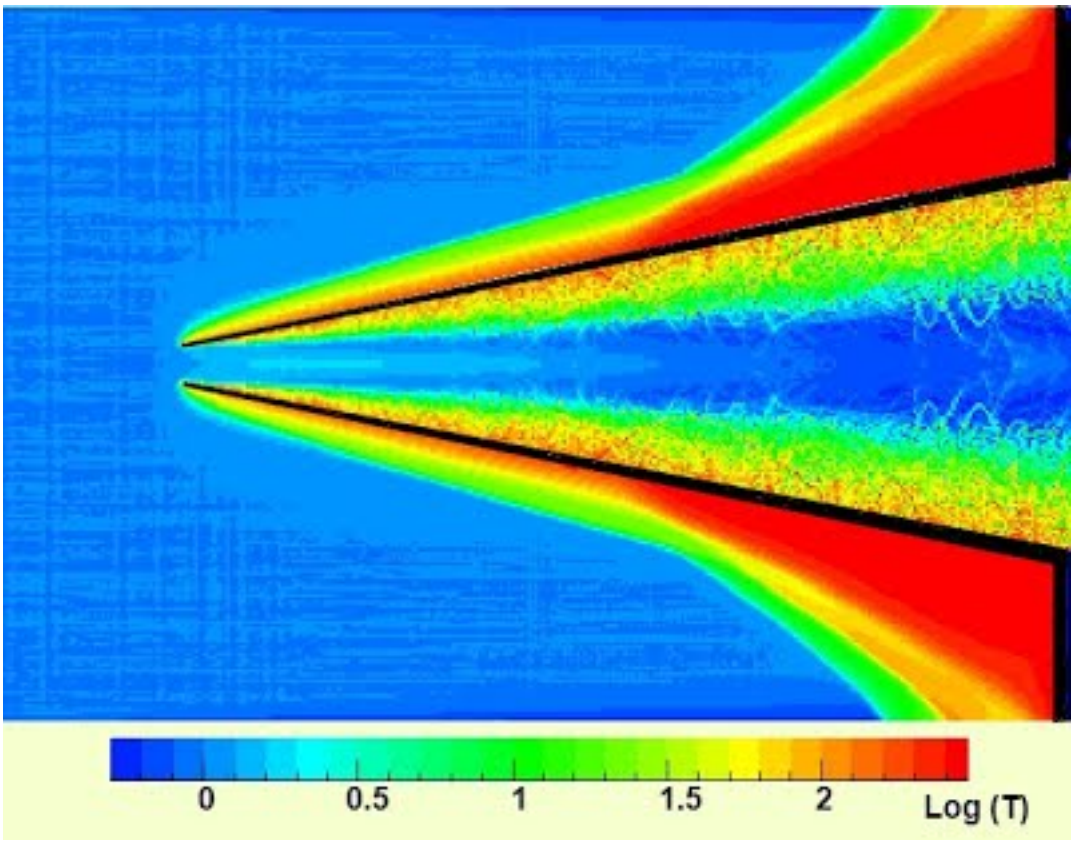

Figure 2.4: A simulation of the local temperature profile of a supersonic helium beam passing through a skimmer. The temperature of the beam will be warmest near the edge of the skimmer and coldest near its center. Source: Luria et al. [34]

Chapter Three: Optical pumping and laser cooling

Throughout the length of the beamline, we have two mechanisms for manipulating the atomic beam: a laser and a magnetic field gradient. This chapter will focus on the laser and its interactions with the atomic beam, notably through optical pumping and laser cooling.

3.1 Neon

In principle, a cold beam of any atom with an easily accessible paramagnetic metastable state would suffice as a probing mechanism for metastable atom microscopy. The noble gases fit these criteria and are therefore excellent candidates for atomic focusing. As discussed in the chapter on the supersonic nozzle, lighter noble gases will form colder beams upon supersonic expansion. A relevant parameter for the susceptibility of an atom to be magnetically focused is its magnetic moment to mass ratio.

$$\mu = \mu_B m_j g_j. \tag{3.1}$$

here μ_B is the Bohr Magneton, and $g_j = \frac{3}{2}$ for neon and $g_j = 2$ for helium is the Landé g factor.

$$\left(\frac{\mu}{m}\right)_{\text{Ne}} = \frac{\mu_B \times 2 \times \frac{3}{2}}{20\,\text{u}} = \frac{3\mu_B}{20\,\text{amu}} \tag{3.2}$$

$$\left(\frac{\mu}{m}\right)_{\text{He}} = \frac{\mu_B \times 1 \times 2}{4\,\text{u}} = \frac{\mu_B}{2\,\text{u}} \tag{3.3}$$

As the magnetic moment to mass ratio is within a factor of four for helium and neon, either would be an ideal candidate. The tiebreaker goes to the atom for which we already had a laser in the lab. In our case, neon.

3.1.1 Electronic structure of neon

Pictured below are the electron configurations of neon in its ground state and lowest excited states. I will denote the different electron states using the standard Russell-Saunders notation. The term symbol is given by ${}^{2S+1}L_J$ Where S is the total elec-

tronic spin quantum number, $2S+1$ is the multiplicity of states, L is the total orbital angular momentum quantum number, and $J = L+S$ is the total angular momentum quantum number. We use the standard notation for L: $L = 0$ is noted with the symbol "S", $L = 1$ corresponds to "P", followed by "D", "F", "G" for $L = 3, 4, 5$. Note J can take any value $|L+S|$, $|L+S-1|$, $|L+S-2|$....$|L-S|$

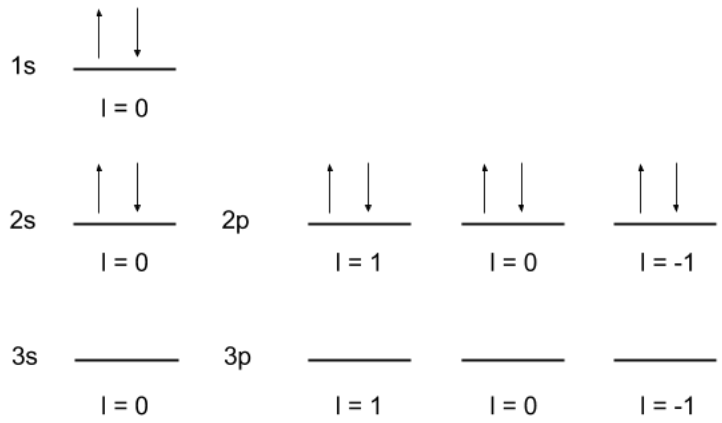

Figure 3.1: The electron configuration of neon in its $^1S_0$ ground state

As shown in Figure 3.1, neon in its ground state has no unpaired electrons, therefore $S = 0$. Additionally, like all noble gases, the ground state of neon consists of filled, complete electronic orbitals and thus has no net orbital angular momentum, $L = 0$. Therefore, the only possible value for J is $J = L + S = 0 + 0 = 0$. This gives the ground state term symbol $^1S_0$. Neon does not have a nuclear magnetic moment, therefore the total atomic magnetic moment will be equal to the electronic magnetic moment for all electronic states.

As shown in Figure 3.2, in neon's lowest energy excited state, an electron is removed from the $2p$ orbital and added to the $3s$ orbital. In the lowest energy configuration, the $3s$ electron will have spin in the same direction as the remaining unpaired $2p$ electron, giving a total electron spin of $s = \frac{1}{2} + \frac{1}{2} = 1$. There also exists a higher energy state in which the $3s$ electron spin is antiparallel to the unpaired $2p$ election, however that state is not metastable and any atom in that state will decay quickly to the ground state. To calculate the orbital angular momentum, sum the orbital angular momenta of each electron in the $2p$ states. $l = 1 + 1 + 0 + 0 - 1 = 1$. There will be three possible values of J, $(J = 1, 2, 3)$ hence it is referred to as a triplet

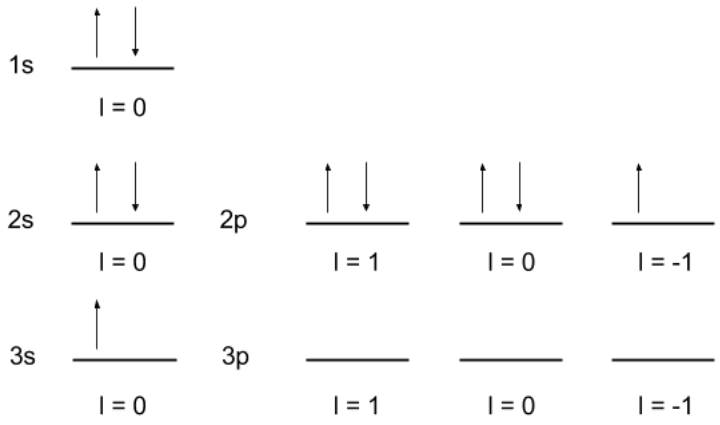

Figure 3.2: The electron configuration of neon in its ^3P lower excited state

state. The state with maximum total angular momentum, $J = 2$, will have the lowest energy, followed by the $J = 1$ state and the $J = 0$ state. The term symbols for these states will be denoted $^3P_{0,1,2}$.

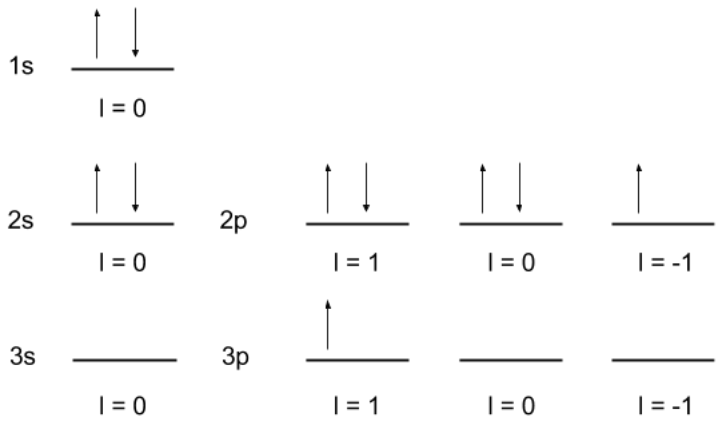

Figure 3.3: The electron configuration of neon in its ^3D upper excited state

We next consider the excited state in which the electron removed from the $2p$ state is added to the $3p$ orbital as shown in Figure 3.3. Again, in the lowest energy configuration, the $3p$ electron spin will be parallel to the spin of the unpaired $2p$ electron spin, giving a total electron spin of $s = \frac{1}{2} + \frac{1}{2} = 1$. The antiparallel case will have higher energy and is not relevant to this experiment. The state with the lowest

energy will maximize L. This requires the $3p$ electron to have an angular momentum antiparallel to the unpaired $2p$ electron. The total orbital angular momentum will be the sum of all $2p$ and $3p$ orbital angular momenta. $l = 1 + 1 + 0 + 0 - 1 + 1 = 2$. The three possible values of J in this triplet state are $J = 1, 2, 3$. The state with maximum $J = 3$ will have the lowest energy followed by the $J = 2$ and $J = 1$ states. The term symbols for these states will be denoted ${}^3D_{1,2,3}$

3.1.2 Transitions between excited states

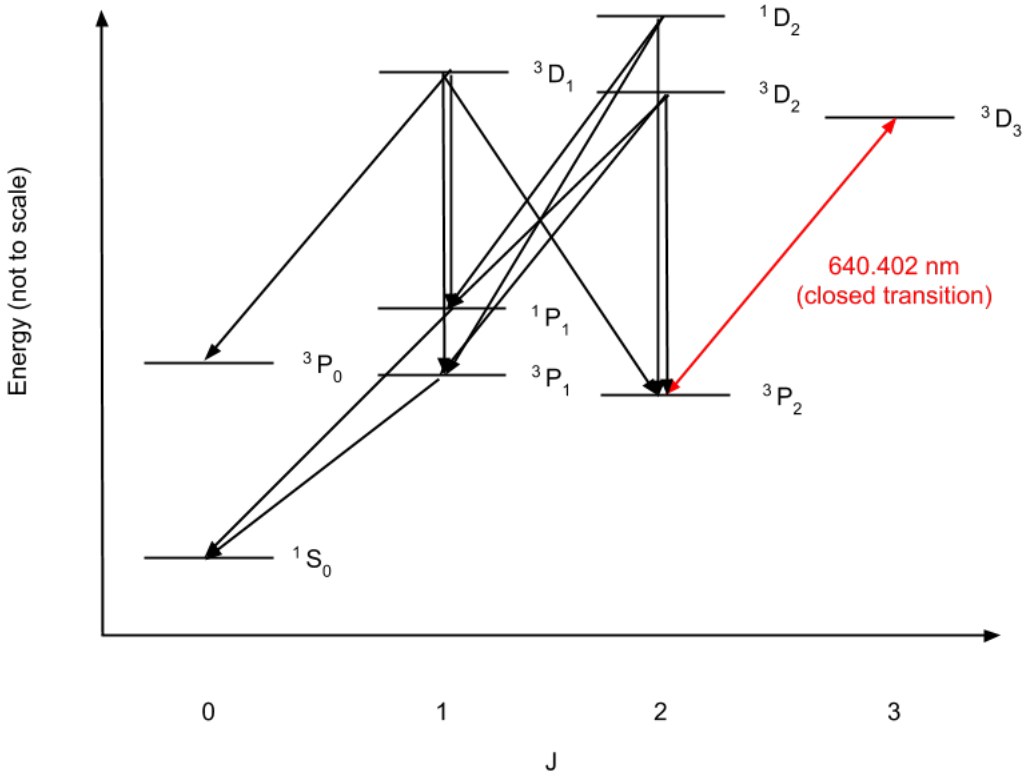

Figure 3.4: The lowest lying electronic states of neon. Black arrows represent allowed spontaneous transitions. The red arrow represents the only closed transition, which will be the only laser transition we use throughout the experiment.

The allowed transitions are shown in Figure 3.4. Note that atoms in all states with the exception of ${}^3P_0$, ${}^3P_2$, and ${}^3D_3$ will decay to the ground state and may be neglected. The allowed transitions are determined by selection rules. Because there

is no allowed transition between the aforementioned $^3P_0$, $^3P_2$, and $^3D_3$ states and the ground state, these will be long-lived metastable excited states. The lifetime of an atom in the $^3P_2$ state is 14.73 s [41], over 1,000 times longer than the lifetime of the experiment. As there is no closed transition including $^3P_0$ atoms, and $^3P_0$ atoms have no magnetic moment and therefore do not interact with magnetic fields, $^3P_0$ atoms will feel no force from either laser radiation pressure or inhomogeneous magnetic fields. A small number of collimated $^3P_0$ atoms will reach the detector, however their density will be quite low compared to the beam of focused $^3P_2$ atoms, therefore we neglect their presence in our atomic beam and instead fixate on atoms in the $^3P_2$, and $^3D_3$ states.

Ground state neon atoms cannot be excited to the $^3P_2$ state with a single photon, but can be excited through electron bombardment. While inefficient, electron bombardment is the best method available for production of metastable atoms [42]. Once in the metastable $^3P_2$ state, atoms can be manipulated using a laser tuned to the $^3P_2 \rightarrow ^3 D_3$ transition. This transition has a wavelength of 640.402 nm, a lifetime of 19.4 ns and a linewidth of 8.18 MHz.

3.2 Laser

This section will examine the laser system and its design. We use two diode lasers at the same wavelength, a master and a slave. The master laser is an extended cavity diode laser. We use Doppler free spectroscopy and a feedback loop to lock the frequency of the laser to the $^3P_2 \leftrightarrow {}^3D_3$ transition of neon. We then send a portion of the frequency locked master laser to drive the slave laser, increasing the total available laser power in a technique known as injection locking.

3.2.1 Extended cavity diode laser

We use an extended cavity diode laser in the Littrow configuration as shown in Figure 3.5. This configuration has a diffraction grating as one edge of its laser cavity. The angle of the diffraction grating is such that the m_{-1} beam is reflected back into the laser cavity and the m_0 beam is reflected toward the laser diagnostics and experiment. The diffraction grating is on a rotatable stage such that the angle between the grating and the output of the laser diode can be precisely controlled. We control this angle

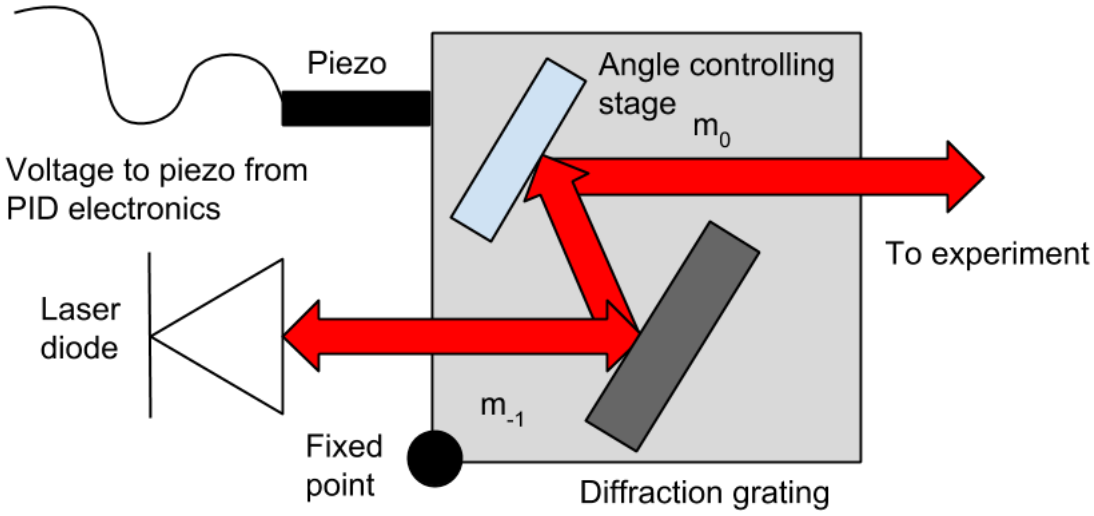

Figure 3.5: A diagram of an extended cavity diode laser

by pushing on one corner of the stage with a voltage controlled piezoelectric device. The voltage sent to the piezo is determined by a feedback loop designed to maintain the angle of the stage and thus the frequency of the laser. The angle controlling stage also contains a mirror parallel to the diffraction grating such that the laser will exit that stage at the same angle relative to the diode regardless of the angle between the diode and stage. Manually controlling the current sent to the laser diode as well as the voltage sent to the piezo can ensure that the laser is single mode and has a wavelength within one picometer of the optimal wavelength of 640.402 nm, however more frequency precision and stabilization is needed. We use a wavemeter and Fabry-Perot interferometer to measure wavelength and mode structure respectively. For more detailed information on an extended cavity diode laser, the reader is encouraged to read the paper by Arnold, Wilson, and Boshier in *Review of Scientific Instruments* [44].

3.2.2 Doppler-free spectroscopy

The goal of Doppler free spectroscopy is to set the frequency of the laser to a reference frequency. In our case, this reference frequency is 40 MHz below the frequency of the transition between the $^3P_2$ and $^3D_3$ states. We use a glass cell with 50 mTorr of neon

inside. We pass current through a coil around the cell to create an RF field. This RF field will accelerate free electrons, which will bombard ground state neon atoms and excite a small but sufficient percentage of them to the metastable $^3P_2$ state. When the RF field is applied, the neon cell will have a soft orange glow from the allowed $^3P \leftrightarrow {}^3D$ transitions. The optimal capacitance and inductance of the RF coil are empirically determined, emphasis on "empirically."

In order to understand Doppler-free spectroscopy, we must first analyze the simplified case of Doppler-broadened spectroscopy. Experimentally, this entails sending a laser through the neon cell and measuring the transmitted laser power as a function of laser frequency. When the laser is on resonance with a certain velocity class of atoms in the cell, some laser light will be absorbed by atoms in said velocity class and will not reach the photodetector beyond the cell. However, this loss in signal will be over a very broad range as the atoms in the cell have a thermal velocity distribution. The apparent frequency of the incoming light will be Doppler shifted by an amount proportional to the relative velocity in the direction of the laser for each individual atom. If we were to use Doppler broadened spectroscopy, it would be very difficult if not impossible to use a PID enabled feedback loop to lock the frequency of the laser diode based on the power measured by the photodetector. A more sophisticated locking mechanism is needed. A diagram for Doppler-broadened spectroscopy is shown in Figure 3.6.

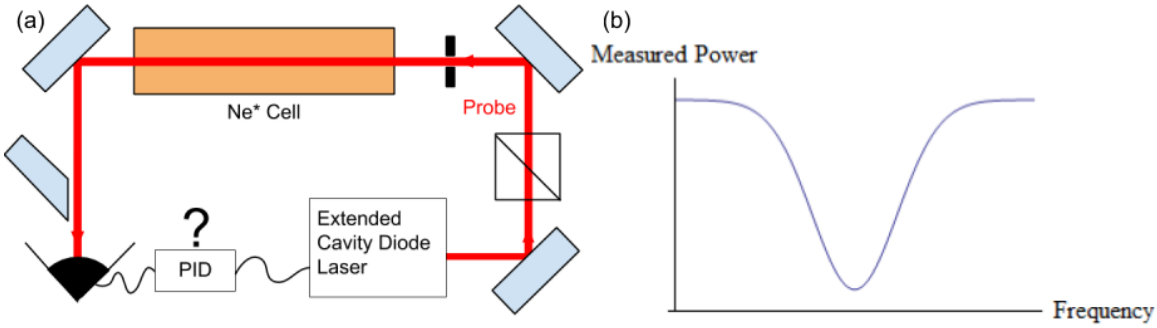

Figure 3.6: (a) A diagram of Doppler-broadened spectroscopy (b) The qualitative shape of the transmitted power as a function of laser frequency. The width of the shape is proportional to the width of the velocity distribution of the neon atoms with the cell.

In order to solve this problem, we add a counterpropagating beam overlapping

with the original laser while both are inside the neon cell as shown in Figure 3.7. We refer to the original beam that traverses the cell to the photodetector as the probe beam and the counterpropagating beam as the pump beam. While scanning the frequency of both the pump and probe beams, there will be a frequency at which both beams are interacting with the same velocity class of atoms. In the Doppler-broadened case, these atoms would absorb the probe light, but in the Doppler-free case, a portion of these atoms will have been excited by the pump beam. When the probe beam reaches an already excited atom, the atom will spontaneously emit two photons in the direction of the incoming beam. This will result in an increase in power measured at the overlap frequency [45]. This increase appears as a small dip known as the Lamb dip, ideally with width equal to the linewidth of the laser transition, in our case about 8 MHz. We use a PID enabled feedback loop with detected probe laser power as an input and voltage sent to the diffraction grating piezo as an output to ensure that the frequency of the laser does not drift from the frequency of the Lamb dip.

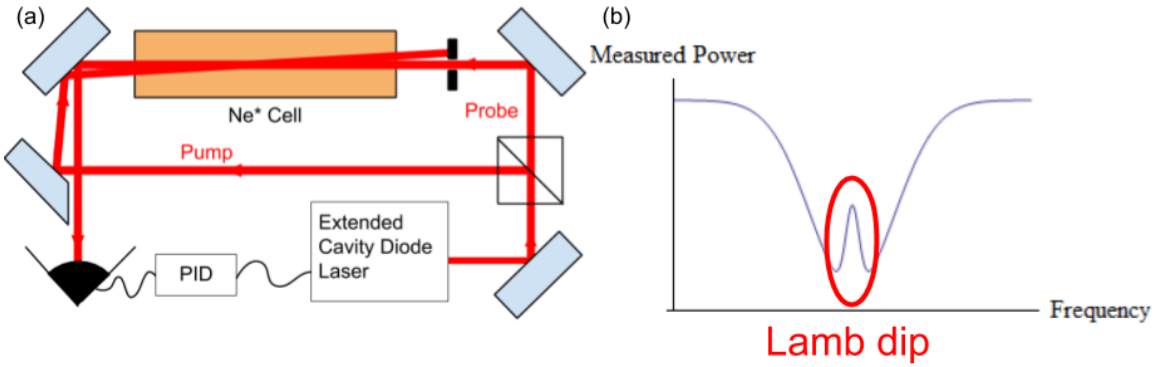

Figure 3.7: (a) A diagram of Doppler-free spectroscopy (b) The qualitative shape of the transmitted power as a function of laser frequency. The narrow dip in measured power occurs when the pump and probe beams are both addressing atoms in the same velocity class in the direction of laser propagation. Note: in reality, we use an 80 MHz acousto-optic modulator (AOM) whose frequency is modulated by an amplitude of 1 MHz. While not shown in the image, this allows us to use a lock-in amplifier to amplify the Lamp dip and results in the output laser frequency being 40 MHz off resonance.

3.2.3 Injection locking

After accounting for the laser power that has been split from the master laser and sent to the pump and probe branches for Doppler free spectroscopy and the beams sent to the wavemeter (EXFO part number WA-1000) and Fabry-Perot interferometer for beam diagnostics, there is insufficient laser power remaining to handle the demands of the experiment. To create this laser power, we add a slave laser that is injection locked to the master, ensuring its frequency and mode structure match that of the master laser [43]. Both the master and slave lasers are temperature controlled using thermoelectric coolers. A photograph of the master and slave lasers is shown in Figure 3.8.

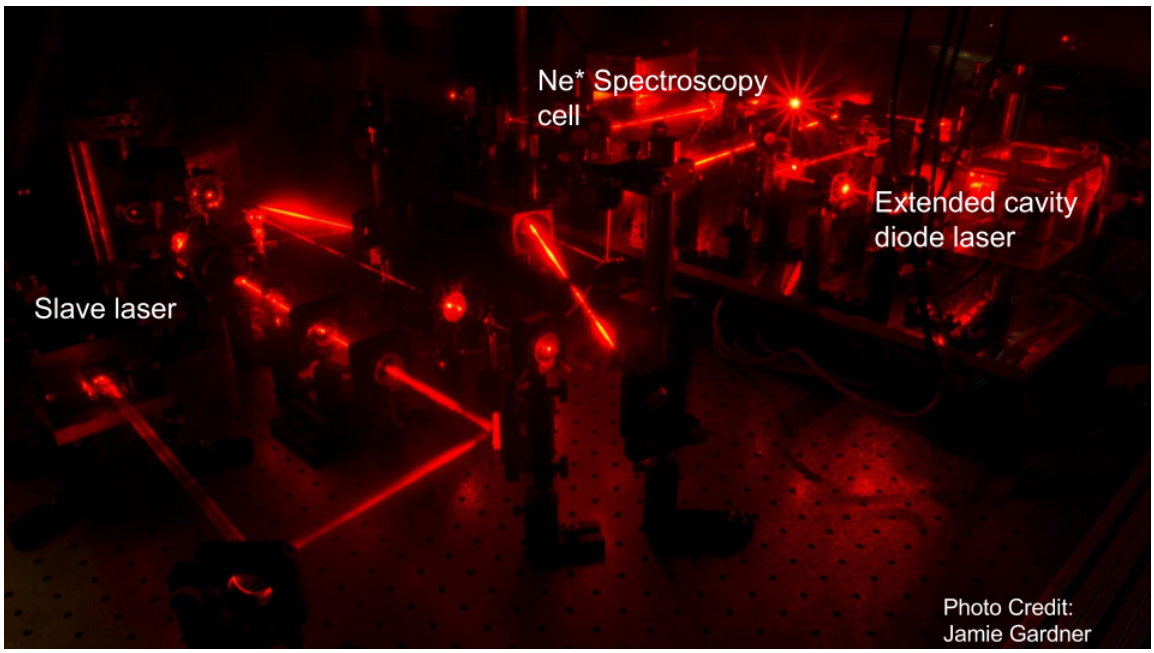

Figure 3.8: The master and slave lasers

The slave laser is a diode laser and when not driven, has a wavelength approximately 640 nm, 100 mW output power and high noise. We seed the slave laser with roughly 4 mW of power split from the master laser. This light enters the slave laser through a partially transmissive mirror at the Brewster angle. If the frequency and shape of the incoming light are sufficiently close to the natural frequency and shape of the slave laser, the slave laser will oscillate with the same frequency as the seed light, but with a much higher output power. This gives us about 100 mW extra usable

laser power for the experiment. A cartoon demonstrating the features of injection locking is shown in Figure 3.9.

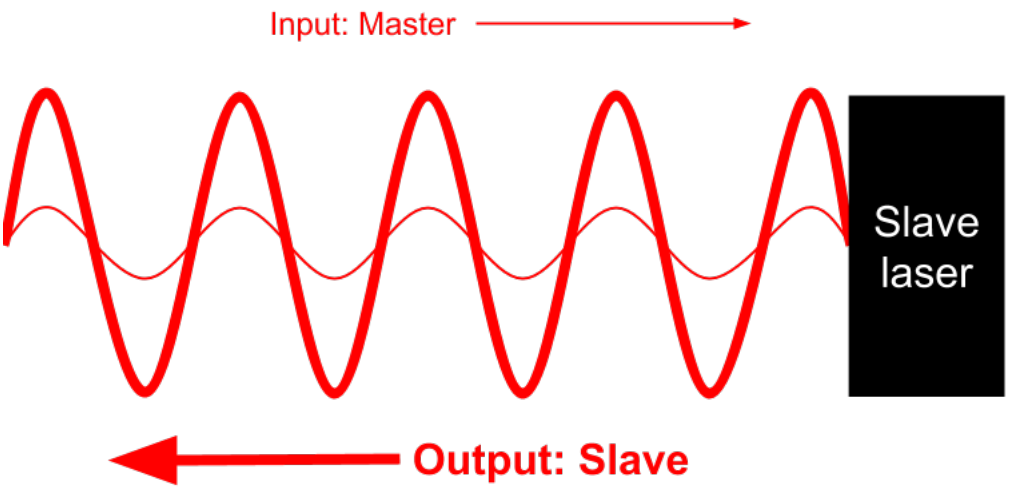

Figure 3.9: A small amount of laser light from the master is sent to a slave laser. The slave laser will oscillate at the same frequency as the incoming laser, but with a much greater power.

We can calculate the total slave laser power necessary for the experiment by adding the power needed for each stage. For transverse laser cooling, we need two branches of 10 mW light, requiring 30 mW of power from the slave given an approximate AOM efficiency of 2/3. For longitudinal cooling, we need a final power of 5 mW, requiring 10 mW of slave power given the efficiency of the double pass of roughly 1/2. For optical pumping, we need three total branches each with roughly 2 mW of power each, corresponding to a total of roughly 10 mW of input power. All told, we need about 50 mW of power from the slave, well within the range it can produce. This extra power will come in handy for future iterations of the experiment requiring further stages of laser cooling and optical pumping.

This coupling of two oscillators with similar natural frequencies is not limited to lasers, but extends to classical oscillators as well. It was first noticed by Huygens when examining two nearby pendulum clocks that would oscillate with the same phase over a significantly longer period of time than had they not been coupled [46].

3.3 Optical pumping

In section 3.1, I refer to the optical transition we use as being between the $^3P_2$ and $^3D_3$ states of metastable neon. While this is true, it does not tell the whole story. Within each of these states exist a number (5 for $^3P_2$, 7 for $^3D_3$) of magnetic substates. We denote these substates with the symbol m_j which take integer values ranging from $-J$ to J. If J were a half integer, the m_j's would also be half integers, but that will not be the case in this experiment.

When there is no magnetic field present, these substates are degenerate, but the degeneracy is lifted when a magnetic bias field is applied. The shift in energy in the presence of a magnetic field is given by the Zeeman shift. $\Delta E = B\mu_B m_j g_j$.

The specific substate we are most interested is the $m_j = 2$ low field seeking state, as this is the stable accessible substate that will be most strongly focused using a magnetic hexapole lens. The magnetic bias field need only be strong enough to lift the degeneracy. In our case $B = \frac{\Delta E}{\mu_B m_j g_j} = \frac{8\,\mathrm{MHz}\times h}{\mu_B m_j g_j} \approx 2 \times 10^{-4}\,\mathrm{T}$ where h is Planck's constant. We tune this magnetic field using Helmholtz coils with adjustable currents.

We can reach this state by hitting a metastable atom repeatedly with circularly polarized light with a magnetic bias field in the direction of laser propagation. Upon absorbing a photon with circular polarization, the atom will absorb the angular momentum of the photon as well as its energy. The atom will thus be excited to the corresponding $^3D_3$ substate with m_j one greater than its original value. The atom will then spontaneously emit a photon and decay back to a $^3P_2$ state. Upon emission, the magnetic quantum number of the atom can either increase by 1, decrease by 1 or stay the same, depending on whether the emitted photon has circular or linear polarization. The probability of each is determined by Clebsch-Gordan coefficients [47]. Over a complete cycle of absorption and spontaneous emission, the magnetic quantum number m_j can increase by 2, increase by 1 or not change. While the atom is not guaranteed to increase over a single cycle, after a small number (about 10) of cycles, nearly all atoms will end up in either the $^3P_2$ state with $m_j = 2$ or $^3D_3$ state with $m_j = 3$. The transition between these two states is closed, meaning that once an atom reaches either state, it will not decay to a state with lower m_j. Once the atom is no longer in the laser field, if it is still in the $^3D_3$ state with $m_j = 3$ it will spontaneously decay to $^3P_2$ state with $m_j = 2$. The transitions between the $^3P_2$ substates and $^3D_3$ substates are shown in Figure 3.10.

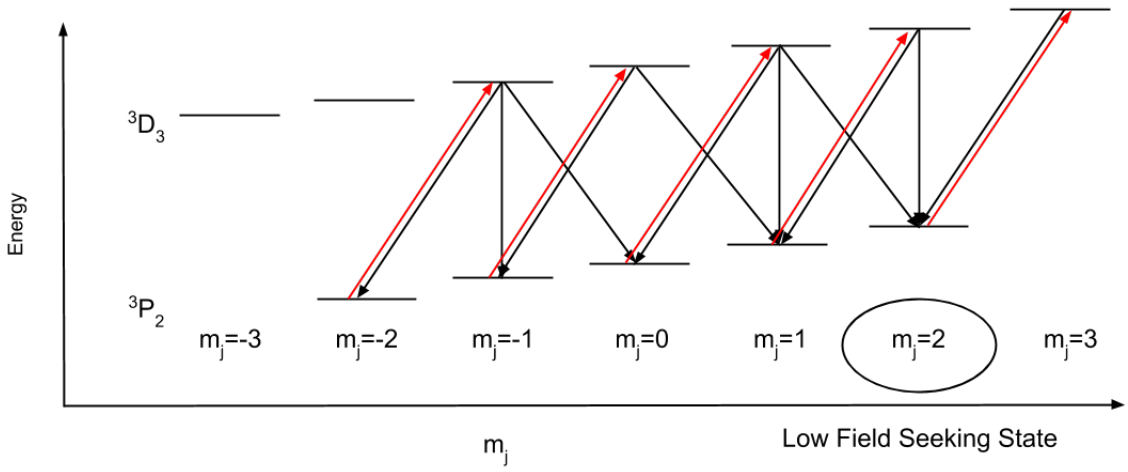

Figure 3.10: A diagram of optically pumping an atom from any magnetic substate to the $m_j = 2$ substate. Like a game of Plinko [48] in which the player drops the ball in the slot to the right of where it ended the previous fall and the ball steadily but not monotonically makes its way to the edge of the board, the atom will make its way towards the $m_j = 2$ state.

Between the skimmer and permanent magnetic lens, we create a force neutral optical pumping beam by retroreflecting a single circular polarized beam so as to pump all atoms passing through the beam to the $m_j = 2$ state while providing a net zero radiation pressure on the beam.

3.3.1 Flashed pumping

After the permanent magnetic lens and laser cooling system, the atomic beam is no longer spin polarized, Another round of spin polarization is necessary. This time, we use two distinct optical pumping beams instead of a single retroreflected beam.

Counterintuitively, we use the first beam to pump all atoms to the high field seeking $m_j = -2$ state. The second beam is focused to a waist of 500 µm along the direction of atomic beam propagation immediately after the first beam. As shown in Figure 3.11, this beam is oriented opposite to the direction of the first beam to balance the radiation pressure and is polarized so as to pump atoms passing through it to the $m_j = 2$ state.

For the current iteration of the experiment, we leave both beams in DC mode,

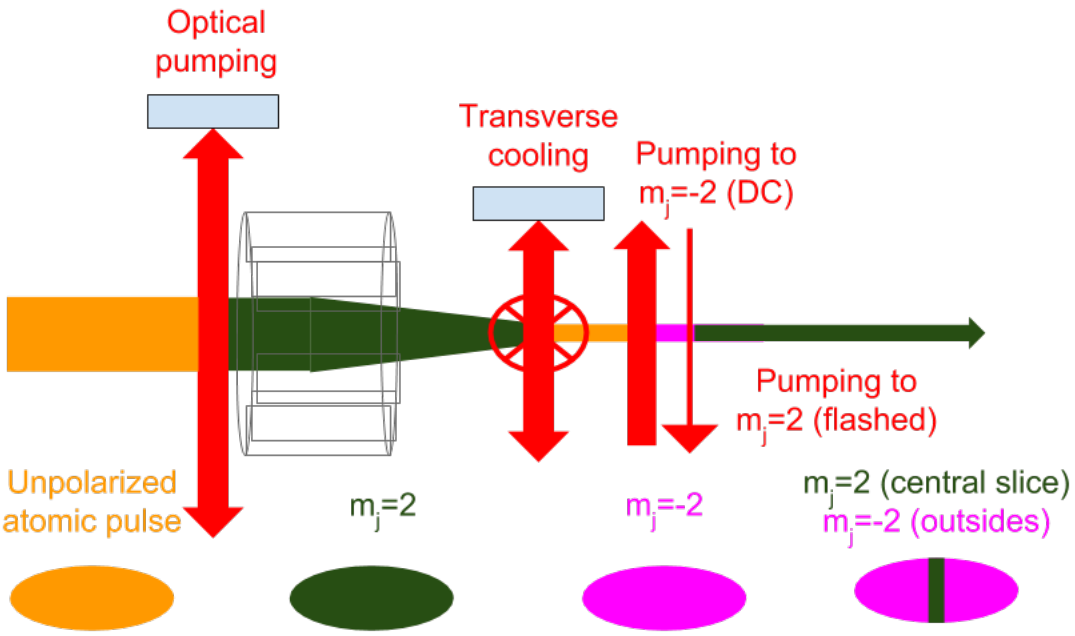

Figure 3.11: A diagram of the optical pumping elements of the beamline. Coming out of the skimmer, the beam is unpolarized. We then optically pump it to the $m_j = 2$ state prior to focusing it and collimating it with a permanent magnetic lens and transverse laser cooling respectively, at which point it is again unpolarized. We then pump the entire beam to the high field seeking $m_j = -2$ state prior to pumping a thin slice of the beam to the $m_j = 2$ stae using a 500 µm wide beam pulsed for 30 µs.

but in future iterations, we plan to pulse the second pumping beam on and off to selectively pump certain atoms in the beam depending on their longitudinal position. We use this to pump only a central portion of specified width of the atomic pulse to the low field seeking state, while leaving the front and back of the pulse in the high field seeking state. The width of the low field seeking slice of the flashed atomic beam will be equal to the pulse duration of the pumping beam times the longitudinal velocity of the atoms. This is a way to shorten the length of the low field seeking atomic pulse. When this total pulse is focused by a magnetic lens, the front and back of the bullet will be defocused creating a wide shallow background layer of atoms while only the middle of the beam will be focused into a bright central spot. This is useful when correcting for chromatic aberration as having a long atomic pulse will

be more subject to chromatic aberration than a short pulse.

3.4 Laser cooling

The following will be a discussion on laser cooling. There are many other great discussions on laser cooling in other Raizen group theses, *Laser Cooling and Trapping* by Metcalf [54] as well from the original laser cooling paper by Wineland et al.[49] Since its invention over 40 years ago, laser cooling has led to many new achievements in physics, including magneto-optical trapping and the creation of a new state of matter, the Bose-Einstein condensate [50]. Laser cooling help paved the way for three Nobel Prizes including Chu, Cohen-Tannoudhi, and Phillips in 1997, Cornell, Wieman, and Ketterle in 2001, and Haroche and Wineland in 2012 [51] [52] [53].

3.4.1 Doppler cooling

We will use the simplest form of laser cooling, known as Doppler cooling. First, consider an atom absorbing an incident photon, then spontaneously emitting a photon in a random direction. The atom will gain the photon momentum $\hbar\mathbf{k}$ and receive a momentum kick $\hbar\mathbf{k}$ in a direction opposite the emitted photon where $\mathbf{k}$ has magnitude $2\pi/\lambda$ and direction in the direction of photon propagation. When continuously hit with a laser with frequency near the resonant frequency of the transition, the atom will continue to absorb momentum kicks in the direction of the laser. For now, we neglect the random recoil kicks due to spontaneous emission as these kicks will average to zero over a sufficient number of cycles. Prior to determining the rate of absorption and emission, let's define a few relevant parameters. $I_{\text{sat}} = \frac{\pi hc}{3\lambda^3\tau} \approx 4.1\,\text{mW}\,\text{cm}^{-2}$ is the saturation intensity of the $^3P_2 \rightarrow^3 D_3$ transition, $\tau \approx 19.4\,\text{ns}$ is the natural lifetime of the $^3D_3$ state, and $\gamma = \frac{1}{\tau} \approx 2\pi \times 8.18\,\text{MHz}$ is the decay rate of the $^3D_3$ state. The rate γ_s at which an atom will absorb incoming photons depends on the intensity of the laser as well as its observed detuning δ from the resonant frequency of the transition:

$$\gamma_s = \frac{I/I_{\text{sat}} \times \gamma/2}{1 + I/I_{\text{sat}} + (2\delta/\gamma)^2}. \tag{3.4}$$

The total radiation force on an atom will be given by the product of the photon momentum and the scattering rate:

$$\mathbf{F} = \gamma_s \hbar \mathbf{k} = \frac{I/I_{\text{sat}} \times \gamma/2}{1 + I/I_{\text{sat}} + (2\delta/\gamma)^2} \times \hbar \mathbf{k}. \tag{3.5}$$

To understand how this radiation force can be useful for cooling, consider a red detuned laser incident an atom moving towards the laser in the lab frame. The observed frequency of the incident beam will be blue shifted in the frame of the moving atom by an amount $\mathbf{k} \cdot \mathbf{v}$ due to the Doppler shift. $\mathbf{v}$ is relative to the lab frame. $\delta = \delta_0 - \mathbf{k} \cdot \mathbf{v}$ where δ_0 is the detuning of the laser in the lab frame. Red detuning corresponds to negative δ_0 and blue detuning corresponds to positive δ_0.

$$\mathbf{F} = \gamma_s \hbar \mathbf{k} = \frac{I/I_{\text{sat}} \times \gamma/2}{1 + I/I_{\text{sat}} + (2(\delta_0 - \mathbf{v} \cdot \mathbf{k})/\gamma)^2} \times \hbar \mathbf{k} \tag{3.6}$$

If the detuning and the Doppler shift are equal and opposite, the atom will feel a force opposite its velocity, slowing it down and reducing its kinetic energy in the lab frame. Temperature is a measure of average kinetic energy of an ensemble of atoms, thus reducing the kinetic energies of the atoms through radiation pressure will reduce the temperature of the ensemble.

Next we consider the force on atom when we add a second counterpropagating laser with detuning and intensity identical to the first. Mathematically, we add a term identical to the single laser case, but with $\mathbf{k}$ replaced with $-\mathbf{k}$:

$$\mathbf{F} = \frac{I}{I_{\text{sat}}} \times \frac{\gamma}{2} \times \hbar \mathbf{k} \left(\frac{1}{1 + \frac{I}{I_{\text{sat}}} + (2(\delta_0 - \mathbf{v} \cdot \mathbf{k})/\gamma)^2} - \frac{1}{1 + \frac{I}{I_{\text{sat}}} + (2(\delta_0 + \mathbf{v} \cdot \mathbf{k})/\gamma)^2} \right). \tag{3.7}$$

This equation can be reduced to

$$\mathbf{F} = \frac{I}{I_{\text{sat}}} \times \frac{\gamma}{2} \times \hbar \mathbf{k} \frac{16 \delta_0 \mathbf{v} \cdot \mathbf{k} \gamma^{-2}}{(1 + \frac{I}{I_{\text{sat}}} + (2(\delta_0 - \mathbf{v} \cdot \mathbf{k})/\gamma)^2)(1 + \frac{I}{I_{\text{sat}}} + (2(\delta_0 + \mathbf{v} \cdot \mathbf{k})/\gamma)^2)}. \tag{3.8}$$

To first order in $\mathbf{v}$:

$$\mathbf{F} \approx \frac{8 \frac{I}{I_{\text{sat}}} \times \frac{\delta_0}{\gamma} \times \hbar \mathbf{k} (\mathbf{v} \cdot \mathbf{k})}{(1 + \frac{I}{I_{\text{sat}}} + (2\delta_0/\gamma)^2)^2}. \tag{3.9}$$

Along the direction of propagation:

$$F \approx \frac{8 \frac{I}{I_{\text{sat}}} \times \frac{\delta_0}{\gamma} \times \hbar \times k^2}{(1 + \frac{I}{I_{\text{sat}}} + (2\delta_0/\gamma)^2)^2} v \approx \beta v, \tag{3.10}$$

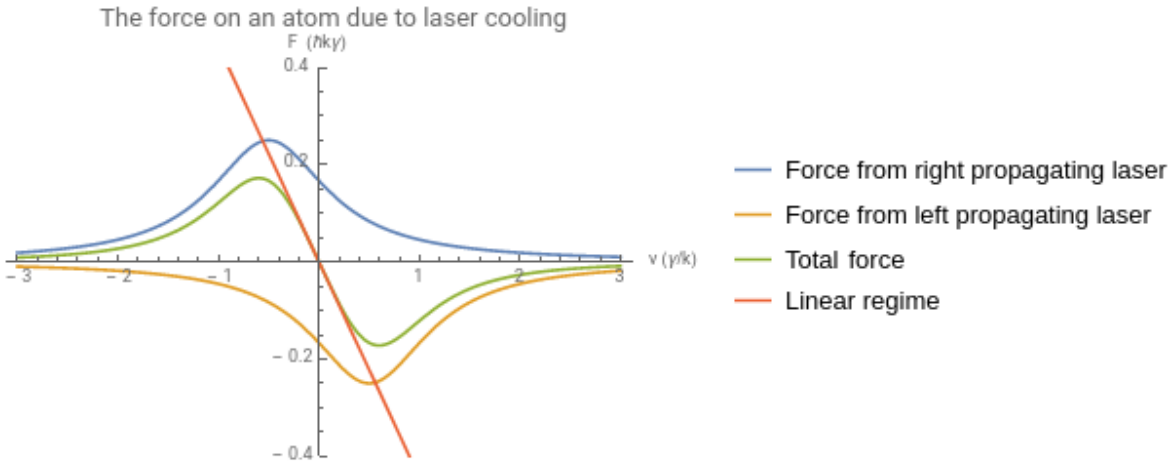

Figure 3.12: The force on atom due to laser(s) detuned by $\delta = -\gamma/2$ with intensity $I = I_{\text{Sat}}$.

where

$$\beta = \frac{8\frac{I}{I_{\text{sat}}} \times \frac{\delta_0}{\gamma} \times \hbar \times k^2}{(1 + \frac{I}{I_{\text{sat}}} + (2\delta_0/\gamma)^2)^2}. \tag{3.11}$$

The velocity dependent forces on an atom from each laser and the total velocity dependent force are shown in Figure 3.12.

As temperature is a measure of average kinetic energy, we treat cooling as kinetic energy lost per unit time:

$$\frac{\partial E}{\partial t}|_{\text{cooling}} = \mathbf{F} \cdot \mathbf{v} \approx \beta |\mathbf{v}|^2. \tag{3.12}$$

To calculate the equilibrium expectation value of kinetic energy, we equate the cooling rate to the heating rate due to the momentum kicks from the incoming photon and the randomly oriented recoil kicks. While the recoil kicks do not affect the expectation value of the momentum, they do add $2\frac{(\hbar k)^2}{2m}$ to the kinetic energy expectation value. m is the atomic mass, in this case the mass of neon $m \approx 20 \times 1.67 \times 10^{-27}\,\text{kg}$ The equilibrium scattering rate is the sum of scattering rates of each of the two lasers. As the scattering rates are equal, this will be twice the scattering rate found in 3.4:

$$2\gamma_s = \frac{I/I_{\text{sat}} \times \gamma}{1 + I/I_{\text{sat}} + (2\delta_0/\gamma)^2}. \tag{3.13}$$

The heating rate is given by

$$\frac{\partial E}{\partial t}|_{\text{heating}} = \frac{(\hbar k)^2}{m}\frac{I/I_{\text{sat}} \times \gamma}{1 + I/I_{\text{sat}} + (2\delta_0/\gamma)^2}. \tag{3.14}$$

Equilibrium will be reached when $\frac{\partial E}{\partial t}|_{\text{cooling}} = \frac{\partial E}{\partial t}|_{\text{heating}}$:

$$\frac{8\frac{I}{I_{\text{sat}}} \times \frac{\delta_0}{\gamma} \times \hbar \times k^2}{(1 + \frac{I}{I_{\text{sat}}} + (2\delta_0/\gamma)^2)^2}|\mathbf{v}|^2 = \frac{(\hbar k)^2}{m}\frac{I/I_{\text{sat}} \times \gamma}{1 + I/I_{\text{sat}} + (2\delta_0/\gamma)^2}. \tag{3.15}$$

Solving for $\frac{1}{2}m|\mathbf{v}|^2$ gives

$$\frac{1}{2}m|\mathbf{v}|^2 = (1 + I/I_{\text{sat}} + (2\delta_0/\gamma)^2)\frac{\hbar}{16}\frac{\gamma^2}{\delta_0}. \tag{3.16}$$

This kinetic energy is minimized when the detuning is given by

$$\delta_0 = \frac{\gamma}{2}\sqrt{1 + \frac{I}{I_{\text{Sat}}}}. \tag{3.17}$$

In the limit of small I, the kinetic energy will correspond to the Doppler limit, the lowest temperature that can be achieved through Doppler cooling:

$$\frac{1}{2}mv^2_{\text{Doppler}} = \frac{1}{2}k_B T = \frac{\hbar\gamma}{4}, \tag{3.18}$$

where k_B is Boltzmann's constant.

The Doppler limits for velocity and temperature are given by

$$v_{\text{Doppler}} = \sqrt{\frac{\hbar\gamma}{2m}} \tag{3.19}$$

and

$$T_{\text{Doppler}} = \frac{\hbar\gamma}{2k_B}. \tag{3.20}$$

The constant of proportionality β in the velocity dependent force equation $F \propto -\beta v$ is given by

$$\beta = \frac{1}{2}\hbar k^2. \tag{3.21}$$

Plugging in values for neon:

$$v_{\text{Doppler}} \approx 28.5\,\text{cm}\,\text{s}^{-1}. \tag{3.22}$$

$$T_{\text{Doppler}} \approx 196\,\mu\text{K}. \tag{3.23}$$

No matter how well Doppler cooling works, we will not be able to cool our atomic beam below these limits. There are several other methods for laser cooling below the Doppler limit including polarization gradient cooling, Raman cooling, and Magneto-optical cooling which as of this writing is currently under development on the other side of the Raizen lab [55] [56] [57].

3.4.2 Doppler cooling in the moving frame

The previous section discussed Doppler cooling in a dimension in which the average velocity of atoms is zero in the lab frame. This is relevant for cooling trapped atoms (which we don't do) and transversely cooling a moving beam (which we do.) To longitudinally cool the beam, we must shift the frequency of the cooling lasers into the moving frame. Due to geometric constraints, we use a single longitudinal cooling laser to push the atoms with the highest velocities into the velocity class with most atoms. This increases the peak density of atoms with respect to velocity. This will be further covered in the chapter on experimental setup.

Our atomic beam moves with a mean velocity of 490 m s To calculate the detuning necessary, use the relation $\frac{v}{c} = \frac{\Delta\nu}{\nu}$.

$$\Delta\nu = \frac{v\nu}{c} = \frac{v}{\lambda} \approx 766\,\text{MHz}. \tag{3.24}$$

The frequency of the laser diode is 40 MHz below resonance in the lab frame, thus we need to shift the frequency by an additional 726 MHz to reach resonance in the moving frame or 730 MHz to reach $\delta_0 = -\frac{\gamma}{2}$. To create this rather large shift, we use a double pass configuration as shown in Figure 3.13. We pass the laser through an AOM twice, each pass shifting the frequency by $730\,\text{MHz}/2 = 365\,\text{MHz}$.

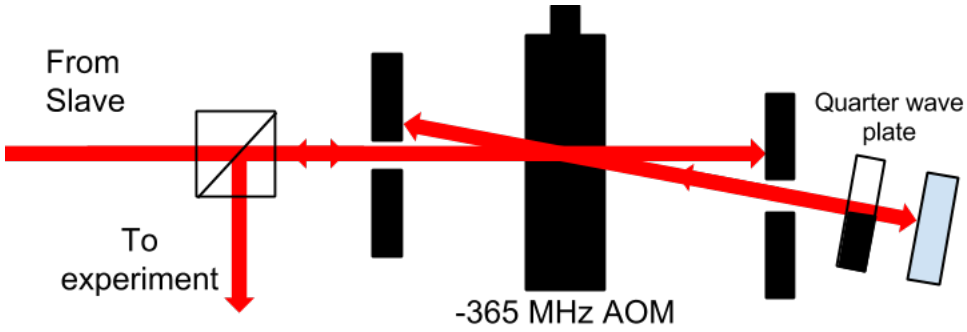

Figure 3.13: A diagram of the double pass configuration. The light passes through a polarizing beam splitter, then deflected and frequency shifted by $-365\,\mathrm{MHz}$ by an AOM. It is then retroreflected back through the AOM and frequency shifted by another $-365\,\mathrm{MHz}$. A quarter wave plate is added so that the net change in polarization of light upon retroreflection is 90 degrees. As drawn, light would enter through the cube with vertical polarization $\updownarrow$ and then be reflected by the cube with polarization into and out of the page $\otimes$.

Chapter Four: Magnetic forces on neutral atoms

The energy of a magnetic dipole in a magnetic field is given by $U = -\boldsymbol{\mu} \cdot \mathbf{B}$. The force on a magnetic dipole is therefore

$$\mathbf{F} = -\nabla U = \nabla(\boldsymbol{\mu} \cdot \mathbf{B}). \tag{4.1}$$

For atoms, the magnetic dipole moment is $\mu = -m_j g_j \mu_B$, therefore the force on a neutral atom is

$$\mathbf{F} = \nabla(-m_j g_j \mu_B \hat{\mu} \cdot \mathbf{B}). \tag{4.2}$$

An important phenomenon of atomic motion in an inhomogenous magnetic field is adiabatic following. If the direction of the magnetic field changes significantly slower than the Larmor frequency $\frac{\partial \hat{B}}{\partial t} << \omega_L = \frac{\mu |B|}{\hbar}$, the direction of the magnetic moment will change with the direction of the magnetic field, thus preserving its value of m_j.

For atoms with positive g_j including neon, atoms with positive m_j will be attracted to points of minimum magnetic field strength, while atoms with negative m_j will be attracted to points of maximum magnetic field strength. We refer to these states as low-field seeking and high-field seeking respectively.

$$\mathbf{F} = -m_j g_j \mu_B \nabla(\hat{\mu} \cdot \mathbf{B}). \tag{4.3}$$

But due to adiabatic following, we know that $\boldsymbol{\mu}$ and $\mathbf{B}$ must point in the same direction. Therefore $\hat{\mu} \cdot \mathbf{B} = |\mathbf{B}|$,

$$\mathbf{F} = -m_j g_j \mu_B \nabla |\mathbf{B}|. \tag{4.4}$$

This is a very interesting result. The force on a magnetic dipole does not depend whatsoever on the direction of the magnetic field, but solely on the gradient of its magnitude.

4.1 Magnetic n-poles

In this section, I will discuss various geometries of magnets that give rise to useful magnetic fields.

4.1.1 Coaxial coils

The most common configuration of coaxial coils are the Helmholtz and anti-Helmholtz configurations. Both involve two identical coaxial circular coils separated a distance equal to their radius. In the Helmholtz configuration, the current is flowing in the same direction in each coil while in the anti-Helmholtz configuration, the direction of the current is flipped in one of the coils. We will also discuss systems of three and four coaxial coils.

Note, for the remainder of this chapter, all math will be done under the assumption that each coil is a single current loop, but the math does not change if each coil consists of many loops. In the case, simply make the transformation $I \to nI$ where I is the current and n is the number of loops in each coil.

4.1.1.1 Dipoles

We will start by analyzing the Helmholtz case.

The magnetic field in the axial direction along the axis of a single coil of radius r and current I on the $z = 0$ plane is

$$B_z = \frac{\mu_0 I r^2}{2} \frac{1}{(z^2 + r^2)^{3/2}}. \tag{4.5}$$

For two coils with current in the same direction, one located in the $z = -\frac{a}{2}$ plane and one located in the $z = +\frac{a}{2}$ plane, the sum of the magnetic fields will be

$$B_z = \frac{\mu_0 I r^2}{2} \left(\frac{1}{((z - \frac{a}{2})^2 + r^2)^{3/2}} + \frac{1}{((z + \frac{a}{2})^2 + r^2)^{3/2}}\right). \tag{4.6}$$

Taking a series expansion neglecting terms fourth order and higher gives

$$B_z = \mu_0 I r^2 \left(\frac{8}{(a^2 + 4r^2)^{\frac{3}{2}}} + \frac{192(a^2 - r^2)}{(a^2 + 4r^2)^{\frac{7}{2}}} z^2 + \mathcal{O}(z^4)\right). \tag{4.7}$$

A couple interesting things to note: As the geometry is symmetric about the $z = 0$ plane, only even powers of z will be nonzero. If $a = r$, the z^2 term will vanish,

leaving only the z^0 term and terms of order z^4 or higher. This special case is the Helmholtz configuration. This configuration is particularly useful for creating nearly homogeneous magnetic bias fields for optical pumping. The on axis field is shown in Figure 4.1 while the approximate off-axis magnetic field is shown in Figure 4.2.

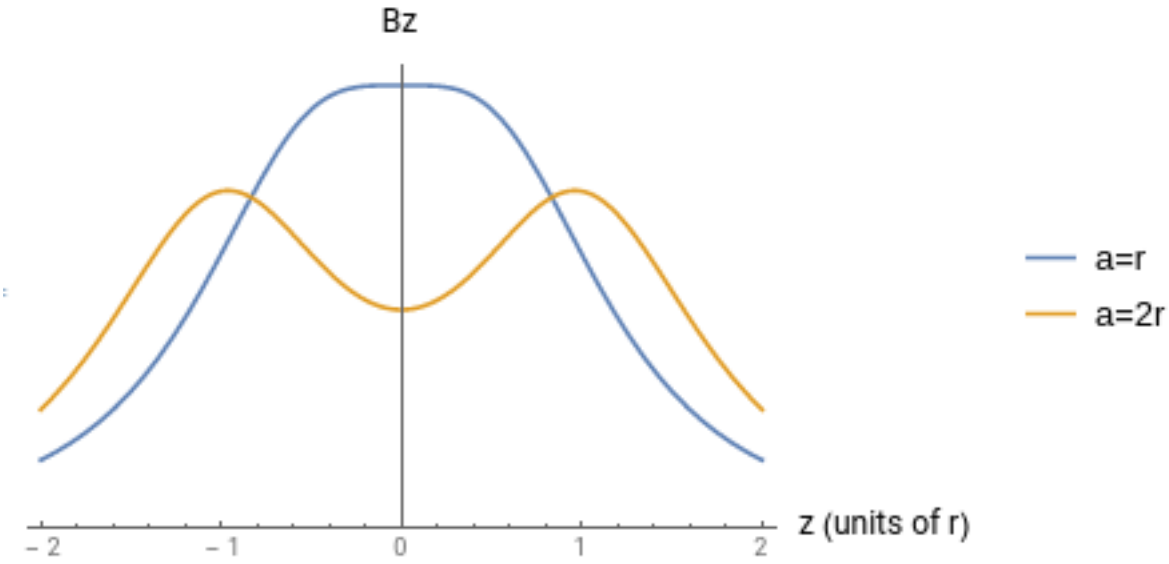

Figure 4.1: The magnetic field in the axial direction for two coils with current in the same direction. If the separation between the coils is equal to the radius, the magnetic field strength will be nearly constant over a wide range.

This equation only holds along the axis of the magnetic field. To calculate the magnetic field everywhere is a surprisingly difficult problem, however we can easily approximate the field in the vicinity of the axis using Gauss's law for magnetism and Ampere's law. This approximation will yield a power series in the distance from the axis, ρ, so we will denote each term in the series by its power of ρ.

First, we know the magnetic field must satisfy Gauss's law for magnetism. In cylindrical coordinates, this is

$$\nabla \cdot \mathbf{B} = \frac{\partial B_z}{\partial z} + \frac{1}{\rho}\frac{\partial \rho B_\rho}{\partial \rho} = 0. \tag{4.8}$$

$$B_\rho = -\frac{1}{\rho}\int \rho \frac{\partial B_z}{\partial z} d\rho \tag{4.9}$$

We do not know the full form of B_z over all space, but we do know it along the z axis, for which $\rho = 0$. This is the B_0 term. I will also switch to prime notation for derivatives. Note, all primes correspond to derivatives with respect to z.

$$B_{\rho 1} = -\frac{1}{\rho}\int \rho B_{z0}' d\rho = -\frac{1}{2}\rho B_{z0}' \tag{4.10}$$

To find the B_2 term, we use Ampere's law with no free currents or time varying electric fields:

$$\nabla \times \mathbf{B} = \frac{\partial B_\rho}{\partial z} - \frac{\partial B_z}{\partial \rho} = 0. \tag{4.11}$$

$$B_{z2} = \int \frac{\partial B_{\rho 1}}{\partial z} d\rho = \int -\frac{1}{2}\rho B_{z0}'' d\rho = -\frac{1}{4}\rho^2 B_z'' \tag{4.12}$$

The total magnetic field is the sum of each term in the power series. The power series will quickly converge to the exact field for $\rho < r$.

$$\mathbf{B} = (B_{z0} - \frac{1}{4}\rho^2 B_{z0}'')\hat{z} - \frac{1}{2}\rho B_{z0}'\hat{\rho} + \mathcal{O}(\rho^3) \tag{4.13}$$

If desired, further terms can be found iteratively:

$$B_{(n+2)z} = -B_{nz}\frac{B^{n+2'}}{B^{n'}}\frac{\rho^2}{(n+2)^2}. \tag{4.14}$$

$$B_{(n+2)\rho} = -B_{n\rho}\frac{B^{n+2'}}{B^{n'}}\frac{\rho^2}{(n+1)(n+3)} \tag{4.15}$$

For Helmholtz coils separated by a distance equal to their radius, to lowest order in ρ and z, in the neighborhood of $z = 0$ and $\rho = 0$,

$$\mathbf{B} \approx \frac{\mu_0 I}{5\sqrt{5}r}\hat{z}. \tag{4.16}$$

Note that this field is of zeroth order in both z and ρ. We refer to this field as a dipole field. Also of note, the single coil produces a magnetic field with lowest term of zeroth order, thus the minimum number of coils to produce a dipole is one. Because the dipole field has no gradient, it will not provide a force on atoms inside it. This is an added benefit, or at least not a detriment, to using Helmholtz coils as a means of creating a bias magnetic field for optical pumping.

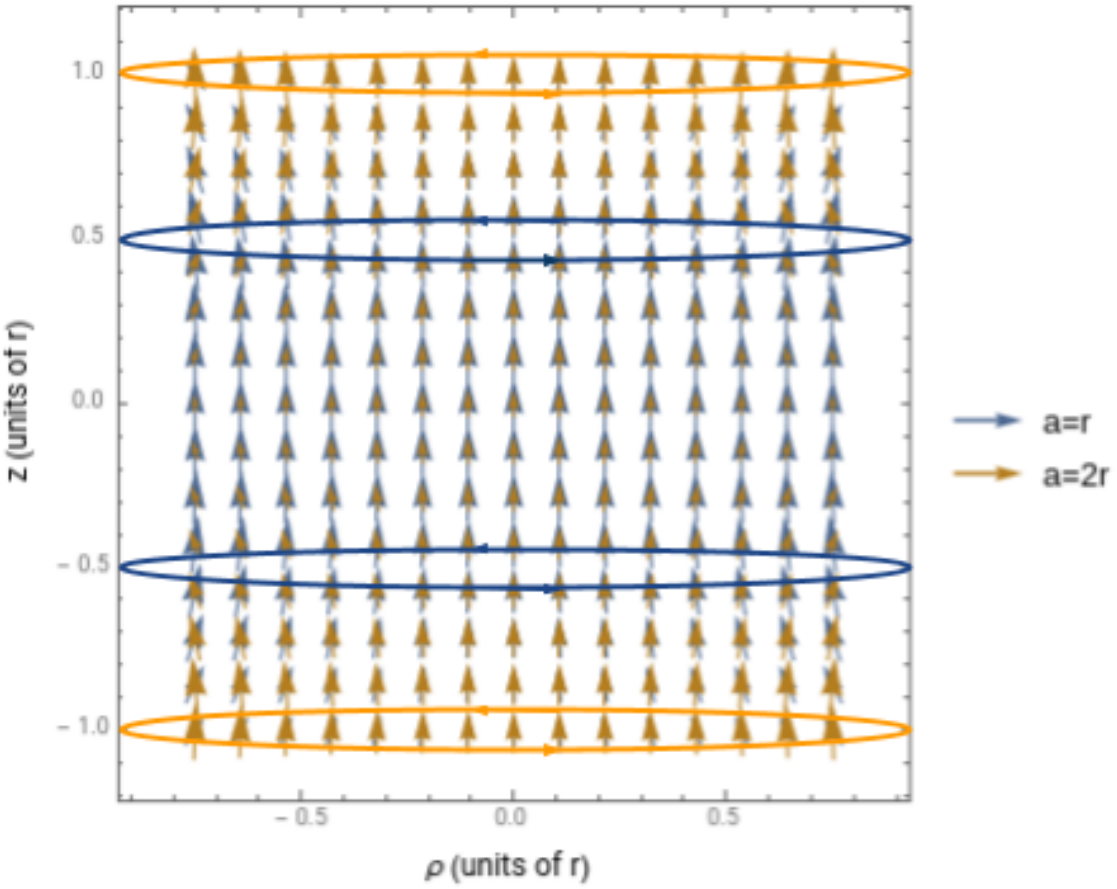

Figure 4.2: The approximate magnetic field for two coils with current in the same direction. If the separation between the coils is equal to the radius, the magnetic field will be nearly homogeneous over a wide range. The blue and orange ovals represent the locations of current loops for spacings $a = r$ and $a = 2r$ respectively.

4.1.1.2 Quadrupoles

We will next consider the magnetic field due to two coaxial coils with currents flowing in opposite directions. Again, we will use two coils of radius r, carrying current I, one in the $z = \frac{a}{2}$ plane and one in the $z = -\frac{a}{2}$ plane.

While quadrupoles are not used in our experiment, they are very useful for other atomic physics experiments including magneto-optical trapping and magnetic slowing [3] [51].

$$B_z = \frac{\mu_0 I r^2}{2}\left(\frac{1}{((z-\frac{a}{2})^2+r^2)^{3/2}} - \frac{1}{((z+\frac{a}{2})^2+r^2)^{3/2}}\right) \tag{4.17}$$

Taking a series expansion neglecting terms fourth order and higher gives

$$B_z = \mu_0 I r^2\left(\frac{48a}{(a^2+4r^2)^{\frac{5}{2}}}z + \frac{640(a^3-3ar^2)}{(a^2+4r^2)^{\frac{9}{2}}}z^3 + \mathcal{O}(z^5)\right). \tag{4.18}$$

Two ratios of a/r will give interesting results.If $a = \sqrt{3}r$, the z^3 will drop out, however this is not necessary to create a quadrupole field. For fixed r, the coefficient of the leading term will be maximized when $a = r$. This is referred to as the anti-Helmholtz configuration. The axial magnetic field is shown in Figure 4.3 while the off axis magnetic field is shown in Figure 4.4 and the off axis force field on low field seeking atoms is shown in 4.5.

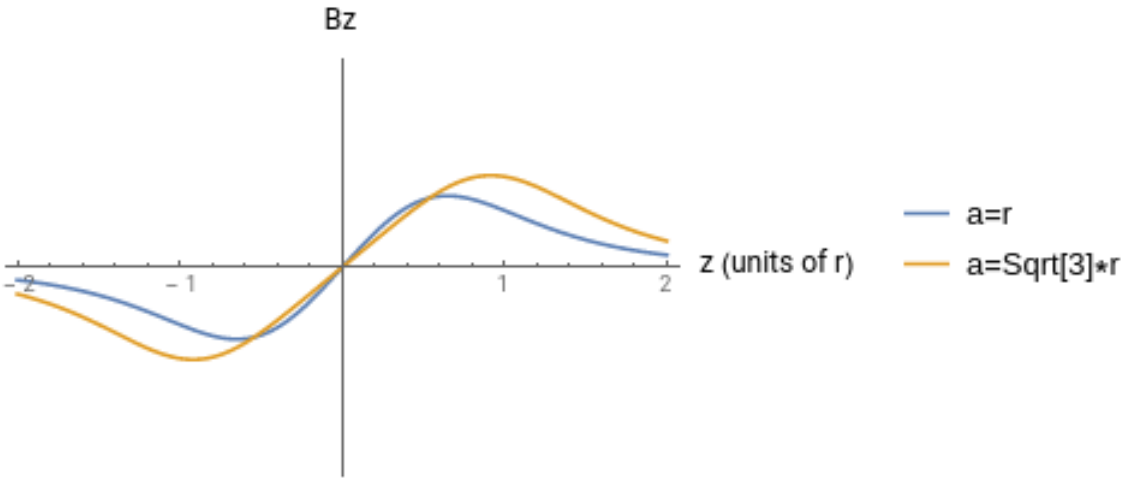

Figure 4.3: The magnetic field in the axial direction for two coils with current in opposite directions. If the separation between the coils is equal to the radius, the gradient of the axial magnetic field will be maximized. If the separation is equal to $\sqrt{3}$ times the coil radii, the regime in which the field is linear in z will be maximized.

To calculate the off axis field, we use the same process as we did for the Helmholtz configuration. Unlike the dipole case, the quadrupole case has a non-negligible derivative at $z = 0$. To first order,

$$B_z' = \mu_0 I r^2 \frac{48a}{(a^2+4r^2)^{\frac{5}{2}}} + \mathcal{O}(z^3). \tag{4.19}$$

$$B_{\rho 1} = -\frac{1}{2}B_z'\rho = \mu_0 I r^2 \frac{-24a}{(a^2+4r^2)^{\frac{5}{2}}}\rho + \mathcal{O}(z^2) \tag{4.20}$$

Summing the components gives a total magnetic field, which to first order is

$$\mathbf{B} \approx \frac{24a\mu_0 I r^2}{(a^2+4r^2)^{\frac{5}{2}}}(2\mathbf{z} - \boldsymbol{\rho}) \tag{4.21}$$

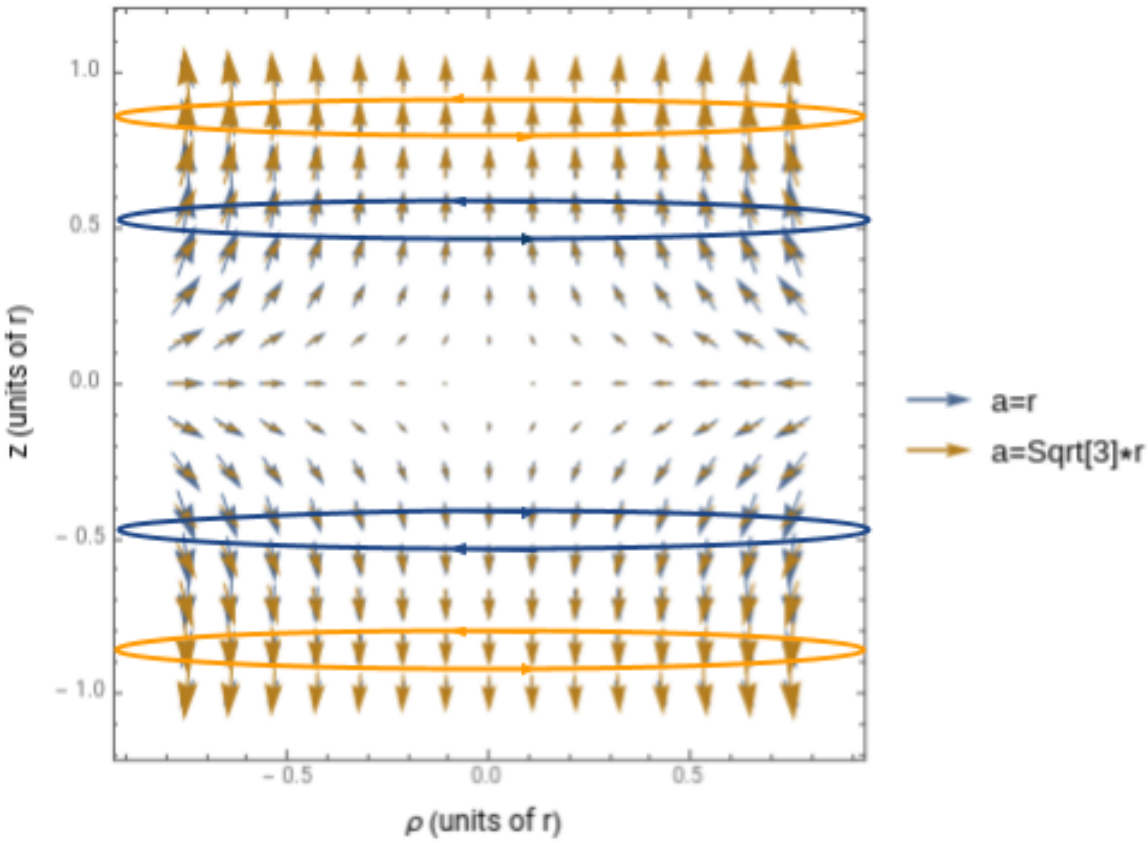

Figure 4.4: The approximate magnetic field for two coils with current in opposite directions. If the separation between the coils is equal to the radius, the magnetic field gradient will be maximized. If the separation is a factor of $\sqrt{3}$ greater than the radius, the linear regime will be maximized. The blue and orange ovals represent the locations of current loops for spacings $a = r$ and $a = \sqrt{3}r$ respectively.

Note that this field is antisymmetric and of first order in both z and ρ. We refer to this field as a quadrupole field. Also of note, it is not possible to produce a quadrupole

field with a single coil, thus the minimum number of coils to produce a quadrupole is two.

When inside a quadrupole, atoms will feel a force

$$\mathbf{F} = -\mu_B m_j g_j \nabla|\mathbf{B}| \approx -\mu_B m_j g_j \nabla|\frac{24a\mu_0 I r^2}{(a^2+4r^2)^{\frac{5}{2}}}(2\mathbf{z}-\boldsymbol{\rho})|. \tag{4.22}$$

$$\mathbf{F} \approx -\mu_B m_j g_j \frac{24a\mu_0 I r^2}{(a^2+4r^2)^{\frac{5}{2}}}\nabla\sqrt{4z^2+\rho^2} \tag{4.23}$$

On either the z axis or the z=0 plane, low field seeking atoms will feel a force toward the origin of constant magnitude, while high field seeking atoms will feel a force away from the origin, also with constant magnitude, which makes sense because that is the region of weakest magnetic field. Otherwise, a coordinate shift can be made such that $z' = 2z$, $\rho' = \rho$, $r' = \sqrt{z'^2+\rho'^2}$ and the force will always point radially toward the origin.

$$\mathbf{F'} \approx -\mu_B m_j g_j \frac{24a\mu_0 I r^2}{(a^2+4r^2)^{\frac{5}{2}}}\nabla' r' \tag{4.24}$$

$$\mathbf{F'} \approx -\mu_B m_j g_j \frac{24a\mu_0 I r^2}{(a^2+4r^2)^{\frac{5}{2}}}\hat{r'} \tag{4.25}$$

This location of the field zero can be moved a few different ways. First, the coils can be moved up or down, causing a corresponding shift in field zero. A set of Helmholtz coils can be added along any dimension to move the perceived field zero in that dimension. For a quadrupole field with magnitude and direction $\mathbf{B_q} = B_q(2z\hat{z} - x\hat{x} - y\hat{y})$. Adding a dipole field $\mathbf{B_d} = B_d(x_0\hat{x} + y_0\hat{y} + z_0\hat{z})$ shifts the field zero by a vector $\frac{B_d}{B_q}(x_0\hat{x} + y_0\hat{y} - 2z_0\hat{z})$. This can be useful for creating a force on atoms that is approximately homogeneous over a large region. When atoms are in an offset quadrupole field far from its effective center, the atoms will feel a force toward the distant quadrupole field zero. Provided the distance is far relative to the extent of the atoms, the force will be approximately one dimensional. The field zero can also be moved by having two different currents passing through the two coils, however this is mathematically equivalent of adding Helmholtz coils of the desired difference in current to the existing anti-Helmholtz coils as shown in Figure 4.6.

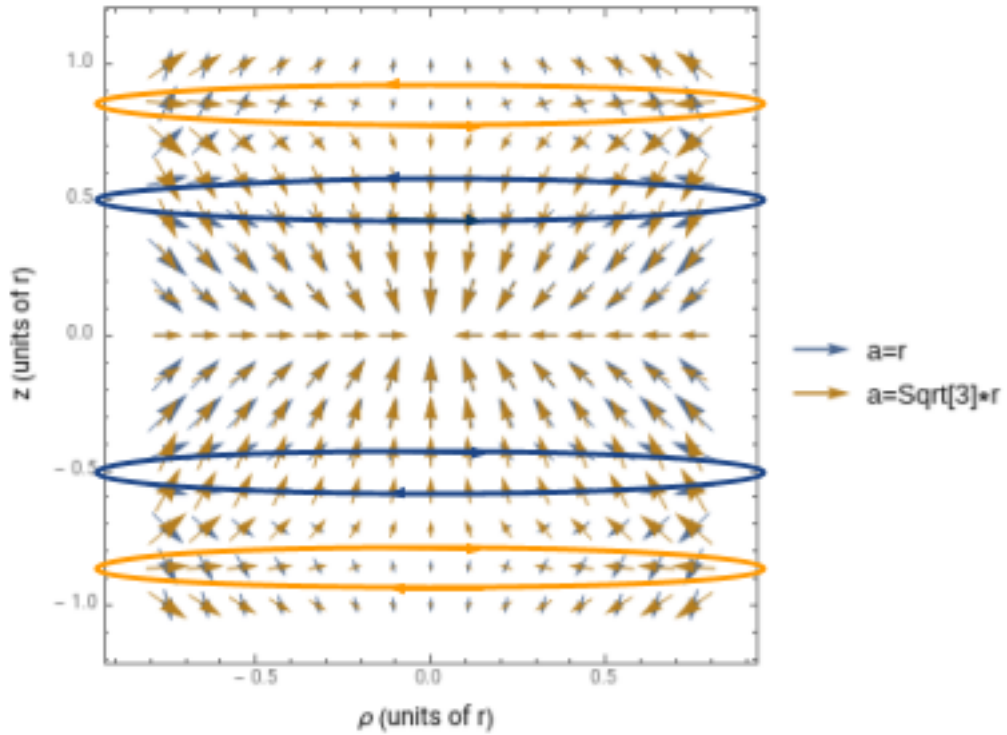

Figure 4.5: The force field on a low field seeking atom in a quadrupole field. Depending on how you scale your axes, in the region enclosed by the coils, the force will generally be towards the center of the configuration

4.1.1.3 Octupoles

Next we consider the case of four identical coils axially separated from the next coil by a distance equal to their radius, with current in alternating directions. The math is the same for arbitrary spacings so long as the system is asymmetric about its central plane. Effectively, the result will be two overlapping quadrupoles, the resulting field of which is shown in Figure 4.7. We can tune the ratio of the current in the outer two coils and the current in the inner two coils to set the linear component of the magnetic field to zero.

Recall for a quadrupole field,

$$B_z = \mu_0 I r^2 \left(\frac{48a}{(a^2+4r^2)^{\frac{5}{2}}} z + \frac{640(a^3-3ar^2)}{(a^2+4r^2)^{\frac{9}{2}}} z^3 + \mathcal{O}(z^5)\right). \tag{4.26}$$

For two overlapping quadrupoles, the inner of which has spacing $a = r$ and current I_1 and the outer has spacing $a = 3r$ and current I_2.

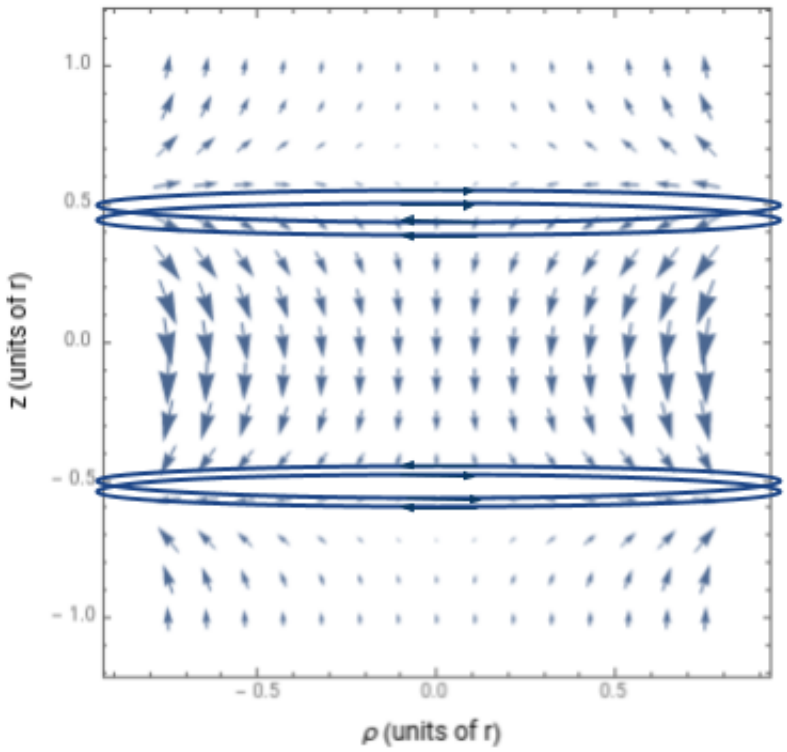

Figure 4.6: The force field on an atom in an offset quadrupole field. This particular field was simulated with identical currents and spacings for a pair of overlapping Helmholtz and anti-Helmholtz coils. This is equivalent to a single coil running twice the original current. Note that the force will be fairly constant over a large region near the center of the coils.

$$B_z = \frac{48\mu_0 z}{r^2}\left(\frac{I_1}{25\sqrt{5}} + \frac{I_2}{169\sqrt{13}}\right) + \mathcal{O}(z^3). \tag{4.27}$$

To cancel out the leading term, set $I_2 = -I_1\frac{169\sqrt{13}}{25\sqrt{5}}$. Plugging the values for the z^3 term gives

$$B_z = \frac{640\mu_0 I_1}{r^4}\left(\frac{-2}{5^{9/2}} - \frac{25\sqrt{5}}{169\sqrt{13}}\frac{18}{13^{9/2}}\right)z^3 + \mathcal{O}(z^5). \tag{4.28}$$

This coefficient is annoyingly bulky and distracts from the larger point of this exercise, which is to show that the z component of the magnetic field increases with the cube of z. From this point I will refer to this coefficient as B_{oct}:

$$B_z = B_{\text{oct}} z^3 + \mathcal{O} z^5. \tag{4.29}$$

Solving for B_ρ in a manner similar to that of the last two sections gives

$$B_{\rho 1} = -\frac{3}{2} B_{\text{oct}} z^2 \rho + \mathcal{O}(z^n)(\rho^{5-n}). \tag{4.30}$$

and

$$B_{z2} = -\frac{3}{2} B_{\text{oct}} z \rho^2 + \mathcal{O}(z^n)(\rho^{5-n}) \tag{4.31}$$

$$B_{\rho 3} = \frac{3}{8} B_{\text{oct}} \rho^3 + \mathcal{O}(z^n)(\rho^{5-n}) \tag{4.32}$$

All together

$$\mathbf{B} \approx B_{\text{oct}}((z^3 - \frac{3}{2} z \rho^2)\hat{z} + (-\frac{3}{2} z^2 \rho + \frac{3}{8} \rho^3)\hat{\rho}). \tag{4.33}$$

Note that this field is antisymmetric and of up to third order in both z and ρ. We refer to this field as a octupole field. Also of note, it is not possible to produce an octupole field with fewer than four coils, thus the minimum number of coils to produce a octupole is four. Along the z axis, low field seeking atoms will feel a force toward the origin, with a magnitude that varies with z^2.

4.1.1.4 Hexapoles?

Summarizing out findings to this point in table form we have:

name	z dependence of B_z	symmetry	minimum coils	force on lfs atoms
dipole	z^0	symmetric	1	$F_z = 0$
quadrupole	z^1	antisymmetric	2	$F_z \propto -\frac{z}{\lvert z \rvert}$
?	?	?	?	?
octupole	z^3	antisymmetric	4	$F_z \propto -z^2$

Clearly, there is something missing in this chart. From our intuition, we're looking for a symmetric field that can be made from three coils and whose axial field strength is proportional to z^2 for small z. This can be made with three equally spaced coaxial coils with current in alternating direction. Set the central coil as on the $z = 0$ plane

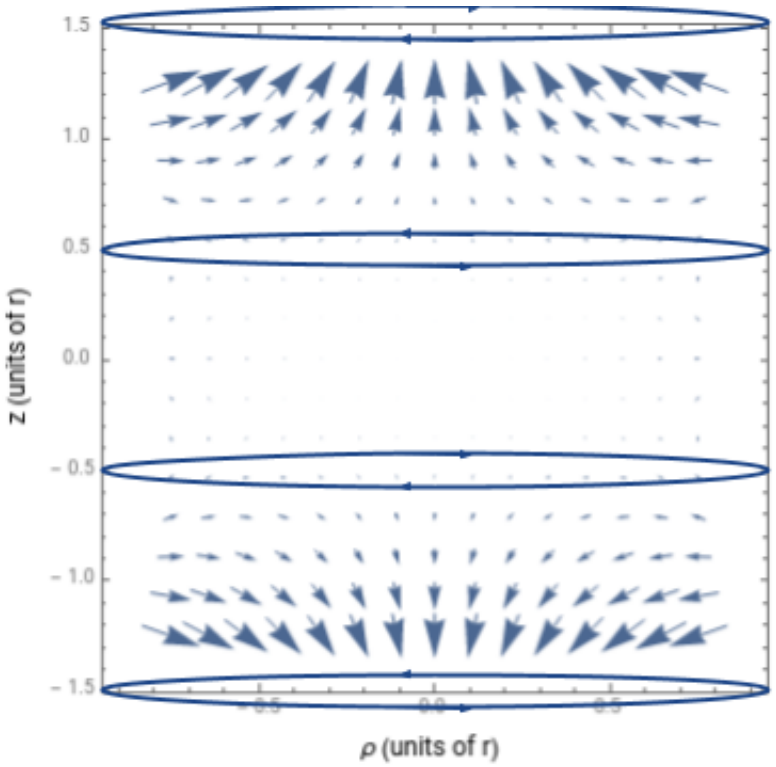

Figure 4.7: The approximate magnetic field for four equally spaced coils with current in alternating directions. If the current in the outside set of coils is a factor of $(\frac{13}{5})^{\frac{5}{2}}$ larger than the current in the inside coils, the quadrupole term will cancel and the leading term will be of order $z^n\rho^{3-n}$.

with current I_2 and the outer coils on the $z = a$ and $z = -a$ planes with current I. The axial magnetic field will be given by:

$$B_z = \frac{\mu_0 r^2}{2}\left(\frac{I}{((z-a)^2+r^2)^{3/2}} + \frac{I}{((z+a)^2+r^2)^{3/2}} - \frac{I_2}{(z^2+r^2)^{3/2}}\right). \tag{4.34}$$

Taking a series expansion neglecting terms fourth order and higher gives

$$B_z = \mu_0\left(\frac{Ir^2}{(a^2+r^2)^{\frac{3}{2}}} - \frac{I_2}{r} + \left(Ir^2\frac{6a^2-\frac{3}{2}r^2}{(a^2+r^2)^{\frac{7}{2}}} + \frac{3I_2}{4r^3}\right)z^2 + \mathcal{O}(z^4)\right). \tag{4.35}$$

We want the ratios I_2/I and a/r that maximize the z^2 coefficient and zero the z^0 coefficient. Using an equation solver and taking the nontrivial solutions gives us these ratios. $I_2 = \frac{16}{7\sqrt{7}}I$ and $a = \frac{\sqrt{3}}{2}r$. Plugging in these ratios gives

$$B_z = \frac{972\mu_0 I z^2}{343\sqrt{7}r^3} \tag{4.36}$$

The axial magnetic field strength is shown in Figure 4.8, the off-axis field in Figure 4.9, and the force field on low field seeking atoms is shown in 4.10.

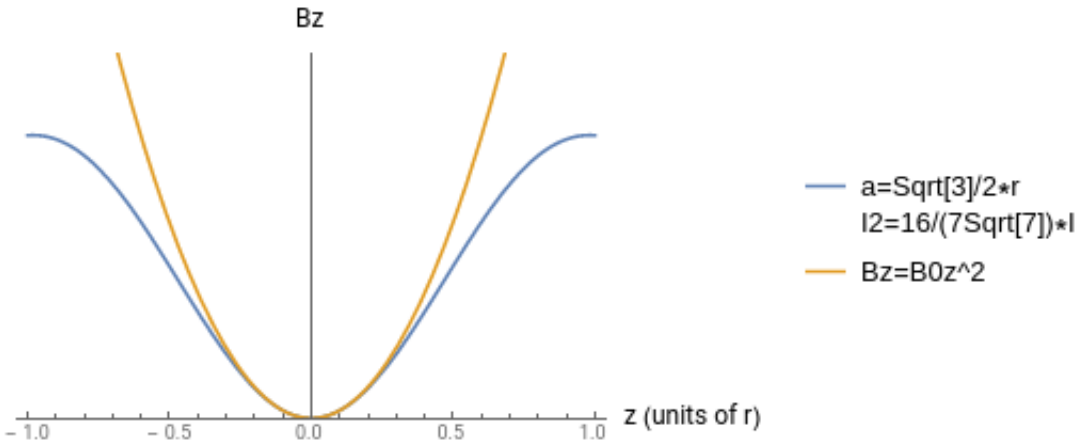

Figure 4.8: The magnetic field in the axial direction for three coils with current in alternating directions. Each coil is spaced from the next by a distance $\frac{\sqrt{3}}{2}r$. The inside coil has current a factor of $\frac{16}{7\sqrt{7}}$ greater than that of the outside coils. Shown next to a parabola for comparison. The range at which this approximation is valid can be extended by increasing the distance between the coils and decreasing the current in the central coil, but this will also serve to decrease the z^2 dependence of the axial magnetic field.

We approximate the off axis fields using the same equations we used for the dipole, quadrupole and octupole fields.

Note that this field is symmetric and of up to second order in both z and ρ. We refer to this field as a hexapole field. Also of note, it is not possible to produce a hexapole field with fewer than three coils, thus the minimum number of coils to produce a hexapole is three. Along the z axis, low field seeking atoms will feel a force toward the origin, with a magnitude that varies with z.

The linear force dependence on z is the most useful aspect of the magnetic hexapole for it gives us the famous equation of $F_z \propto -z$ of simple harmonic motion. It turns out, this is also the equation necessary for an atom lens as will be discussed further in the upcoming chapters.

We return to our table from earlier in this section and fill in its holes.

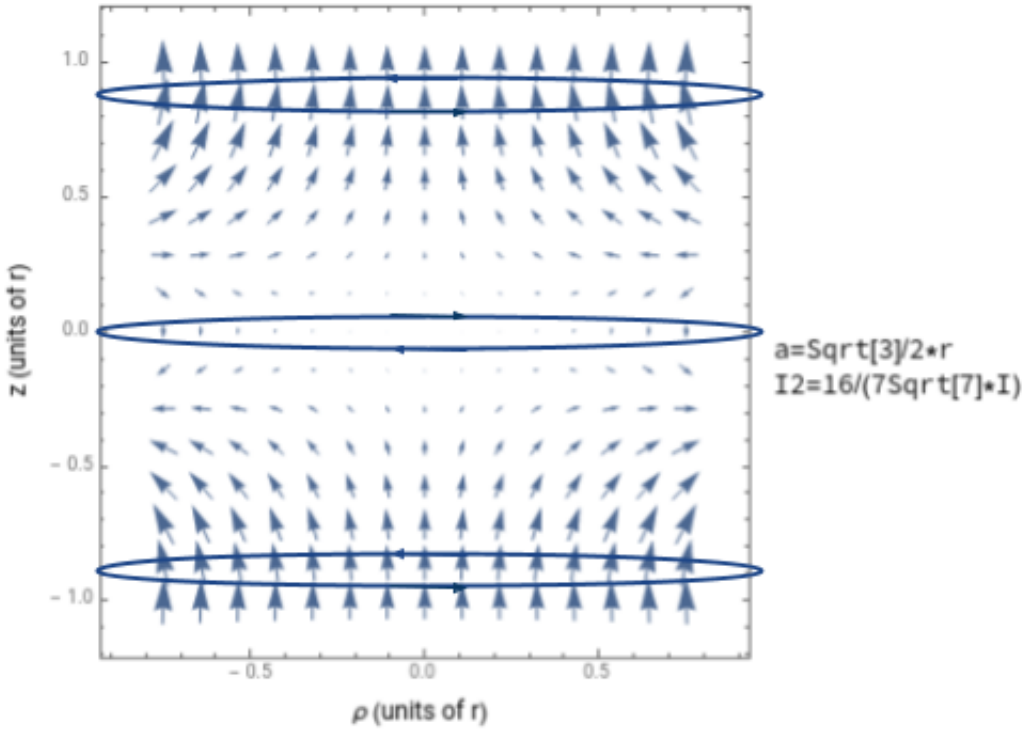

Figure 4.9: The approximate magnetic field for three coils with current in alternating directions. If the separation between the coils is equal to $\frac{\sqrt{3}}{2}$ times the radius and the current in the inside coils is a factor of $\frac{16}{7\sqrt{7}}$ greater than the current in the outside coils, the coefficient of the z^2 term of the axial magnetic field strength will be maximized and the coefficient for the z^0 term will be zero.

name	z dependence of B_z	symmetry	minimum coils	force on lfs atoms
dipole	z^0	symmetric	1	$F_z = 0$
quadrupole	z^1	antisymmetric	2	$F_z \propto -\frac{z}{\|z\|}$
hexapole	z^2	symmetric	3	F$\propto -z$
octupole	z^3	antisymmetric	4	$F_z \propto -z^2$

4.1.2 Permanent magnets

The magnetic fields of permanent magnets are significantly harder to solve analytically than those of their coaxial electromagnetic counterparts, but can generally be solved numerically. Finite element modeling software such as COMSOL can be very helpful, however a numerical solver such as Mathematica or Matlab can do the job.

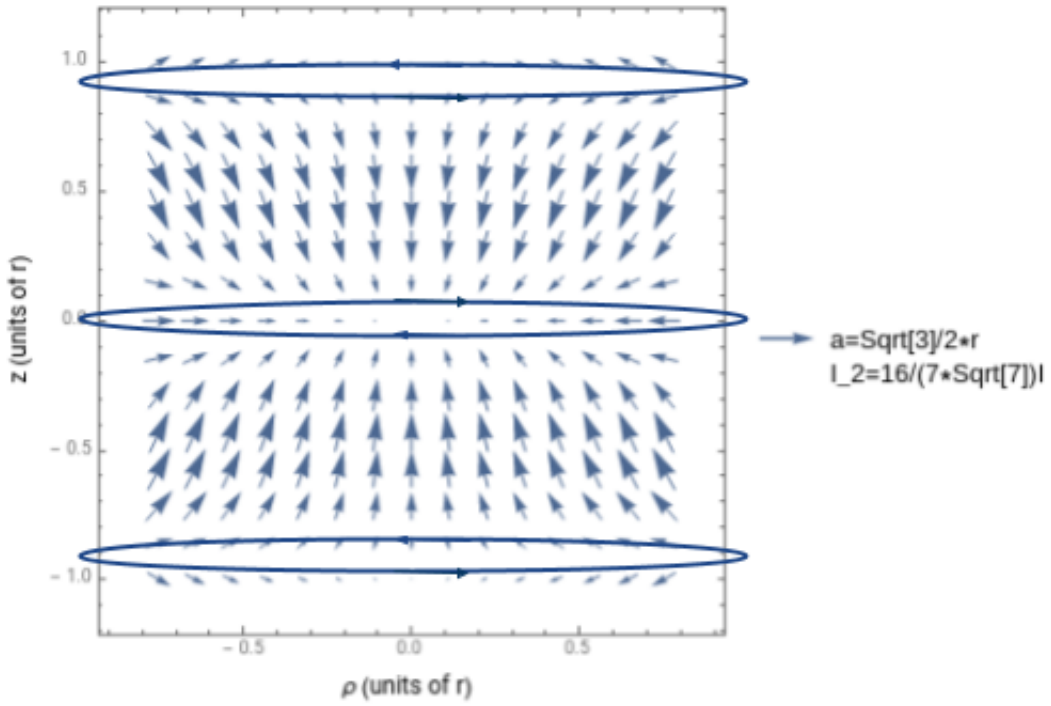

Figure 4.10: The force field on low field seeking atoms inside a hexapole field. Along the z axis and near the origin, atoms will feel a force toward the origin with strength proportional to its distance from the origin.

Because I am most familiar with Mathematica, that's what I use.

The magnetic field of a permanent magnet can be found by integrating the magnetic field created by a dipole at each point within the magnet

$$\mathbf{B}(\mathbf{r}) = \frac{\mu_0}{4\pi} \int_{V'} dx'^3 \frac{3\mathbf{n}(\mathbf{n}\cdot\mathbf{m}) - \mathbf{m}}{|\mathbf{r}-\mathbf{r}'|^3}, \tag{4.37}$$

where **r** is the point at which the magnetic field is measured, **r'** is the point inside in the magnet creating the field, **m** is the local magnetization, and **n** is the unit vector pointing toward the measurement point $\mathbf{n} = \frac{\mathbf{r}-\mathbf{r}'}{|\mathbf{r}-\mathbf{r}'|}$.

We start our analysis by finding the magnetic field from a single magnet. We will use magnets of rectangular cross section of width w and thickness t for our analysis, both for simplicity and because we use rectangular magnets in the experiment itself.

To limit the magnetic field to two dimensions, we assume the magnets are of infinite length. We also assume that the magnetic moment lies along the thickness axis. Let's label the thickness coordinate as y, the width coordinate as x and the

length coordinate as z. The top of the magnet will be at position $z' = -a$ and the bottom will be at position $z' = -a - t$.

$$\mathbf{B}(\mathbf{r}) = \frac{\mu_0}{4\pi} \int_{-\infty}^{\infty} dz' \int_{-w/2}^{w/2} dx' \int_{-a-t}^{-a} dy' \frac{3\mathbf{n}(\mathbf{n}\cdot\mathbf{m}) - \mathbf{m}}{|\mathbf{r} - \mathbf{r}'|^3} \tag{4.38}$$

We assume that the width as small enough that the y' integral can be approximated as a product of $w\mathbf{B}(r')$. We start by finding the magnetic field along the y axis and using Maxwell's equations to find the field off axis and plot it in Figure 4.11.

$$B_{y0}(y) = \frac{\mu_0}{4\pi} w \int_{-\infty}^{\infty} dz' \int_{-a-t}^{-a} dy' \frac{m(\frac{(y-y')^2}{(y-y')^2+z'^2} - 1)}{((y-y')^2 + (z')^2)^{\frac{3}{2}}} \tag{4.39}$$

$$B_{y0}(y) \approx \frac{\mu_0 m w t}{2\pi(a+y)(a+t+y)} \tag{4.40}$$

By symmetry there will not a component of the magnetic field in the z direction. By applying Gauss's law for magnetism we get

$$\nabla \cdot \mathbf{B} \approx B_{y0}(y)' + \frac{\partial}{\partial x} B_{x1} = 0. \tag{4.41}$$

$$B_{x1} = -x B_{y0}'(y) \tag{4.42}$$

and applying Faraday's law we get

$$\nabla \times \mathbf{B} \approx \frac{\partial}{\partial y} B_{x1} + \frac{\partial}{\partial x} B_{y2}, \tag{4.43}$$

$$B_{y2} = -\frac{1}{2} x^2 B_{y0}''(y), \tag{4.44}$$

and,

$$\mathbf{B} \approx -x B_{y0}'(y)\hat{x} + (B_{y0}(y) - \frac{x^2}{2} B_{0y}''(y))\hat{y}. \tag{4.45}$$

For the remainder of this section, we will use this field as the approximate magnetic field due to one magnet and provide a coordinate transformation to find the total magnetic field of a set of identical magnets at different positions.

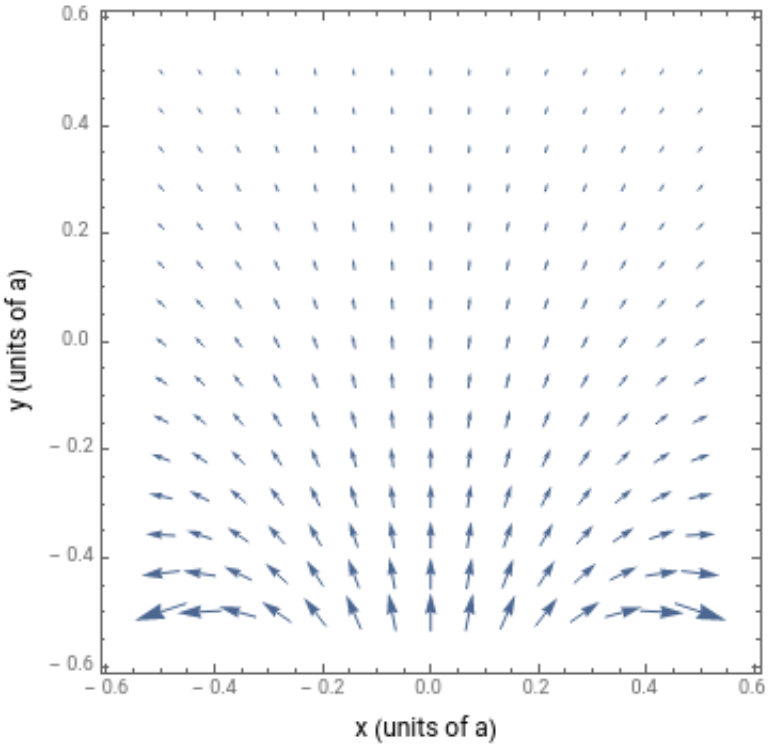

Figure 4.11: The approximate magnetic field due to a single permanent magnet of thickness $t = a$, infinitesimally small width and infinite length positioned from $y = -2a$ to $y = -a$ with magnetization along the y axis.

4.1.2.1 Dipoles

Similar to using two coils with current in the same direction spaced a distance apart to create a region of nearly uniform magnetic field, we can use two permanent magnets with magnetizations pointing in the same direction.

For the dipole field, we have two magnets with magnetization along the thickness (positive y) axis. The first has top located at $y = -a$ and bottom at $y = -a - t$. The second has top located at $y = a + t$ and the bottom at $y = a$.

B_{y0} is very easy to estimate. Exploit the symmetry of the problem and add a term identical to the single magnet case with the transformation $a \to -a$ and $a + t \to -a - t$.

$$B_{y0}(y) \approx \frac{\mu_0 mwt}{2\pi(a+y)(a+t+y)} + \frac{\mu_0 mwt}{2\pi(-a+y)(-a-t+y)} \tag{4.46}$$

Taking a power series in y about the $y = 0$ plane gives

$$B_{y0}(y) \approx \frac{\mu_0 mwt}{\pi}\left(\frac{1}{a(a+t)} + \frac{3a^2+3at+t^2}{(a^3)(a+t)^3}y^2 + \mathcal{O}(y^4)\right). \tag{4.47}$$

Similar to the Helmholtz case, the leading term is of zeroth order, however it is not possible to eliminate the second order term using clever geometries. The magnetic field for this configuration is shown in Figure 4.12.

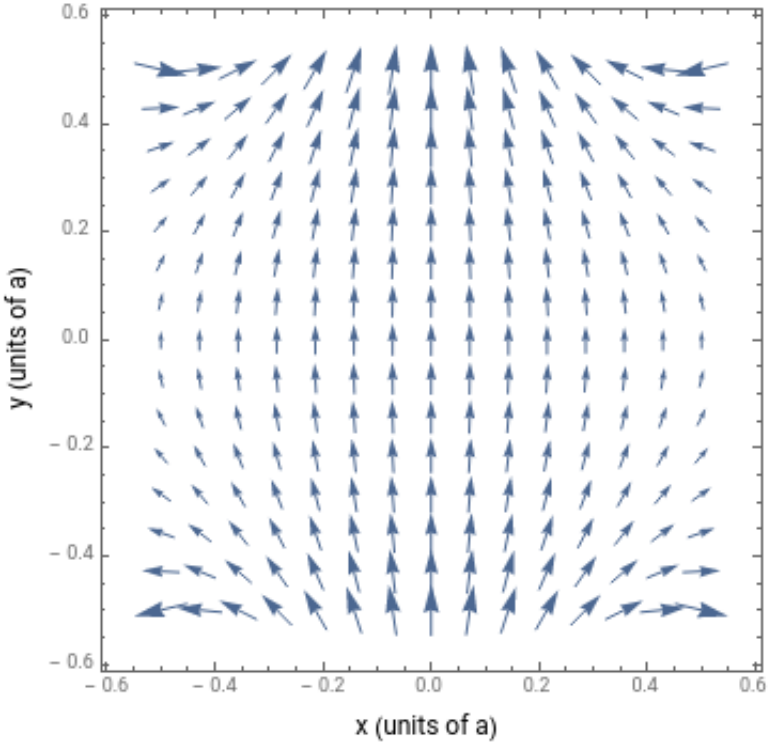

Figure 4.12: The approximate magnetic field due to two permanent magnets of thickness $t = a$, infinitesimally small width and infinite length positioned from $y = -2a$ to $y = -a$ and $y = a$ to $y = 2a$ with upward magnetization.

Note that again, the dipole field is symmetric, has leading term of zeroth order in both x and y and can be formed by a single magnet.

4.1.2.2 Quadrupoles and octupoles

In the previous section, we noticed that a set of coils with current in the same direction created a dipole field while coils with opposing currents created a quadrupole field.

For permanent magnetic fields, dipoles consist of two magnets with magnetization in the same direction while quadrupoles are formed by two magnets with magnetization in opposing directions.

We use the same geometry as the dipole case, but the top magnet will have negative (downward) magnetization. Mathematically, this amounts to flipping the sign corresponding to the field due to the top magnet:

$$B_{y0}(y) \approx \frac{\mu_0 mwt}{2\pi(a+y)(a+t+y)} - \frac{\mu_0 mwt}{2\pi(-a+y)(-a-t+y)}. \tag{4.48}$$

Taking a power series in y about the $y = 0$ plane gives

$$B_{y0}(y) \approx \frac{\mu_0 mwt}{\pi}(-\frac{2a+t}{a^2(a+t)^2}y - \frac{4a^3+6a^2t+4at^2+t^3}{a^4(a+t)^4}y^3 + \mathcal{O}(y^5)) \tag{4.49}$$

This field has leading term of first order in y and has the same antisymmetric form as the magnetic field of anti-Helmholtz coils.

This quadrupole field can be augmented or reduced by adding another set of permanent magnets on the x=0 plane with magnetization along the x axis. First, we consider the case of adding a set of magnets with magnetization pointing away from the origin. Mathematically this is equivalent to making the coordinate transformation $y \to -x$ and $x \to -y$. This magnetic field is plotted in Figure 4.13.

$$B_{x0}(x) \approx \frac{\mu_0 mwt}{2\pi(a-x)(a+t-x)} - \frac{\mu_0 mwt}{2\pi(-a-x)(-a-t-x)} \tag{4.50}$$

Taking a power series in x about the $x = 0$ plane gives

$$B_{x0}(x) \approx \frac{\mu_0 mwt}{\pi}(\frac{2a+t}{a^2(a+t)^2}x + \frac{4a^3+6a^2t+4at^2+t^3}{a^4(a+t)^4}x^3 + \mathcal{O}(x^5)). \tag{4.51}$$

The approximate magnetic field in two dimensions will be

$$\mathbf{B} \approx (B_{x0}(x) - B_{x0}''(x)\frac{y^2}{2})\hat{x} - B_{x0}'(x)y\hat{y}. \tag{4.52}$$

Adding this field to the quadrupole field from magnets along the y axis gives

$$\mathbf{B} \approx (B_{x0}(x) - B_{x0}''(x)\frac{y^2}{2} - B_{y0}'(y)x)\hat{x} + (-B_{x0}'(x)y + B_{y0}(y) - \frac{x^2}{2}B_{y0}''(y))\hat{y}. \tag{4.53}$$

For simplicity, let $B_1 = \frac{\mu_0 mwt}{\pi}\frac{2a+t}{a^2(a+t)^2}$ and $B_3 = \frac{\mu_0 mwt}{\pi}\frac{4a^3+6a^2t+4at^2+t^3}{a^4(a+t)^4}$.

$$\mathbf{B} \approx (B_1 x + B_3 x^3 - 3B_3 x y^2 + B_1 x + 3B_3 x y^2)\hat{x} + (-B_1 y - 3B_3 x^2 y - B_1 y - B_3 y^3 + 3B_3 x^2 y)\hat{y} \tag{4.54}$$

$$\mathbf{B} \approx \frac{2\mu_0 m w t}{\pi} \frac{2a + t}{a^2(a + t)^2}(x\hat{x} - y\hat{y}) + \mathcal{O}(x^n y^{3-n}) \tag{4.55}$$

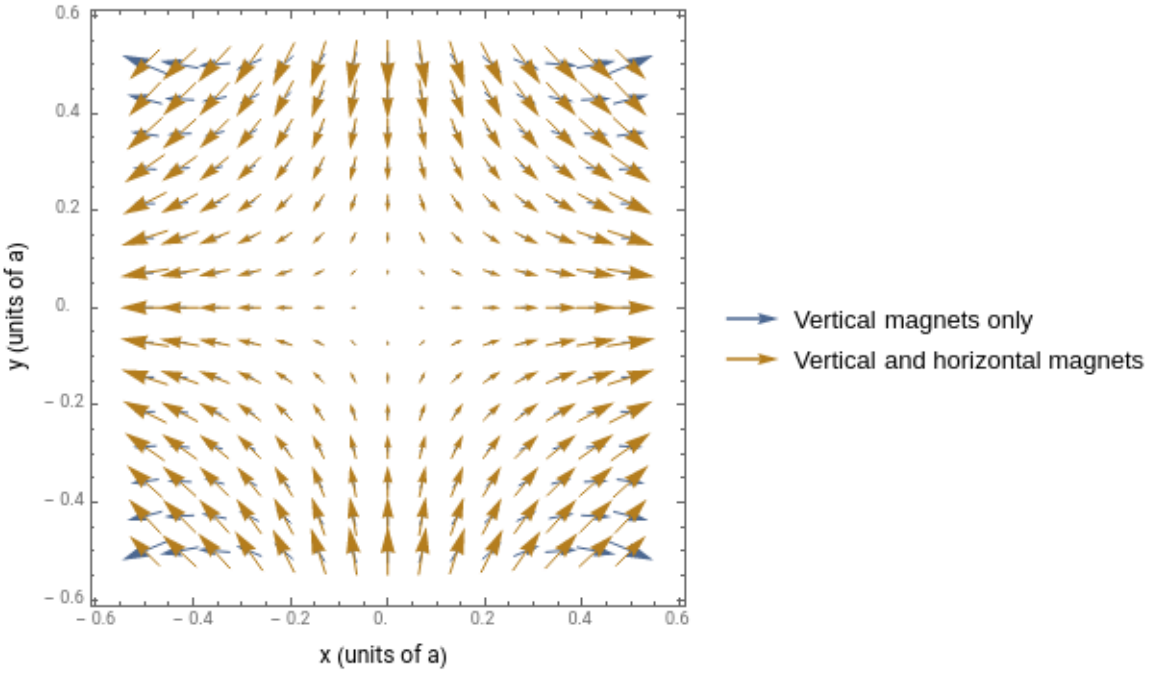

Figure 4.13: The approximate magnetic fields due to one and two sets of two permanent magnets of thickness $t = a$, infinitesimally small width and infinite length. One set positioned along the y axis with one magnet from $y = -2a$ to $y = -a$ and one positioned $y = a$ to $y = 2a$ both with inward magnetization. The second set is positioned along the x axis with one magnet from $x = -2a$ to $x = -a$ and one positioned $x = a$ to $x = 2a$ both with outward magnetization.

Note that similar to the anti-Helmholtz case, the quadrupole field made from permanent magnets is antisymmetic, is of first order in x and y and can be made with as few as two magnets.

When inside this quadrupole field, atoms will feel a force of constant magnitude toward the origin, as shown in Figure 4.14.

$$\mathbf{F} \approx -\mu_B m_j g_j \nabla (B_1 |x\hat{x} - y\hat{y}|^2) \tag{4.56}$$

$$\mathbf{F} \approx -\mu_B m_j g_j \frac{\mu_0 mwt}{\pi} \frac{2a+t}{a^2(a+t)^2} (x\hat{x} + y\hat{y}) \tag{4.57}$$

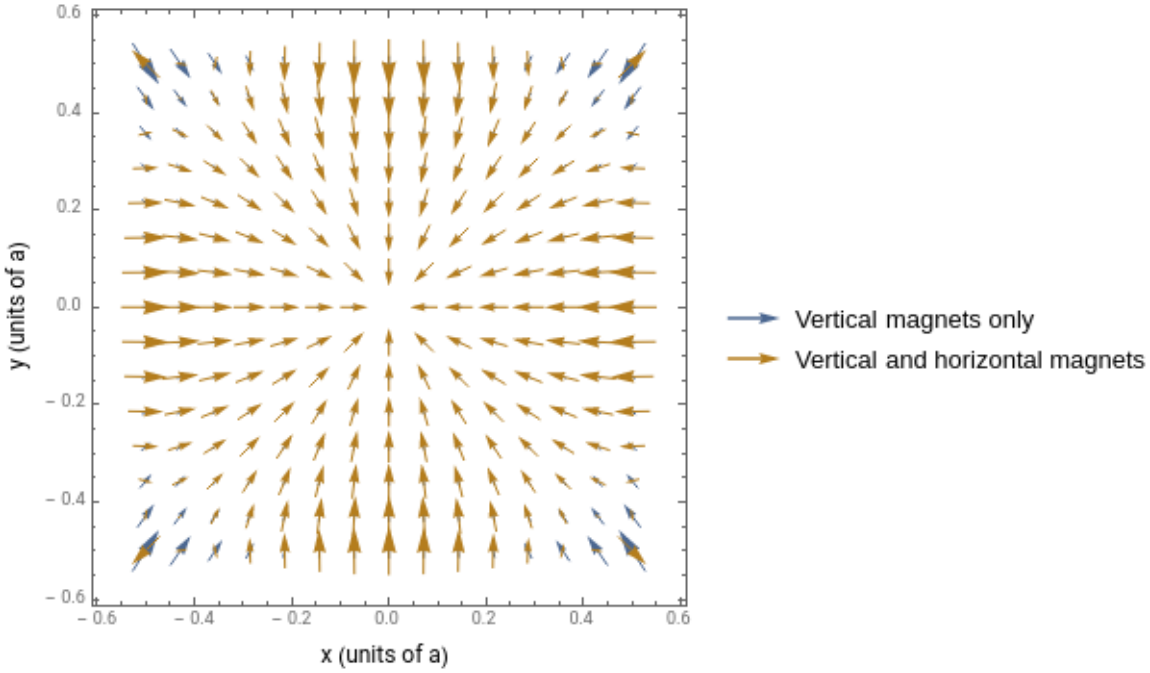

Figure 4.14: The approximate force field on a low field seeking atom inside a permanent magnetic quadrupole field. Near the origin, the force will be constant in magnitude and toward the origin.

The next field configuration we will analyze is with four magnets, all pointing inwards. This is mathematically equivalent to all pointing outwards but with a flipped sign.

Taking the quadrupole field and flipping the sign of the contribution of the horizontal coils gives

$$\mathbf{B} \approx (-B_1 x - B_3 x^3 + 3B_3 x y^2 + B_1 x + 3B_3 x y^2)\hat{x} + (B_1 y + 3B_3 x^2 y - B_1 y - B_3 y^3 + 3B_3 x^2 y)\hat{y}. \tag{4.58}$$

$$\mathbf{B} \approx (-B_3 x^3 + 6B_3 x y^2)\hat{x} + (-B_3 y^3 + 6B_3 x^2 y)\hat{y} + \mathcal{O}(x^n y^{nn-3}) \tag{4.59}$$

Note that there are extra third order terms arising from a second derivative of the fifth order term that I did not take. The point remains however, this octupole field is of third order, can be formed from a minimum of four magnets and, is antisymmetric,.

4.1.2.3 Hexapoles

Now for the fun part: permanent magnetic hexapoles. A permanent magnetic hexapole consists of six magnets arranged in a circle, each separated by 60 degrees from the next and with alternating inward-outward polarization. This is equivalent to having three dipoles, each rotated 120 degrees.

Recall the field of a single permanent magnetic dipole from earlier in the section:

$$B_{y0}(y) \approx \frac{\mu_0 mwt}{\pi}\left(\frac{1}{a(a+t)} + \frac{3a^2+3at+t^2}{(a^3)(a+t)^3}y^2 + \mathcal{O}(y^4)\right). \tag{4.60}$$

By symmetry, the zeroth order terms represent homogenous magnetic fields separated by 120 degrees will end up cancelling. We are therefore only concerned with terms of second order and higher. For simplicity, let $B_0 = \frac{\mu_0 mwt}{\pi}\frac{1}{a(a+t)}$, $B_2 = \frac{\mu_0 mwt}{\pi}\frac{3a^2+3at+t^2}{(a^3)(a+t)^3}$ and $B_4 = \frac{\mu_0 mwt}{\pi}\frac{5a^4+10a^3t+10a^2t^2+5at^3+t^4}{a^5(a+t)^5}$.

In this simpler notation, the nontrivial addition of each magnet to the total field will be

$$\mathbf{B^*} \approx (B_2 y^{*2} + B_4 y^{*4} - 2B_2 x^{*2} - 12B_4 x^{*2} y^{*2})\hat{y}^* + (-2B_2 y^* x^* - 4B_4 x^* y^{*3})\hat{x}^*. \tag{4.61}$$

The first magnet pair will be rotated zero degrees, $x^* \to x, y^* \to y$. The second pair will be rotated 120 degrees. $x^* \to -\frac{x}{2} + \frac{\sqrt{3}y}{2}, y^* \to -\frac{\sqrt{3}x}{2} - \frac{y}{2}$. The third pair will be rotated 240 degrees. $x^* \to -\frac{x}{2} - \frac{\sqrt{3}y}{2}, y^* \to +\frac{\sqrt{3}x}{2} - \frac{y}{2}$.

This ends up being a truly horrendous sum, but it looks much nicer in cylindrical coordinates. We plot the magnetic field of this configuration in Figure 4.15 and the force field on low field seeking atoms in Figure 4.16.

$$\mathbf{B} \approx \frac{\mu_0 mwt}{\pi}\frac{3(3a^2+3at+t^2)\rho^2(\sin(2\phi)\hat{x} - \cos(2\phi)\hat{y})}{a^3(a+t)^3} + \mathcal{O}(\rho^4) \tag{4.62}$$

, where $\rho = \sqrt{x^2+y^2}$ and $\phi = \arctan y/x$.

This ρ^2 dependence is a very important result as it requires that $F \propto -\rho$, the ideal harmonic field for focusing. We will use this exact configuration as a focusing element to focus a diverging beam of atoms exiting the supersonic nozzle.

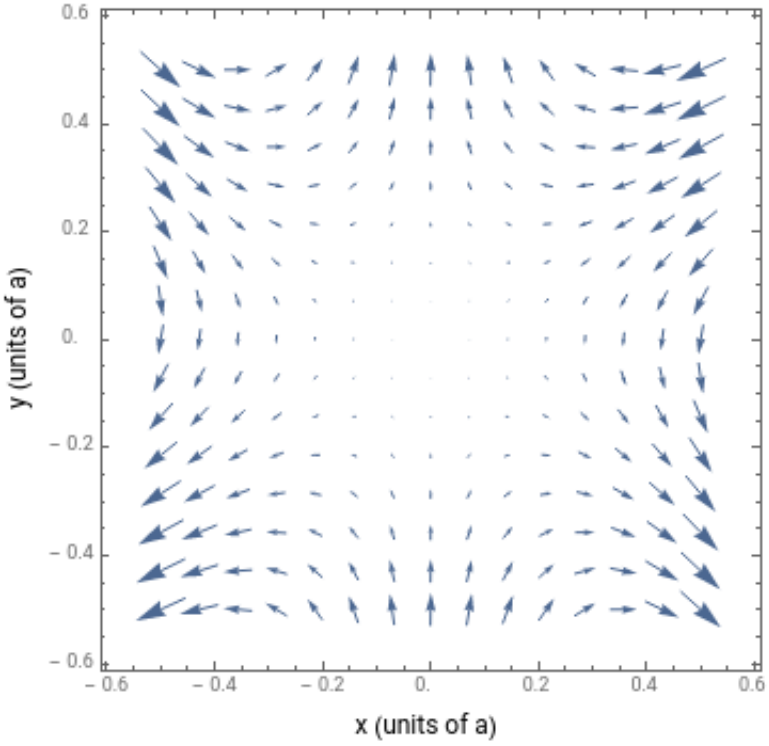

Figure 4.15: The approximate magnetic fields due to six permanent magnets of thickness $t = a$, infinitesimally small width and infinite length. The magnets are separated by 60 degrees and have alternating polarization. The edge of the magnet closest to the center is a distance $a = t$ from the center and the further edge is a distance $a = 2t$ from the center.

$$\mathbf{F} \approx -\mu_B m_j g_j \frac{\mu_0 mwt}{\pi} \frac{3(3a^2 + 3at + t^2)}{a^3(a+t)^3} \nabla|\rho^2| \tag{4.63}$$

$$\mathbf{F} \approx -2\mu_B m_j g_j \frac{\mu_0 mwt}{\pi} \frac{3(3a^2 + 3at + t^2)}{a^3(a+t)^3} \rho\hat{\rho} \tag{4.64}$$

For completeness, note that the hexapole field is symmetric about the x axis and could be created with any multiple of three magnets.

4.1.3 Current-carrying straight conductors

The final configurations of magnetic multipoles I will discuss are magnetic fields due to infinite current-carrying straight conductors. In reality and in this experiment, all

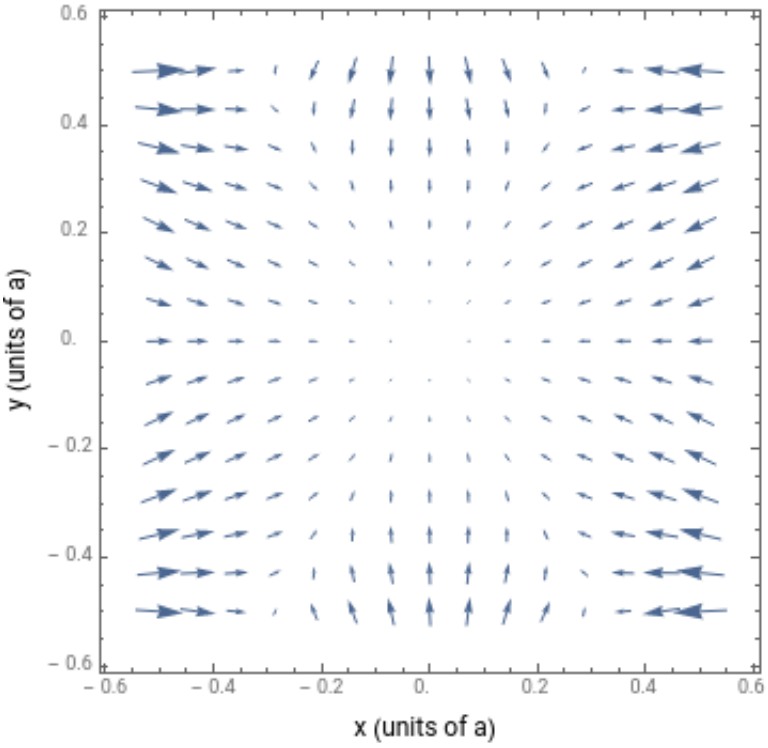

Figure 4.16: The approximate force field on a low field seeking atom inside a permanent magnetic hexapole field. Near the origin, the force will increase with the distance from the origin and point toward the origin.

conductors are finite, but assuming the distance from the point being measured to the conductor is much shorter than the length of the conductor, assuming the conductors are infinite is a reasonable approximation.

In cylindrical coordinates, the magnetic field due to a current I travelling in the positive z direction in a single infinitely long wire passing through the origin is

$$\mathbf{B} = \frac{\mu_0 I}{2\pi(\boldsymbol{\rho} - \boldsymbol{\rho'})^2}\hat{z} \times (\boldsymbol{\rho} - \boldsymbol{\rho'}), \tag{4.65}$$

where ρ is the point at which the field is being measured and ρ' is the point at which the current is flowing. Note this field is exact over all space outside the conductor and we will not have to employ Maxwell's equations to solve for an off axis field.

4.1.3.1 Dipoles

Consider the case of two parallel wires separated by a distance 2a with current I travelling in opposite directions perpendicular to the x-y plane. Let the wire with current flowing in the positive z direction be located at $x = a, y = 0$ and the wire with current flowing in the negative z direction be located at $x = -a, y = 0$, the magnetic field of which is plotted in Figure 4.17.

The total magnetic field due to current flowing through the two rods will be

$$\mathbf{B} = \frac{\mu_0 I}{2\pi((x-a)^2+y^2)}\hat{z}\times((x-a)\hat{x}+y\hat{y}) - \frac{\mu_0 I}{2\pi((x+a)^2+y^2)}\hat{z}\times((x+a)\hat{x}+y\hat{y}). \quad (4.66)$$

$$\mathbf{B} = \frac{\mu_0 I}{2\pi}\left(\frac{(x-a)\hat{y}-y\hat{x}}{((x-a)^2+y^2)} - \frac{(x+a)\hat{y}-y\hat{x}}{((x+a)^2+y^2)}\right) \quad (4.67)$$

Taking a Taylor Series near the origin and keeping terms of order up to $x^n y^{2-n}$ gives

$$\mathbf{B} = \frac{\mu_0 I}{a\pi}\left(-\frac{2xy}{a^2}\hat{x} + (-1+\frac{y^2}{a^2})\hat{y}\right) + \mathcal{O}(x^n y^{4-n}). \quad (4.68)$$

Just like with Helmholtz coils and permanent magnetic dipoles, this field is of zeroth order in both x and y and is symmetric about both the x and y axes.

4.1.3.2 Quadrupoles and octupoles

The next configuration will consist of four infinitely long straight wires located at $(x, y) = (a, 0), (0, a), (-a, 0), (0, -a)$. The first and third will have current I flowing in the positive z direction while the second and fourth have current I flowing in the negative z direction. The magnetic field of this configuration is plotted in Figure 4.18.

$$\mathbf{B} = \frac{\mu_0 I}{2\pi}\left(\frac{(x-a)\hat{y}-y\hat{x}}{((x-a)^2+y^2)} + \frac{(x+a)\hat{y}-y\hat{x}}{((x+a)^2+y^2)} - \frac{(y-a)\hat{x}-x\hat{y}}{((y-a)^2+x^2)} - \frac{(y+a)\hat{x}-x\hat{y}}{((y+a)^2+x^2)}\right) \quad (4.69)$$

Taking a Taylor Series near the origin and keeping terms of order up to $x^n y^{3-n}$ gives

$$\mathbf{B} = \frac{\mu_0 I}{a^2\pi}(-2y\hat{x} - 2x\hat{y}) + \mathcal{O}(x^n y^{5-n}). \quad (4.70)$$

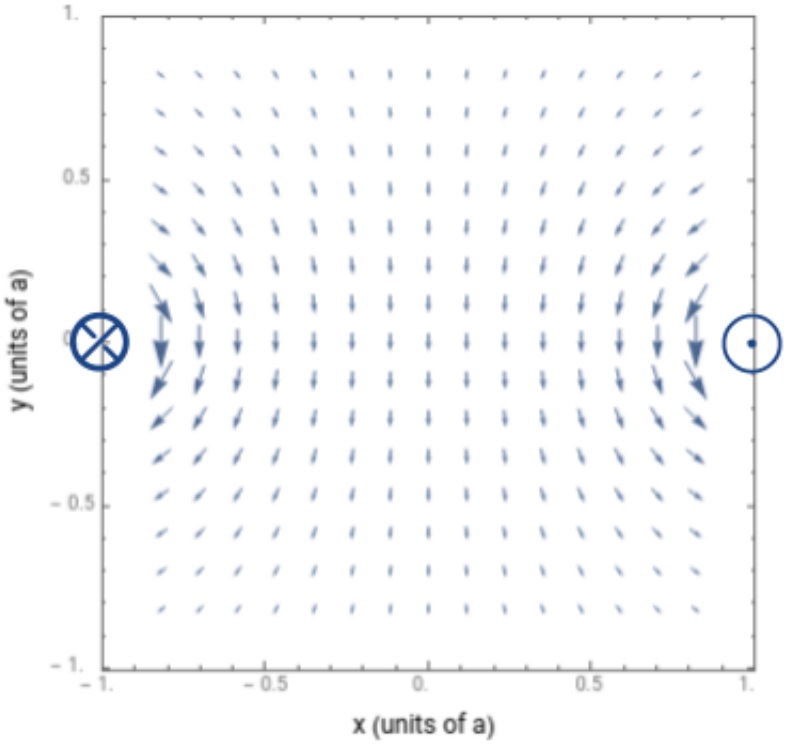

Figure 4.17: The magnetic field due to two infinitely long straight conductors, one with current in the positive z direction at location $(x, y) = (a, 0)$ and one with current in the negative z direction at location $(x, y) = (-a, 0)$

All third order terms drop out and we are left with just the first order term alongside terms of fifth order and higher. This field is of first order in both x and y and is antisymmetric about both axes. Assuming no net current, four conductors are required to create this field.

We next calculate the force on an atom near the center of the quadrupole field and plot the force field on low field seeking atoms in Figure 4.19.

$$\mathbf{F} = -\mu_B m_j g_j \nabla |\frac{\mu_0 I}{a^2 \pi}(-2y\hat{x} - 2x\hat{y} + \mathcal{O}(x^n y^{5-n}))|^2 \tag{4.71}$$

$$\mathbf{F} = -\mu_B m_j g_j |\frac{2\mu_0 I}{a^2 \pi}(\hat{x} + \hat{y} + \mathcal{O}(x^n y^{4-n})) \tag{4.72}$$

Note the near the origin, the force is of near constant magnitude and always toward the center of the quadrupole field.

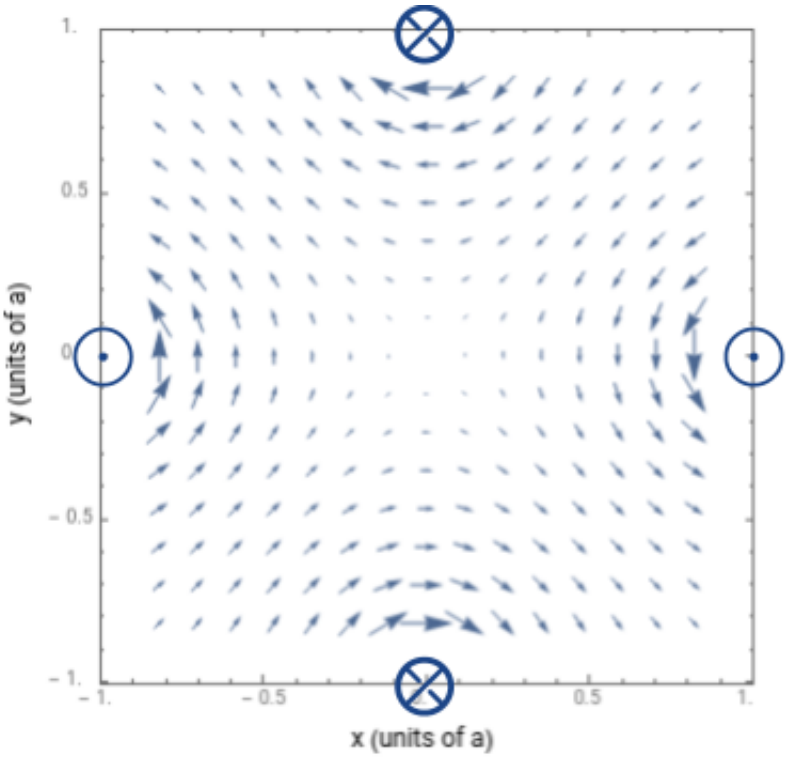

Figure 4.18: The magnetic field due to four infinitely long straight conductors, located at positions $(x, y) = (a, 0), (0, a), (-a, 0), (0, -a)$. The first and third have current in the positive z direction. The second and fourth have current in the negative z direction.

For the octupole field we use eight conductors each a distance a from the center and each separated by 45 degrees. Each conductor carries a current of magnitude I, but in alternating directions. We plot the resulting magnetic field in Figure 4.20.

$$\mathbf{B} = \frac{\mu_0 I}{2\pi} \sum_{i=0}^{7} \frac{(x - x_i)\hat{y} - (y - y_i)\hat{x}}{((x - x_i)^2 + (y - y_i)^2)} (-1)^i, \tag{4.73}$$

where $x_i = a \cos \frac{2i\pi}{8}$ and $y_i = a \sin \frac{2i\pi}{8}$.

Taking a Taylor series of this sum near the origin, dropping terms of seventh order or higher gives

$$\mathbf{B} = \frac{\mu_0 I}{2\pi a^4}((-8y^3 + 24x^2 y)\hat{x} + (8x^3 - 24xy^2)\hat{y}) + \mathcal{O}x^n y^{7-n}. \tag{4.74}$$

As clean as this is, it is cleaner is cylindrical coordinates:

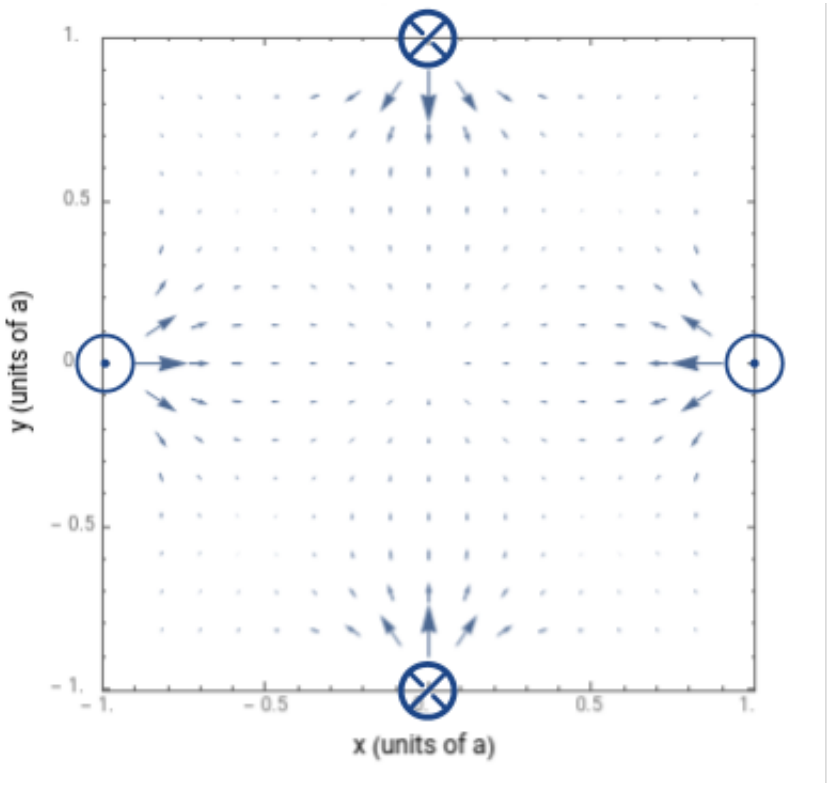

Figure 4.19: The force on a low field seeking atom four infinitely long straight wires located at $(x, y) = (a, 0), (0, a), (-a, 0), (0, -a)$. The first and third will have current I flowing in the positive z direction while the second and fourth have current I flowing in the negative z direction.

$$\mathbf{B} = \frac{8\rho^3\mu_0 I}{2\pi a^4}((-\sin^3(\phi) + 3\cos^2(\phi)\sin(\phi))\hat{x} + (\cos^3(\phi) - 3\cos(\phi)\sin^2(\phi))\hat{y} + \mathcal{O}x^n y^{7-n}, \tag{4.75}$$

$$\mathbf{B} = \frac{8\rho^3\mu_0 I}{2^4}(-\sin(3\phi)\hat{x} - \cos(3\phi)\hat{y}) + \mathcal{O}(x^n y^{7-n}). \tag{4.76}$$

Note the field strength is of third order in ρ and is antisymmetric.

The force on a low field seeking atom is very easy to approximate:

$$\mathbf{F} \approx -\mu_B m_j g_j \frac{24\rho^2\mu_0 I}{2\pi a^4}\hat{\rho}. \tag{4.77}$$

Note the force on low field seeking atoms will be toward the origin and scales with ρ^2.

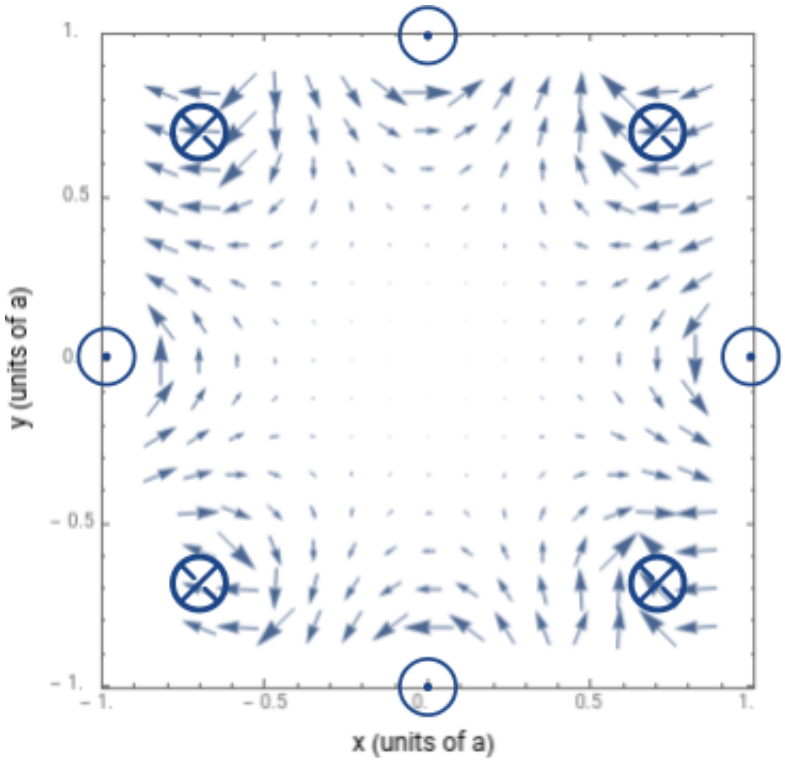

Figure 4.20: The magnetic field due to eight infinitely long straight conductors, each a distance a from the origin, separated by 45 degrees with currents in alternating positive and negative z directions.

4.1.4 Hexapoles

We use the same formula to calculate the field due to six wires with current in alternating directions as we used for eight wires. We plot the resulting magnetic field in Figure 4.21 and the resulting force field on low field seeking atoms in Figure 4.22.

$$\mathbf{B} = \frac{\mu_0 I}{2\pi} \sum_{i=0}^{5} \frac{(x - x_i)\hat{y} - (y - y_i)\hat{x}}{((x - x_i)^2 + (y - y_i)^2)} (-1)^i, \tag{4.78}$$

where $x_i = a \cos \frac{2i\pi}{6}$ and $y_i = a \sin \frac{2i\pi}{6}$.

Taking a Taylor series of this sum near the origin, dropping terms of eighth order or higher gives

$$\mathbf{B} = \frac{\mu_0 I}{2\pi a^3} (12xy\hat{x} + (6x^2 - 6y^2)\hat{y}) + \mathcal{O}x^n y^{7-n} \tag{4.79}$$

This equation is also simpler in cylindrical coordinates:

$$\mathbf{B} = \frac{6\mu_0 I\rho^2}{2\pi a^3}(-\sin 2\phi\hat{x} - \cos 2\phi\hat{y}) + \mathcal{O}x^n y^{7-n}. \tag{4.80}$$

This field strength is of second order in ρ and is three fold symmetric.

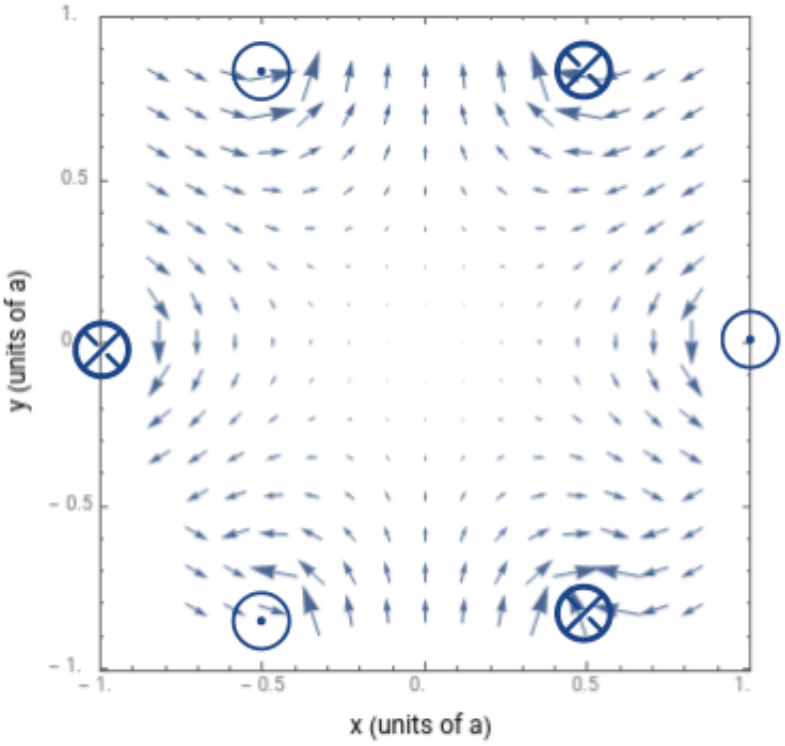

Figure 4.21: The magnetic field due to six infinitely long straight conductors, each a distance a from the origin, separated by 60 degrees with currents in alternating positive and negative z directions.

Due to the radial symmetry of the magnitude of the magnetic field, the force is again trivial to calculate:

$$\mathbf{F} \approx -\mu_B m_j g_j \frac{12\rho\mu_0 I}{2\pi a^3}\hat{\rho}. \tag{4.81}$$

The radial dependence of this force renders the magnetic hexapole field ideal for focusing.

We have calculated the magnetic fields due to two, four, six, and eight parallel rods a distance a from the origin, each rod having a current in an opposite direction

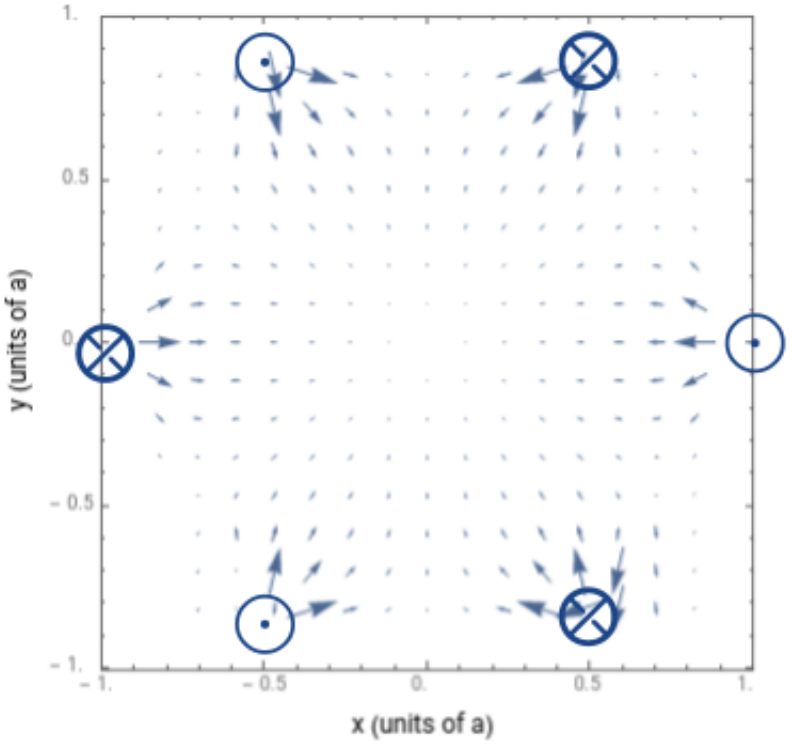

Figure 4.22: The force on low field seeking atoms due to six infinitely long straight conductors, each a distance a from the origin, separated by 60 degrees with currents in alternating positive and negative z directions.

as its neighbors and we notice a pattern for calculating the approximate field near the origin. For a pole of order n (for dipoles, n=2, quadrupoles, n=4 etc.), to lowest order, the magnetic field is given by

$$\mathbf{B} \approx \frac{\mu_0 I n}{2\pi a^{n/2}} \rho^{n/2-1}(-\sin((\frac{n}{2}-1)\phi)\hat{x} - \cos((\frac{n}{2}-1))\hat{y}). \tag{4.82}$$

Similarly, the force also has a general equation for any n-pole:

$$\mathbf{F} \approx -\mu_B m_j g_j \frac{\mu_0 I n(\frac{n}{2}-1)}{2\pi a^{n/2}} \rho^{n/2-2}\hat{\rho}. \tag{4.83}$$

4.2 Chapter summary

To this point, we have analyzed dipole, quadrupole, octupole and hexapole fields due to circular coils, permanent magnets and pseudo infinite current carrying rods and

have noticed some interesting symmetries and analogs, regardless of the mechanism for creating the magnetic fields.

Dipole fields are of zeroth order in position and are approximately constant over a large region and thus to first order, do not provide a net force on neutral atoms. They have at least one axis of symmetry and can generally be created from a single magnetic element (though two is often preferable). Dipole fields are useful for creating a uniform bias field across a region of space.

Quadrupole fields are of first order in position and have approximately constant field gradient and will provide a force of constant magnitude on magnetic atoms over a large region of space. They are antisymmetric and can generally be made from two dipole elements in opposing directions. Quadrupole fields are useful for giving atoms a uniform magnetic kick in a direction towards a specific point.

Hexapole fields are of second order in position and have a field gradient that increases linearly with distance along a chosen axis. Hexapole fields have at least one axis of symmetry and can generally be made from any multiple of three magnetic dipole elements. Hexapole fields are useful for providing a focusing force on a cloud of atoms of finite spatial extent.

Octupole fields are of third order in position and have a field gradient that increases with the square of position. Octupole fields are antisymmetric and can generally be formed from two opposing quadrupole fields, requiring a minimum of four magnetic elements. Octupole fields are useful for providing further background education to the reader but are of no actual use to this experiment.

4.3 Magnetic monopoles

Section not found.

Chapter Five: Permanent magnetic hexapole

While the previous chapter did an excellent job providing the theoretical framework for permanent magnetic hexapoles, this chapter will discuss the physical framework for the permanent magnetic hexapole that exists as part of our experiment.

In our experimental setup, upon exiting the nozzle and skimmer, the atomic beam is cooled longitudinally and optically pumped to the low field seeking $m_j = 2$ magnetic state. After optical pumping, the atomic beam passes through the magnetic hexapole lens. The lens focuses the beam to a spot downstream, at which point it will be laser cooled and collimated in the transverse direction.

5.1 Lens construction

We derived the equation for the magnetic field of a permanent magnetic field consisting of six infinitely long permanent magnets with thickness t, width w, inner radius a, and magnetization m, spaced sixty degrees apart with alternating inward-outward magnetization:

$$\mathbf{B} \approx \frac{\mu_0 mwt}{\pi} \frac{3(3a^2 + 3at + t^2)}{a^3(a+t)^3} \rho^2 (\sin(2\phi)\hat{x} - \cos(2\phi)\hat{y}) + \mathcal{O}(\rho^4). \tag{5.1}$$

The magnets we use are Neodymium N52 NdFeB block magnets from K&J Magnetics with dimensions 3/4 in. x 1/16 in. x 1/4 in. and magnetization along the 1/4 in. thickness axis. The remanence of these magnets is quoted as 1.45-1.48 T[59].

We designed a cylindrical delrin block with 1.375 in. outer diameter and circular cross section and 3 in. length as shown in Figures 5.1 and 5.2 to serve as a mount for the permanent magnetic lens. The mount has a central circular bore through which the atomic beam passes. The bore was drilled to fit snugly over a titanium tube of outer diameter .25 in. and inner diameter .18 in. which serves as the vacuum chamber for this section of the beamline. The titanium tube is connected to the remainder of the vacuum chamber using quick connect fittings from Kurt J. Lesker Company[58]. Twelve identical trenches of width .064 in. and depth .5 in. spaced 30 degree apart

are carved out of the delrin to house the magnets themselves. Six of these trenches are not used. Each trench can fit an array of magnets two deep and four wide.

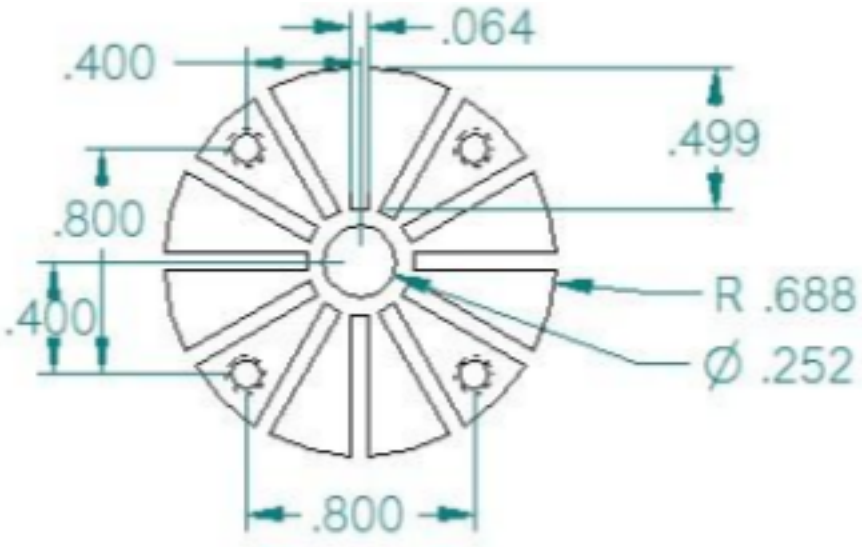

Figure 5.1: A CAD drawing of the cross section of the cylindrical delrin lens mount. The magnets sit in the trenches of the mount. The atoms pass through a titanium tube inside the central bore of the lens.

Physically, this corresponds to $\mu_0 m \approx 1.45\,\mathrm{T}$, $w = .0625'' = 1.8755\,\mathrm{mm}$, $a = .1875'' = 4.7625\,\mathrm{mm}$, $t = 6.35\,\mathrm{mm}$ for single magnets or $t = 12.7\,\mathrm{mm}$ for stacks of two magnets.

Plugging in numbers for magnetic field for an array one magnet deep gives

$$\mathbf{B} \approx 18\,747\,\mathrm{T\,m^{-2}}\rho^2(\sin(2\phi)\hat{x} - \cos(2\phi)\hat{y}). \tag{5.2}$$

For a stack two magnets deep, we would get

$$\mathbf{B} \approx 19\,936\,\mathrm{T\,m^{-2}}\rho^2(\sin(2\phi)\hat{x} - \cos(2\phi)\hat{y}). \tag{5.3}$$

In the limit of an infinite stack of magnets ie. $t \to \infty$

$$\mathbf{B} \approx 20\,349\,\mathrm{T\,m^{-2}}\rho^2(\sin(2\phi)\hat{x} - \cos(2\phi)\hat{y}). \tag{5.4}$$

It is clear that adding more magnets beyond a second stack does not drastically change the strength of the hexapole field.

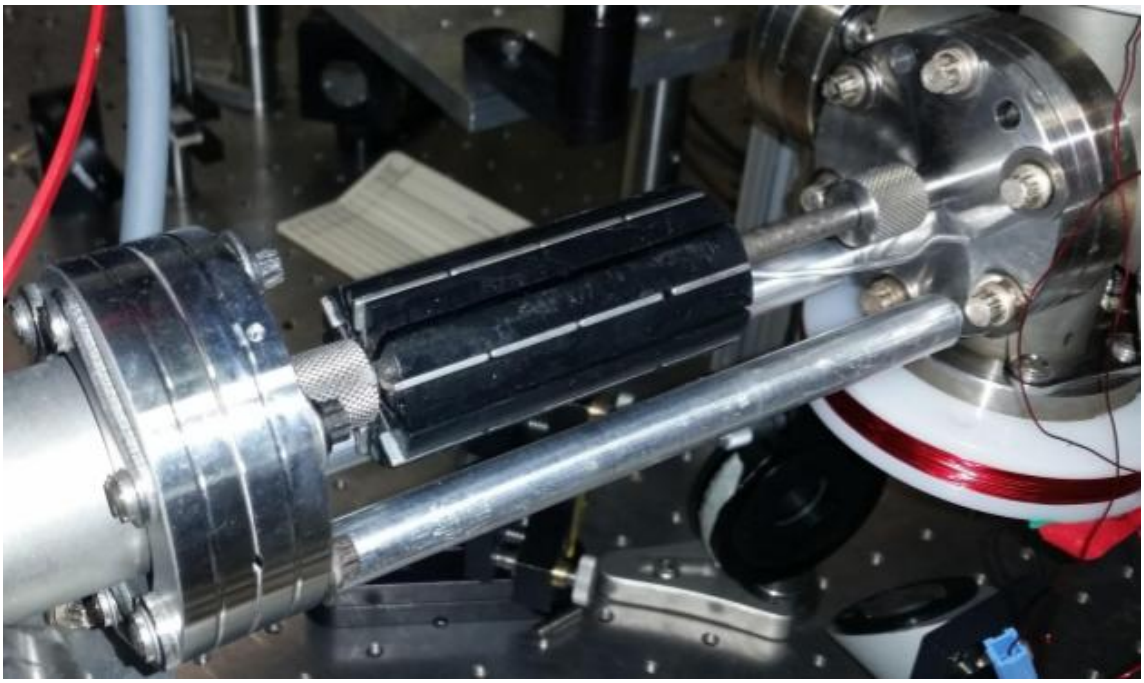

Figure 5.2: The permanent magnetic hexapole. Six arrays of N52 permanent magnets stacked two deep and four long rest in trenches cut out of a cylindrical delrin block. Inside the block is a hollow titanium tube through which the atomic beam passes. As shown, the atomic beam passes right to left through the permanent magnetic hexapole lens.

An interesting check is to calculate the magnitude of this approximate field as $\rho \to a$. For a single magnet

$$\mathbf{B}|_{\rho\to a} \approx 0.425\,\mathrm{T}. \tag{5.5}$$

For a stack of two magnets, we would get

$$\mathbf{B}|_{\rho\to a} \approx 0.452\,\mathrm{T}, \tag{5.6}$$

while for an infinite stack of magnets,

$$\mathbf{B}|_{\rho\to a} \approx 0.462\,\mathrm{T}. \tag{5.7}$$

For an infinite stack of magnets, the ratio between the approximate magnetic field and the remanance of the actual magnets is roughly .31831. If this ratio looks interesting to you, it should. If it doesn't, it's $\frac{1}{\pi}$. Recall that the width of magnets

used is 1/16" or 1/3 the inner radius a of the hexapole. If the total width of the six magnets were to equal the circumference of the hexapole with radius a, the ratio of width to inner radius would be $\frac{\pi}{3}$. Because our magnets are a factor of π smaller, our approximate field at $\rho = a$ is smaller than the remanance field by a factor of π. Keep in mind, that our approximation methods are based on the assumption that the width of the magnets is sufficiently small than an integral can be approximated with an average value multiplied by a width. Still, this serves as a nice sanity check for the validity of our approximate magnetic hexapole field strength.

For the remainder of this chapter, we will analyze only the two magnet stack case.

It is worth analyzing how the strength of the magnet scales with inner diameter, which is relevant because a hexapole with a larger inner diameter will enable a lens with a wider aperture:

$$|B| \propto wt\frac{a^2}{a^6}\rho^2 \propto \frac{\rho^2}{a^2} \tag{5.8}$$

An interesting thing to note is that the field strength varies with $\frac{\rho^2}{a^2}$ whereas a hexapole built from straight conductors has a field strength that varies with $\frac{\rho^2}{a^3}$. The permanent hexapole will retain its strength for increasing inner radius better than a hexapole made from straight current carrying conductors. This renders it the more effective lens for wide aperture applications.

Next we look at the force on low field seeking atoms within the bore of the hexapole. We derived the force to be

$$\mathbf{F} \approx -\mu_B m_j g_j \frac{\mu_0 mwt}{\pi} \frac{3(3a^2+3at+t^2)}{a^3(a+t)^3} \nabla|\rho^2|. \tag{5.9}$$

$$\mathbf{F} \approx -2\mu_B m_j g_j \frac{\mu_0 mwt}{\pi} \frac{3(3a^2+3at+t^2)}{a^3(a+t)^3} \rho\hat{\rho} \tag{5.10}$$

Plugging in numbers gives

$$\mathbf{F} \approx -1.11 \times 10^{-18} \mathrm{N\,m^{-1}} \rho\hat{\rho}. \tag{5.11}$$

I will refer to this constant of proportionality as F_0:

$$F_0 \equiv 2\mu_B m_j g_j \frac{\mu_0 mwt}{\pi} \frac{3(3a^2+3at+t^2)}{a^3(a+t)^3} \approx 1.11 \times 10^{-18}\,\mathrm{N\,m^{-1}}. \tag{5.12}$$

One major assumption we have made throughout this exercise is that the magnetic field is due to infinitely long magnets. Obviously this is not the case. The magnets we use are 3/4 in. long but can be placed side by side such that the total length of the magnet is any integer multiple of 3/4 in. We make the incorrect assumption that the magnetic field inside the bore of the magnets is as derived and immediately outside the edges, the magnetic field is zero. While this is physically impossible, it serves as a reasonable mathematical starting point.

The total impulse on a low field seeking atom traveling through the bore of the hexapole will therefore be

$$\Delta p_\rho \approx -F_0 \tau \rho \hat{\rho}, \tag{5.13}$$

where τ is the travel time through the bore of the hexapole.

5.2 Focal length approximation

We next assign a focal length to this now finite length. From geometric optics, we know that a perfectly collimated beam passing through an ideal lens will focus to a single spot a distance downstream from the lens regardless of its initial transverse position. For a single atom with velocity parallel to the lens axis, it will cross the lens axis at this focal point as shown in Figure 5.3. Using ray tracing methods on a particle moving parallel to the axis of a thin lens a distance ρ from its axis will be focused to a point downstream determined by the impulse it feels and its longitudinal velocity. The ratio of this distance, the focal length to the axial distance ρ is equal to the ratio of longitudinal velocity to the perpendicular velocity kick it feels from the lens impulse.

Using a thin lens approximation,

$$\frac{\rho}{f} = \frac{\Delta v_\rho}{v_z} = \frac{\Delta p_\rho / m}{v_z}. \tag{5.14}$$

Plugging in numbers for the power $\frac{1}{f}$ gives

$$\frac{1}{f} \approx 2.53\,\mathrm{m}^{-1}\, magnets^{-1}. \tag{5.15}$$

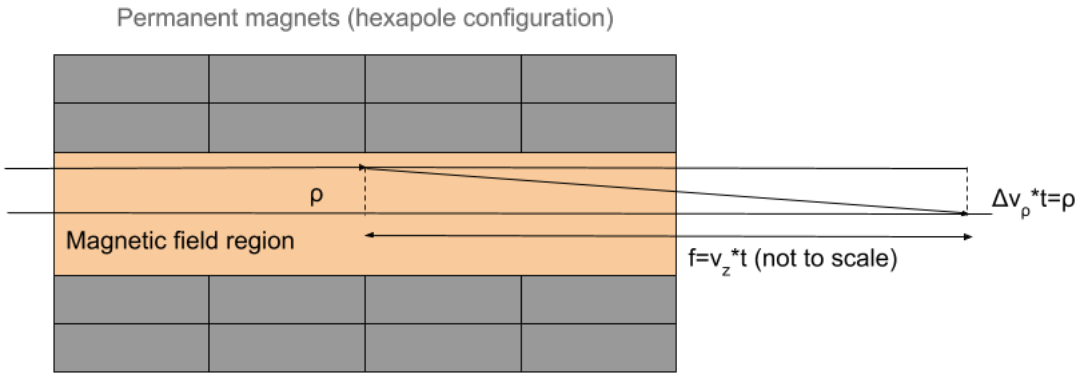

Figure 5.3: A diagram of an atom passing through a permanent hexapole field. The atom will cross the lens axis at a point downstream from the lens. This distance is proportional to the ratio of the longitudinal velocity of the atom to the impulse an atom feels. This ratio will be constant for all values of initial axial position ρ

For a 3/4" long hexapole, this corresponds to a focal length of approximately 40 cm. For arrays two, three and four magnets long, this corresponds to focal lengths of 20 cm, 13 cm, and 10 cm long respectively.

Throughout this analysis, we have made several nonphysical approximations that affect the validity of these calculations, nonetheless we have reached a starting point for what to expect from the permanent magnetic lens. As this serves as a sort of collector lens, its purpose is funnel as many atoms into as dense of a spot as possible. At this point, we value the effectiveness of the lens for wide apertures more than its precision. Analysis of its performance will be analyzed in Chapter 8.

5.3 Atomic funnel

At the focus of the permanent magnetic hexapole, we employ transverse cooling to collimate the atomic beam at its narrowest point. As shown in Figure 5.4, the overall shape of this focused and collimated beam somewhat resembles the shape of a funnel with a wide opening converging to a narrow neck at which point it is collimated.

Recall from Chapter 3 the force on an atom due to laser cooling,

$$F \approx -\frac{8\frac{I}{I_{\text{sat}}} \times \frac{\delta_0}{\gamma}\hbar k^2}{(1+\frac{I}{I_{\text{sat}}}+(2\delta_0/\gamma)^2)^2} v = -\beta v, \tag{5.16}$$

where

$$\beta = \frac{8\frac{I}{I_{\text{sat}}} \times \frac{\delta_0}{\gamma}\hbar k^2}{(1 + \frac{I}{I_{\text{sat}}} + (2\delta_0/\gamma)^2)^2}. \tag{5.17}$$

This approximation holds roughly over the region $|\frac{kv}{2\pi}| < |\delta_0|$. Laser cooling will be unable to collimate atoms with transverse velocity outside this region.

For $\delta_0 = \gamma \approx 8.18\,\text{MHz}$, this gives a maximum transverse velocity of approximately $5.1\,\text{m}\,\text{s}^{-1}$. Any atoms with greater transverse velocity will not be collimated.

The transverse velocity spread of our beam can be calculated geometrically. This also sets the minimum usable focal length:

$$v_{||}\frac{a}{f} < 5.1\,\text{m}\,\text{s}^{-1}. \tag{5.18}$$

For longitudinal velocity $v_{||} = 500\,\text{m}\,\text{s}^{-1}$ and inner radius of the hexapole lens tube $a = 2.25\,\text{mm}$,

$$f > 22\,\text{cm}. \tag{5.19}$$

If the focal length is shorter than roughly 22 cm, atoms with the greatest divergence angle at the focus cannot be collimated through laser cooling. These atoms will thus be removed from the beam.

Another factor to be considered is the time it takes laser cooling to collimate the focused beam and the associated laser width along the direction parallel to the propagation of the beam.

Given the transverse force on atom $F \approx -\beta v$, the transverse velocity of the atom as a function of time will be

$$v = v_0 e^{-\frac{\beta}{m}t}. \tag{5.20}$$

The final velocity achievable is the Doppler velocity. Continuing to attempt to cool once the velocity has decreased below the Doppler limit will not further cool the beam:

$$v_{\text{Doppler}} = v_0 e^{-\frac{\beta}{m}t_{\text{final}}}. \tag{5.21}$$

$$t_{\text{final}} = -\frac{m_{Ne}}{\beta}\ln\frac{v_{\text{Doppler}}}{v_0} \tag{5.22}$$

For a detuning $\delta_0 = \gamma$ and intensity $I = I_0$,

$$t_{\text{final}} = -\frac{m_{Ne}}{4/9 \times \hbar k^2} \ln \frac{v_{\text{Doppler}}}{v_0} \approx 42\,\mu\text{s}. \tag{5.23}$$

In physical space, this corresponds to a distance $z = v_{||} t_{\text{final}} \approx 21\,\text{mm}$ along the longitudinal direction of the beam, meaning our transverse cooling laser must be at least this wide in the longitudinal direction. In the direction transverse to both the the laser and the atomic beam, the beam need not be wider than a few millimeters. A beam of this aspect ratio can be made by means of a telescope with cylindrical lens. We use a telescope with 50 mm and 350 mm lenses to expand a circular beam with 5 mm diamter to create an elliptical beam with a 25 mm major diameter and 5 mm minor diameter.

We now have limits on both the minimum focusing distance between the magnetic lens and the cooling lasers as well as the minimum width of cooling laser to cool the beam to the Doppler limit.

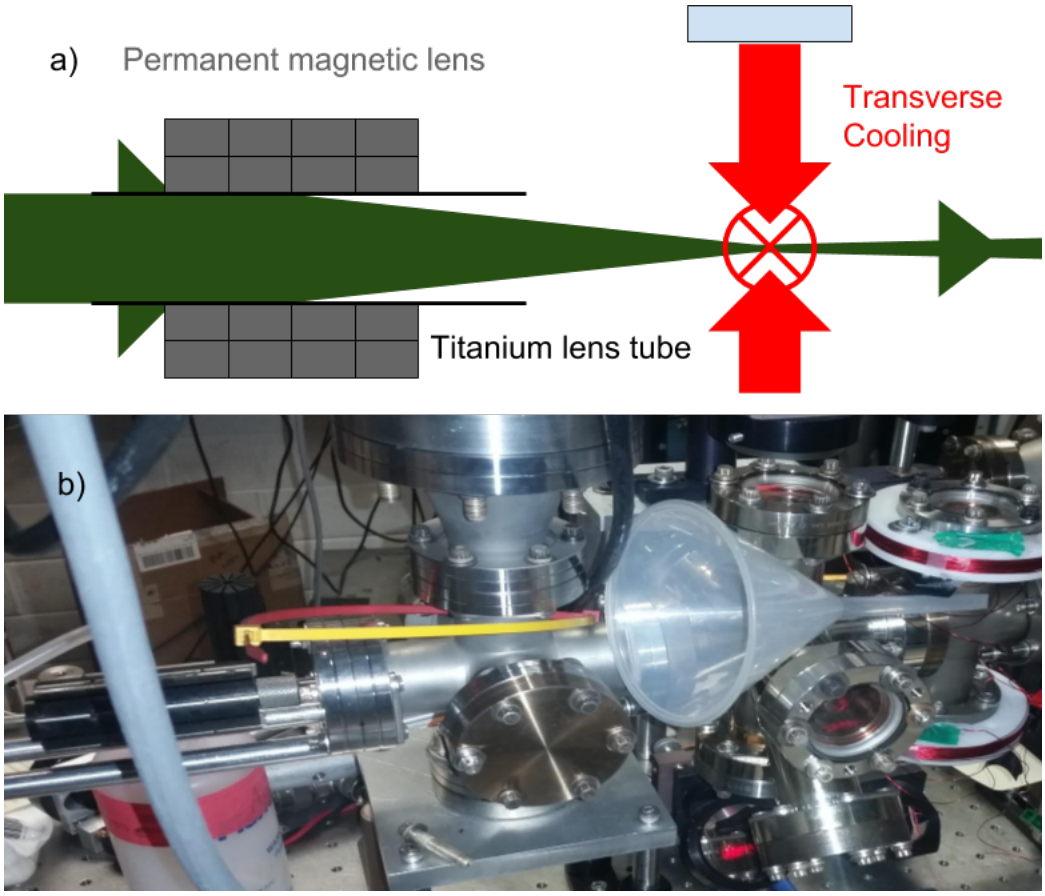

Figure 5.4: a) A cartoon of the atomic beam focused by a permanent magnetic lens and collimated by means of transverse laser cooling at its focus. (not to scale) b) A photograph of the atomic funneling portion of the beamline. A funnel is added to demonstrate the shape of the atomic beam as it is focused and cooled.

Chapter Six: Adjustable electromagnetic hexapole

Upon being focused and cooled by the permanent magnetic hexapole lens, the atomic beam undergoes a second round of optical pumping back to the low field seeking $m_j = 2$ state prior to propagating toward the adjustable magnetic lens. Rather than relying on static magnetic fields from permanent magnets, the adjustable electromagnetic lens relies upon the pulsed magnetic fields due to current carrying wires. The power of the lens and therefore the focal length will be determined by both the temporal duration and magnitude of the current passing through the electromagnets that form the magnetic lens.

6.1 Lens construction

The magnetic hexapole field for the adjustable electromagnetic hexapole lens is created using six straight current carrying rods, in the configuration demonstrated in Chapter 4. The rods themselves are 3.4 in. long, 1/16 in. diameter pure tungsten rods sold by McMaster Carr as welding electrodes[60]. Tungsten was chosen due to its low resistivity (52.8 nΩ m at 20 °C), comparable to that of copper (16.8 nΩ m) as well as its high stiffness (Young's modulus 411 GPa) comparable to that of stainless steel (Young's modulus 190 GPa). The high conductivity maximizes the current and therefore magnetic field strength for a given voltage. The stiffness allows the rods to be straight over a long region of space, a necessary condition to avoid geometric aberrations due to bends, kinks or other defects in the rods.

The six rods that make up the lens sit in trenches of two specially designed delrin mounts shown in Figure 6.1. The mounts are identical; one is at the front of the lens and one is at the back. The trenches are .064 in. wide and form an asterisk shape.

In the center of this asterisk shape is the lens tube, which is a 1/8 in. OD, 1/16 in ID polyether ether ketone (PEEK) tube. PEEK is a thermoplastic polymer with excellent vacuum properties[61]. It was chosen as it is UHV compatible, easily available, electrically insulating and relatively nonbreakable. Previous versions of this experiment have used Vespel, which is similar to PEEK, but is not sold in tube form, and glass which at the thickness needed is very breakable. Similarly to the titanium

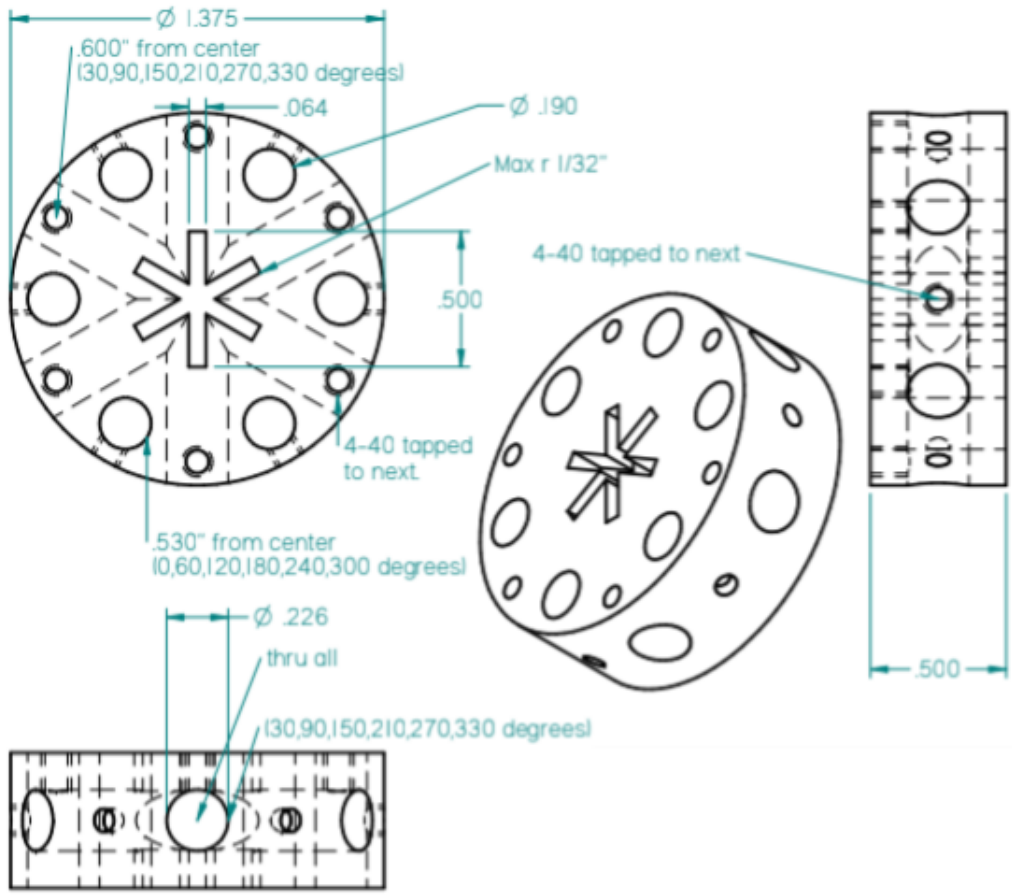

Figure 6.1: A part drawing of the delrin lens mount for the adjustable electromagnetic hexapole lens. The six tungsten current rods fit one each into the six flanges of the central asterisk shape. The PEEK lens tube sits inside the center of the six rods. The six holes perpendicular to the trenches serve to hold the 6-80 bushings and set set screws, while the holes parallel to trenches, but offset 60 degrees hold plastic rods that form a rigid structure around the lens.

lens tube for the permanent magnetic lens, the PEEK lens tube is attached to the vacuum chamber via quick connect fittings from Lesker[58].

The tungsten rods are pressed against the outside of the PEEK lens tube using twelve 6-80 set screws from Thorlabs, one for each rod for each delrin mount. The set screws themselves are held by in place by threaded bushings inserted into the outside of the delrin mounts. The centers of the tungsten rods will be a distance equal to the sum of their radius and the radius of the PEEK tubing from the center of the tube.

This gives us our value a for the hexapole radius:

$$a = 1/16'' + 1/32'' \approx 2.38\,\text{mm}. \tag{6.1}$$

Six plastic rods pass through each of the delrin mounts and serve as a rigid cage to preserve the straightness of the lens system and maintain the right angle between the lens tube and adjacent vacuum flanges. The entire lens assembly is shown in Figure 6.2.

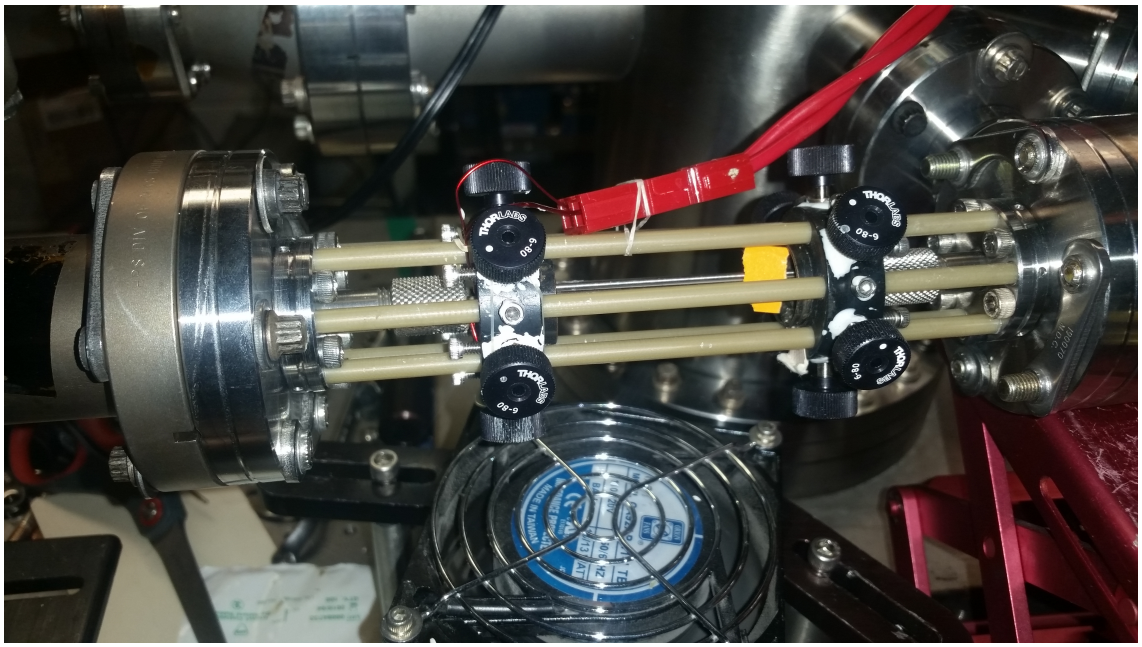

Figure 6.2: A photograph of the adjustable electromagnetic lens assembly.

Copper jumper wires are inserted between the tungsten rods and the 6-80 set screws. These jumper wires link each rod to the next such that the current passes through all six rods in alternating directions. Current will flow in one direction through a tungsten rod, then through the copper jumper before passing in the opposite direction through the next tungsten rod and so on and so forth until all six rods are connected. For the first and last connections, we use copper jumpers clamped with the 6-80 set screws to the tungsten rods on one end and fixed to an Anderson connector on the other end as is tradition in the Raizen Lab. This serves as the input/output for the electronics of the system.

6.2 Sources of geometric aberration

At the entrance and exit of the bore of a magnetic lens, the magnetic field does not immediately drop from its full strength to zero, but rather decays over a certain distance. These fringe fields are difficult to calculate and not necessarily ideal for focusing. One way to eliminate these fields is by only pulsing current through the magnetic lens when the atomic beam is fully inside the lens.

A second form of geometric aberration is aberration due to slightly misplaced tungsten rods. We simulate a magnetic field of a hexapole with a single rod misplaced by a distance 1/10 the radius of the lens as shown in Figure 6.3.

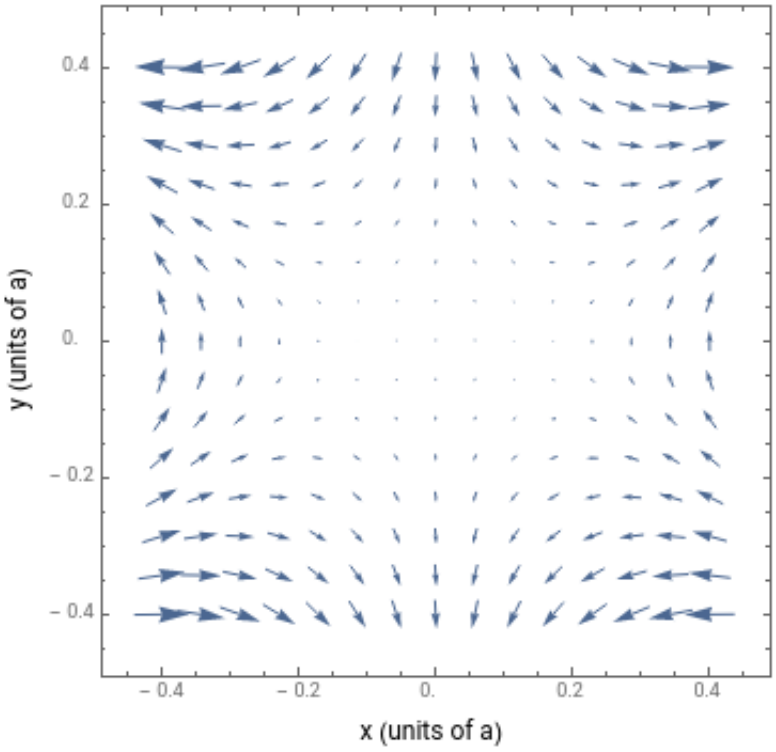

Figure 6.3: The magnetic field of an electromagnetic hexapole lens with the right most rod displaced outward by 1/10 the radius of the lens. There are two field zeroes horizontally separated along the x axis.

In this configuration, rather than having a single field zero at the origin or even a single zero offset from the origin, there are two spatially separated field zeroes, one on each side of the origin. Clearly, the $|B| \propto \rho^2$ approximation is no longer valid.

We should then expect the force on a low field seeking atom within the magnetic lens to be pointing to one or the other field zero as shown in Figure 6.4.

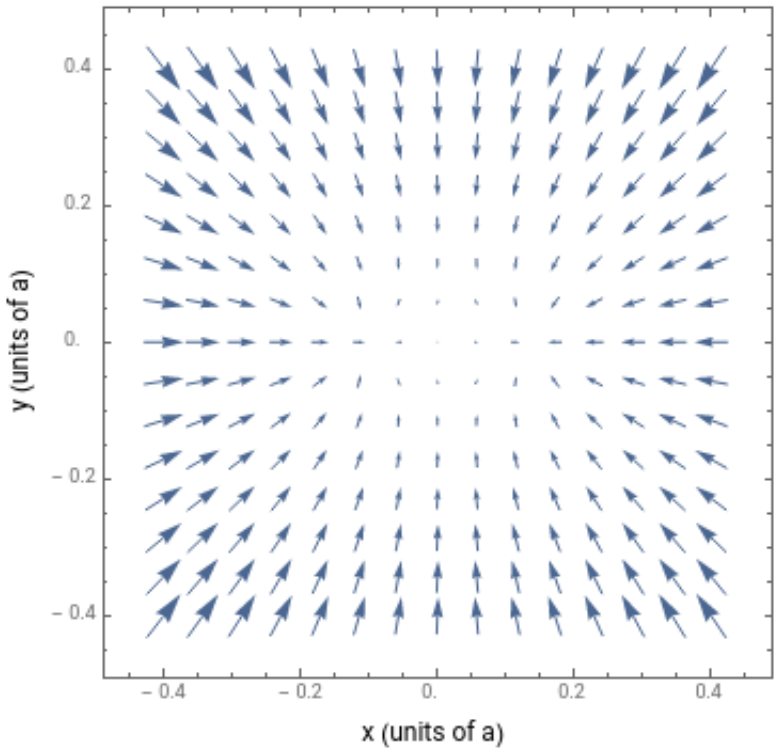

Figure 6.4: The force on a low field seeking atom within an electromagnetic hexapole lens with the right most rod displaced outward by 1/10 the radius of the lens. Atoms will feel a force toward either of the two horizontally separated field zeroes.

As the magnetic field is no longer proportional to the distance from the center of the hexapole, the atoms will no longer feel the ideal harmonic force necessary for focusing. The resulting force field will be towards one of two spatially separated local field minima.

A third source of geometric aberration is a background magnetic field. We simulated the magnetic field of a hexapole with a small bias field $\mathbf{B} = \mathbf{B}_{\text{hex}} + \mathbf{B}_{\text{bias}}$ as shown in Figure 6.5 and the associated force field in Figure 6.6.

If Figure 6.5 looks eerily similar to the magnetic field from a misaligned hexapole lens, it should. Consider again the case of the right most rod being displaced outward by a distance Δa. In its correct position, the current from this rod should create a

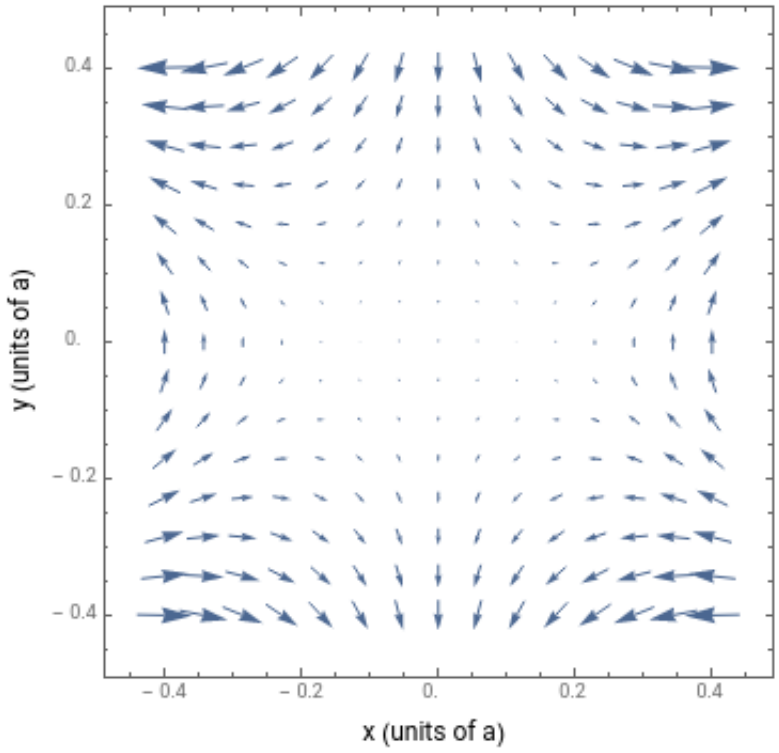

Figure 6.5: The magnetic field of an electromagnetic hexapole lens with a small downward bias field. The added bias field in the field shown has magnitude equivalent to 1/10 that of the magnitude of the magnetic field due to single current carrying rod a distance a from the origin. There are two field zeroes horizontally separated along the x axis.

field of

$$\mathbf{B}_{\text{Hex}} \approx \frac{\mu_0 I}{2\pi a}\hat{y}. \tag{6.2}$$

It instead creates a field of

$$\mathbf{B}_{\text{OffsetHex}} \approx \frac{\mu_0 I}{2\pi(a+\Delta a)}\hat{y}. \tag{6.3}$$

The difference between these fields is

$$\mathbf{B}_{\text{Offset}} \approx \frac{\mu_0 I}{2\pi a^2}(a-(a-+\Delta a))\hat{y}, \tag{6.4}$$

$$\mathbf{B}_{\text{Offset}} \approx -\frac{\mu_0 I}{2\pi a^2}(\Delta a)\hat{y}. \tag{6.5}$$

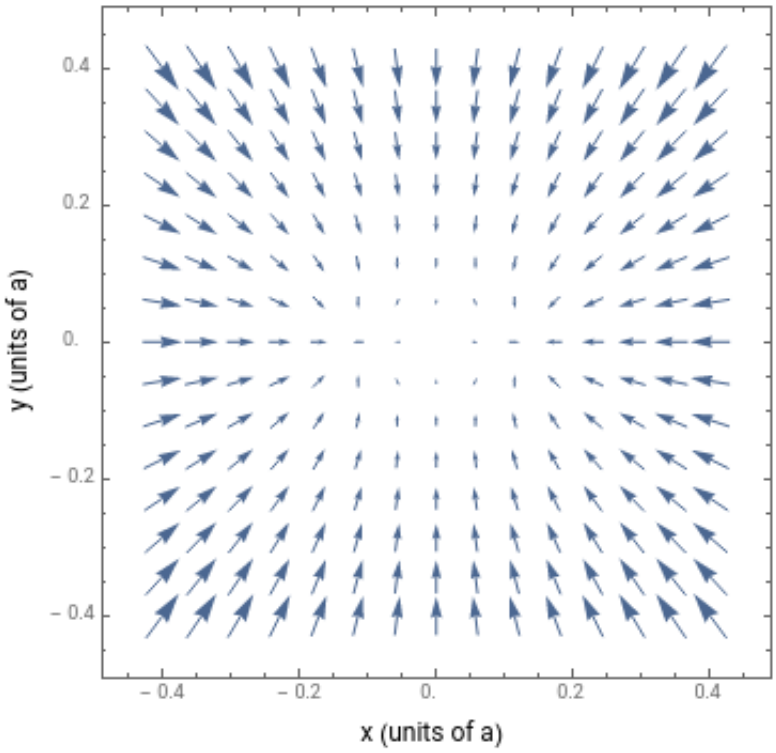

Figure 6.6: The force field on low field seeking atoms in an electromagnetic hexapole lens with a small downward bias field. The added bias field in the field shown has magnitude equivalent to 1/10 that of the magnitude of the magnetic field due to single current carrying rod a distance a from the origin. Atoms will feel a force toward either of the two horizontally separated field zeroes.

This difference in magnetic field strength is approximately equal to the ratio $\frac{\Delta a}{a}$ times the magnitude of the magnitude due to current from a single rod. For both the misplaced rod case as well as the external bias field case, we used a ratio of 1/10 for clarity.

A single method for mitigating both of these problems is the addition of two sets of modified Helmholtz coils, one for each dimension transverse to the direction of beam propagation. Instead of using circular coils, we use oblong racetrack shaped coils with long axis along the propagation direction so as to maintain a more uniform field along the length of the lens.

The magnetic field from these sets of coils creates a bias field that can either cancel out external bias fields or correct for (most of) aberrations due to radially misplaced

wires.

Nonuniform bias fields or skew rods on the other hand are pretty much impossible to correct for.

6.3 Focal length calculation

We calculate the focal length for the adjustable magnetic hexapole lens in a manner similar to how we calculated the focal length for the permanent magnetic hexapole lens.

We start with the force on a low field seeking atom inside the bore of the lens:

$$\mathbf{F} \approx -\mu_B m_j g_j \frac{12\rho\mu_0 I}{2\pi a^3}\hat{\rho}. \tag{6.6}$$

For low field seeking neon, $m_j = 2$ and $g_j \approx \frac{3}{2}$,

$$\mathbf{F} \approx -\mu_B \frac{18\rho\mu_0 I}{\pi a^3}\hat{\rho}. \tag{6.7}$$

We pulse the lens on for a finite amount of a time τ, giving a total velocity kick

$$\Delta v_\rho \approx -\mu_B \frac{18\rho\mu_0 I\tau}{\pi a^3 m}\hat{\rho}. \tag{6.8}$$

Using similar logic as we used for the permanent magnetic hexapole,

$$\frac{\Delta v_\rho}{v_z} = \frac{\rho}{f}. \tag{6.9}$$

This gives a lens power proportional to the magnitude and duration of the current passing through the lens. This is an interesting result as we now have a magnetic lens with a variable lens power and focal length:

$$\frac{1}{f} = \frac{\Delta v_\rho}{\rho}\frac{1}{v_z} \approx \frac{18\mu_0\mu_B I\tau}{\pi a^3 m}. \tag{6.10}$$

The focal length will then be

$$f \approx \frac{\pi a^3 m v_z}{18\mu_0\mu_B I\tau}. \tag{6.11}$$

Plugging in values, for a 50 µs pulse, the lens power will be

$$\frac{1}{f} \approx 0.015\,\mathrm{m}^{-1}\,\mathrm{A}^{-1}. \tag{6.12}$$

For a current of 100 A, this gives a focal length of $f \approx 66\,\mathrm{cm}$.

The power supply we use maxes out around 700 A, corresponding to a minimum focal length of $f \approx 9.5\,\mathrm{cm}$.

This is a much more robust approximation than that of the permanent magnetic hexapole case as we are able to eliminate fringe fields by pulsing the magnet only while the atomic beam is fully within the bore of the lens and more accurately judge the time for which the atoms feel a magnetic force. We can also reduce the pulse length to better approximate a thin lens.

6.4 Sources of chromatic aberration

Another source of aberration in atomic focusing is chromatic aberration. Analogous to light being focused differently at different wavelengths, chromatic aberration in atomic focusing is a result of atoms with different longitudinal velocities being focused differently.

6.4.1 Pulsed mode

In the previous section, we calculated the focal length of a pulsed adjustable electromagnetic lens. This approximation allows us to estimate with reasonable accuracy how far downstream an atom in the lens will be focused. One major problem however is the longitudinal extent of the atomic pulse. Atoms at the front of the atomic pulse will be focused to a spot further downstream than the spot to which atoms at the rear of the pulse will be focused, creating a smearing of the focal plane as shown in Figure 6.7.

One solution to rectify this is by applying a slight taper to the lens, such that the radius of the lens is wider at the front of the lens and narrower at the front of the lens. This allows for a weaker focusing effect on the atoms toward the back of the atomic pulse and a stronger focusing effect on atoms toward the front of the pulse, allowing the entire atomic pulse to be focused to the same focal plane. Chromatic aberration correction through lens tapering has not been verified experimentally, however the

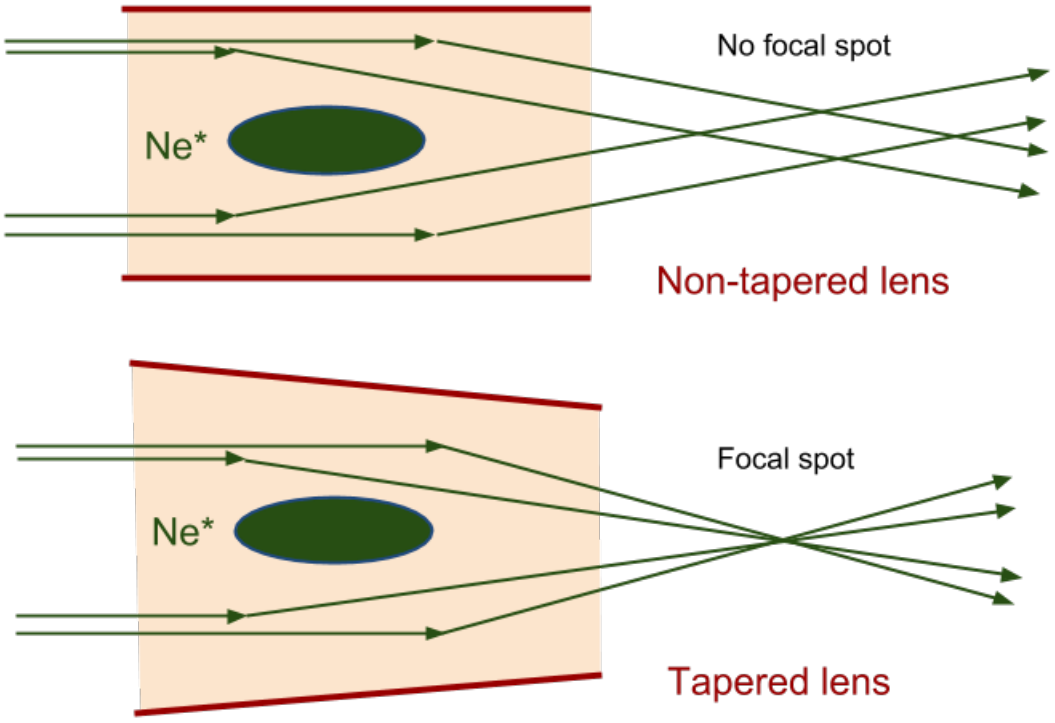

Figure 6.7: A diagram showing the focal plane smearing of a straight lens. Atoms at the front of the pulse will be focused to a plane ahead of the focal plane for atoms at the rear of the pulse. A slightly tapered lens ($< 1°$) creates a stronger focusing force on atoms at the front of the pulse and weaker focusing force on atoms at the back of the pulse, creating a single focal plane for all atoms regardless of longitudinal position.

current lens is designed such that small modifications can be made to allow for an adjustable taper. This will be further discussed in Chapter 9.

6.4.2 Pseudo-DC mode

In the pseudo-DC mode, we pulse current through the lens for a period of time substantially longer than the travel time of the atoms through the lens, such that the current is flowing through the lens for the entire duration of the atomic beam's travel through the lens. This solves the problem of different atoms being focused differently based on their position within the lens.

In this case, the effective time for which the lens is applying a force on the atomic

beam is given by $\tau = \frac{L}{v_z}$. Where L is the active length of the lens and v_z is the longitudinal velocity. While the tungsten rods are 3.4" long, the active area is only 2.9" long as the copper jumper wires are attached 1/4" from the ends of the tungsten rods. Substituting this into our calculation for the focal length gives

$$f \approx \frac{\pi a^3 m v_z^2}{18 \mu_0 \mu_B I L}. \tag{6.13}$$

Not considering geometric aberration due to the fringe fields the atoms experience as they enter and leave the lens,the v_z^2 dependence of the focal length will be a source of chromatic aberration with this configuration. Faster atoms will have a longer focal length than slower atoms. We do not have a means of correcting for this.

One benefit of the pseudo-DC mode is the lack of focal spot dependence on an atom's longitudinal position within the lens. Without aberration correction, this is the preferred method for lens operation. Another benefit comes from the longer pulse time requiring a smaller current to maintain a certain focal length. This decreases the power requirements of the lens, also reducing heating and vacuum outgassing.

6.5 Electronics and timing

The pulsed adjustable electromagnetic lens needs to be able to pulse currents up to 700 A for as short as 50 µs. We use a TDK Lambda max 300 V, 5 A power supply to charge a 6600 µF capacitor bank and use a Powerex BG2A gate driver that drives a Powerex CM600DU24NFH IGBT as a high speed, high voltage switch as shown in Figure 6.8.

When the lens is off and circuit is open, we send a 5 V signal to the driver. In order to close the circuit and fire the lens, we drop the 5 V input signal to 1 V for the amount of time we wish for the lens to remain on. The charge stored in the capacitor discharges through a 0.25 Ω resistor and the electromagnetic lens. The total resistance of the circuit is 0.42 Ω.

For such a high current application, heat management is definitely a concern. The most detrimental effect of heat in the system will be heating the PEEK lens tube and releasing moisture trapped in the walls of the tube. This will increase the pressure inside the vacuum and result in a significantly diminished beam. Prior to using the lens to focus atoms, we run the lens at high current 400 A and long pulse duration

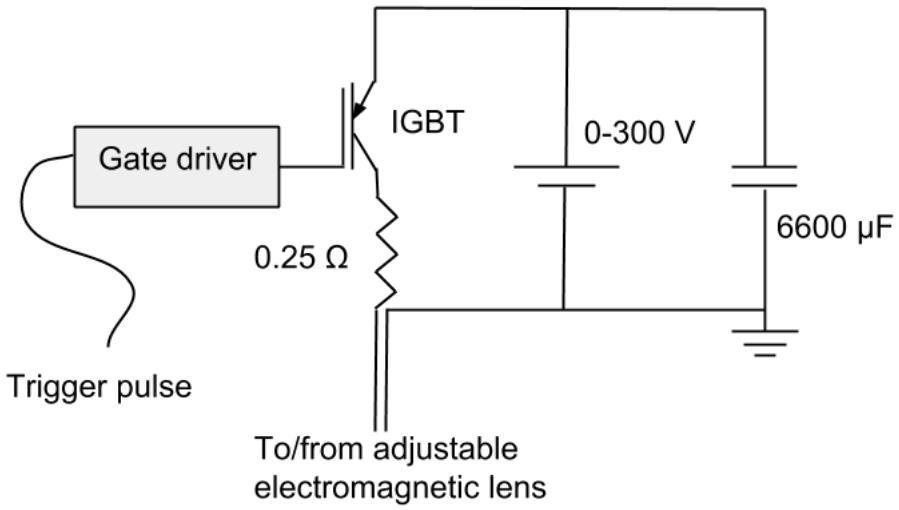

Figure 6.8: A simplified diagram of the circuit used to fire the adjustable electromagnetic lens.

400 µs so as to bake off remaining moisture trapped in the lens tube. During lens operation, we also use a small fan to forced air cool the lens assembly.

The proper lens timing is determined empirically. We use the Even-Lavie nozzle opening pulse to trigger a pulse generator with variable delay, which in turn triggers a function generator which sends out a 5 V signal, which drops to 1 V for a specified duration to trigger the lens circuit. We optimize the timing of the lens by scanning the delay from the nozzle pulse until the beam is most tightly focused.

If the tungsten rods and copper jumper wires are not secured by the 6-80 set screws, sparking may occur. Alternatively, electrical connection may be lost all together. In this case, it is important to disconnect the lens prior to repair. Even if the voltage is turned to zero, if you attempt to repair the lens while it is connected to the driver, you're gonna have a bad time.

Chapter Seven: Phase space representation

This chapter will analyze how each element of the complex atom lens affects the atomic beam in the phase space picture. If you choose to remember no other sentence of this dissertation, I recommend you remember this sentence: "A lens is a phase space rotation."

7.1 Phase space

In the phase space picture, the path of a particle is not analyzed in time, but rather in space. Instead of measuring position versus time, we measure conjugate momentum as a function of position. For the purposes of this chapter, we will analyze the transverse velocity of atoms within the atomic beam as a function of their transverse position.

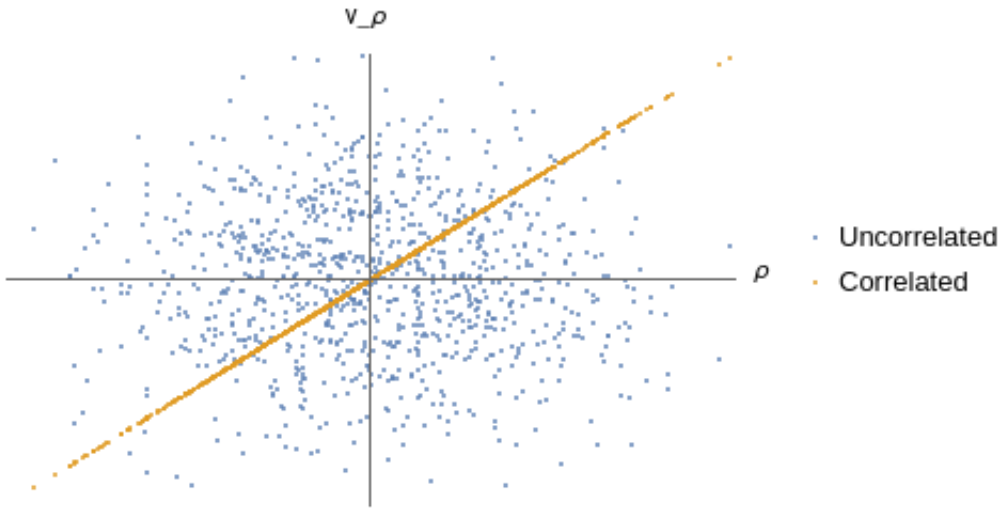

Figure 7.1: The phase space diagram for two ensembles of particles, both with identical σ_ρ and σ_{v_ρ}. It is intuitive to see that the uncorrelated ensemble has a much greater area and therefore phase space volume than the correlated ensemble.

The concept of phase space volume describes the area of a region in phase space $V_{ps} = \int d\rho dv_\rho$. Note that phase space volume does not necessarily equal $\sigma_\rho \sigma_{v_\rho}$ as ρ

and v_ρ are often correlated. This concept is much easier to see graphically in Figure 7.1.

Phase space density is an important concept in many areas of physics including Bose-Einstein condensation and ultracold atomic physics[62]. Here, phase space density will be defined $\rho_{\mathrm{PSD}} = \frac{n}{V_{ps}}$ where n is the density of atoms in real space.

A very important result of 19th century physics is Liouville's theorem, which states that local phase space density of a closed system is conserved[63]. Phase space density of an atomic beam is functionally equivalent to its brightness as introduced in Chapter 1.

7.2 Free propagation

The simplest phase space progression is the case of free propagation with no active elements. Experimentally, this occurs after atoms leave the nozzle, before they reach the magnetic lens. It is very difficult to explicitly measure the transverse velocities of atoms within the beam, however we can piece together a picture of their velocities using what we know about the positions and sizes of the atomic beam at various points along the beamline.

We know that all atoms start at the supersonic nozzle with an initial transverse radius less than 100 µm as that is the radius of the nozzle opening. We know that the beam then expands and propagates through the skimmer and toward the permanent magnetic lens. As the beam expands, atoms collide with each other and their velocity distribution randomizes. There will still be some correlation between position and velocity, however this correlation will not be one to one, as demonstrated in Figure 7.2.

7.3 Apertures

A very common technique in photon optics and electron optics is the use of an aperture to reduce the size of a beam. When a beam passes through an aperture, any particle outside the aperture will be effectively removed from the beam. The phase space representation of a beam passing through an aperture is shown in Figure 7.3. Assuming the densest part of the beam passes through the aperture, and less dense

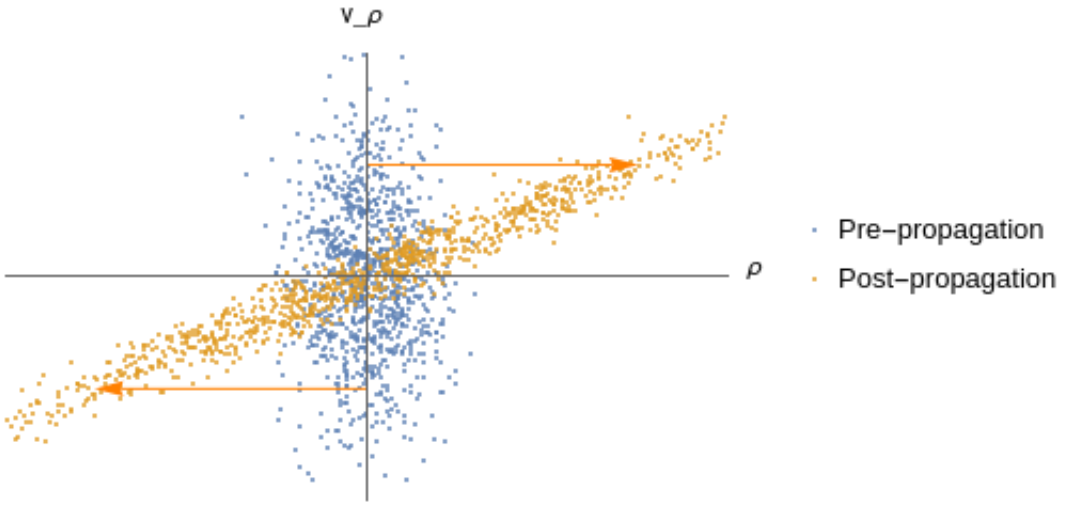

Figure 7.2: As a previously uncorrelated beam freely propagates in space, the faster atoms located in the upper half plane in phase space travel to the right and atoms in the lower half plane travel to the left. While σ_ρ and σ_{v_ρ} stays constant, phase space volume and therefore density remain conserved.

portions of the beam are blocked, this can be a means of increasing total phase space density of the beam, however it does not violate Liouville's theorem as the local phase space density does not change.

As the atomic beam reaches the titanium tube that serves as the bore of the permanent magnetic hexapole lens, a portion of the atoms will have radial position greater than the radius of the lens tube and will thus be blocked by the tube. Effectively, this is an aperture that cuts off the outside of the atomic beam.

7.4 Permanent magnetic lens

A magnetic lens provides a transverse kick to atoms in an atomic beam that is proportional to the distance between the atom and the axis of the lens. Using a thin lens approximation, this amounts to no change in the position of atom, but the transverse velocity will be shifted by an amount proportional its initial position. The total phase space volume will be conserved and because no atoms are lost, the phase space density is also conserved. The phase space evolution of a beam being focused by a magnetic lens is shown in Figure 7.4.

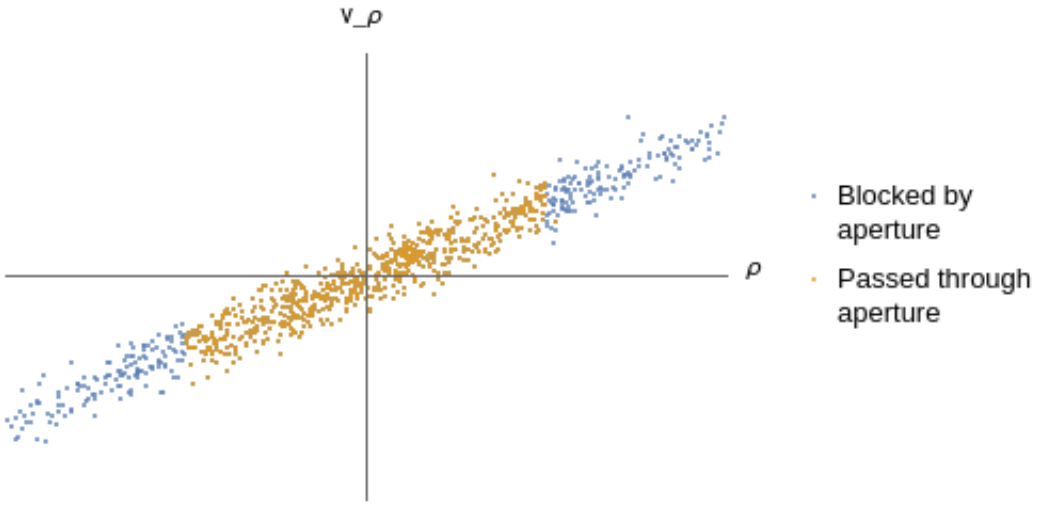

Figure 7.3: As an atomic beam passes through an aperture, any atoms outside the aperture will be blocked and removed from the beam.

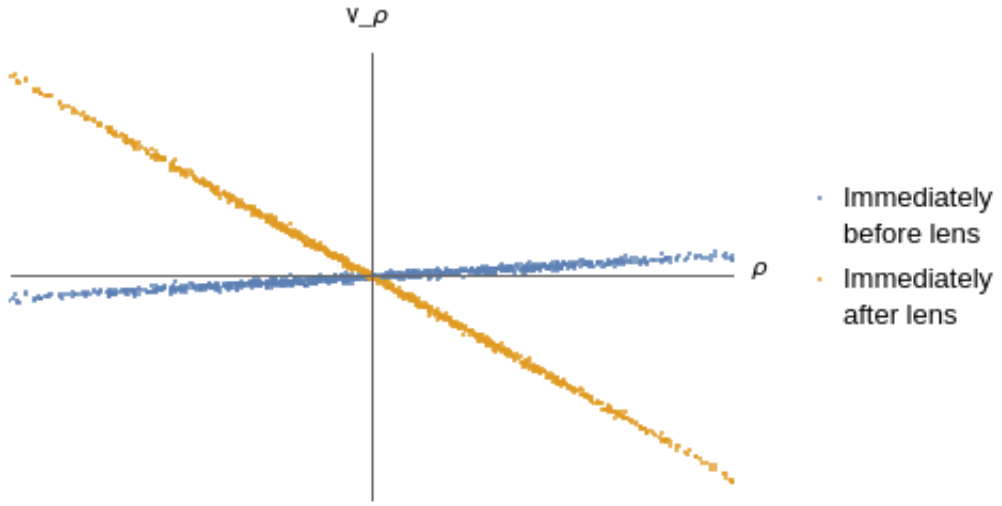

Figure 7.4: As the atomic beam passes through the magnetic lens, the transverse velocity of each atom is shifted by an amount proportional to its position.

In the phase space picture, this amounts to a rotation. A lens neither compresses or brightens an atomic beam, but merely rotates the beam in phase space.

The atomic beam then undergoes a round of free space propagation between the magnetic lens and its focal plane, the phase space representation of which is shown in Figure 7.5. This corresponds to another rotation, this time back towards the v_ρ

axis.

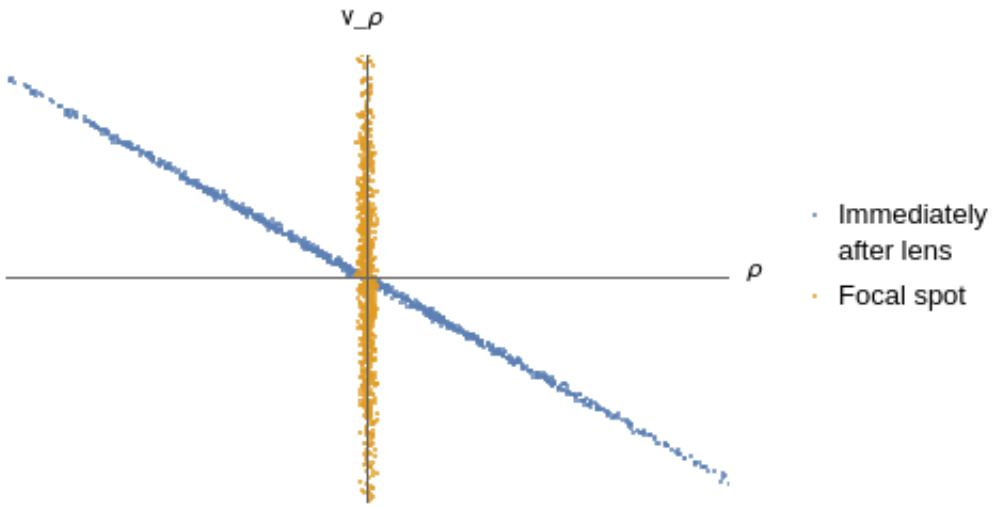

Figure 7.5: After passing through the magnetic lens, the atomic beam propagates toward a focal plane. The beam will be focused in the spatial dimension, but highly divergent.

Combining the propagation towards the lens, the lens kick, and subsequent propagation to the focal plane, the lensing system provides a three step rotation in phase space, trading a wide distribution in position and narrow distribution in velocity for a narrow distribution in position and wide distribution in velocity. At no point has the beam been brightened, merely rotated in phase space.

7.5 Laser cooling

At the focus of the magnetic lens, we apply transverse laser cooling to collimate the focused yet divergent beam. In the phase space picture, this amounts to compressing the beam along the v_ρ axis as shown in Figure 7.6. While this would appear to violate Liouville's theorem, keep in mind Liouville's theorem only applies to closed systems. An atomic beam being laser cooled is not a closed system as photons enter and leave the system. Coming in, the laser cooling photons are highly collimated and have near infinite phase space density. Upon absorption and spontaneous emission, photons are emitted in a random direction. This corresponds to a finite phase space

density. Thus the phase space density gained by the atomic beam corresponds to a phase space density decrease in the laser cooling beam.

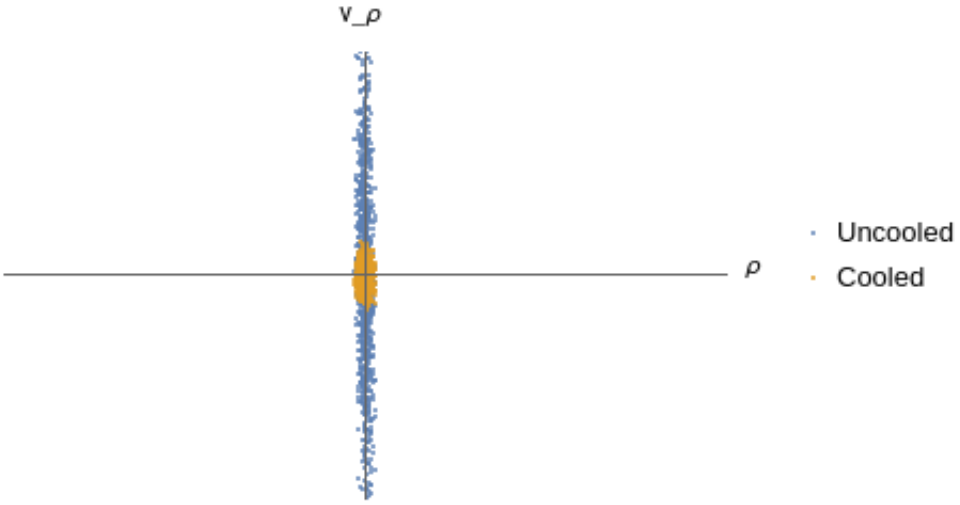

Figure 7.6: The phase space representation of the atomic beam as it is collimated by means of transverse laser cooleing.

The beam is now both focused and collimated with narrower position and velocity distributions than its initial values. The minimum achievable width of the final velocity distribution is given by the Doppler limit, as that is the lowest velocity that can be attained through laser cooling. Also, atoms with velocity greater than that of the capture limit will not be collimated via laser cooling and will continue on their merry way.

7.6 Focusing vs. imaging

After being focused and brightened, the atomic beam propagates toward the adjustable lens. At this point, the beam has a small divergence angle corresponding to the Doppler limit and a small initial spot size corresponding to its width at the collimation region. We independently analyze the case of a collimated beam and the case of a divergent beam with a small initial spot size. In phase space, these correspond to a beam with a wide position distribution and narrow velocity distribution and a beam with a narrow position distribution and wide velocity distribution respectively.

7.6.1 Focusing

The phase space representation of a perfectly collimated beam will not evolve as the beam freely propagates. For a nearly collimated beam whose initial transverse position distribution is much larger than the product of its transverse velocity distribution and its propagation time, the qualitative picture of the beam in phase space will not change. This is easier to see in real space than phase space.

As we know from geometric optics, a perfect lens will focus a collimated beam to (nearly) a single point. For a beam with a small divergence angle, we can estimate this deviation from this ideal point focus. We expect the spot size to be equal to the transverse spreading that would occur in a non-focused beam with the given initial divergence angle and propagation distance. This expected spreading is equal to the divergence angle multiplied by the image distance.

When I refer to focusing, I refer to focusing a collimated or nearly collimated beam that has not been defined by an aperture.

7.6.2 Imaging

Imaging a beam refers to passing a beam with a well defined shape through a lens. This beam shape is defined by an aperture. After passing through the aperture, the beam propagates toward a lens, followed by propagation toward an image plane. From geometric optics, we know that the expected image size is equal to the object size multiplied by the image distance divided by the object distance.

After our brightening mechanism, our beam has a somewhat collimated beam with a somewhat well defined shape and cannot be well characterized by either the focusing picture or imaging picture alone, but rather a hybrid of the two.

7.7 Adjustable electromagnetic hexapole lens

In the phase space picture, the pulsed electromagnetic lens is very similar to the permanent magnetic lens. The beam undergoes free propagation from the location of laser cooling toward the pulsed electromagnetic lens at which point it receives a momentum kick from the lens in a direction opposite that of its transverse position.

It then propagates towards the focal spot of the pulsed magnetic lens where it reaches our detector. In principle, it could again be laser cooled.

Each cycle of propagation, lens, propagation, cooling increases the phase space density of the beam. This is a general method that can be repeated as needed either until the desired phase space density is reached or lens aberrations become the dominant factor in beam brightness.

A shortcut in achieving high beam brightness or small spot size is the use of apertures. While the aperture does locally brighten the beam, it can allow for beams with higher average brightness and smaller spot size. An aperture placed after laser cooling and prior to beam propagation serves as an object plane for geometric imaging. Assuming a linear magnification factor, the final image size will be proportional to initial object size, meaning that a smaller aperture can give way to a smaller final spot size.

Chapter Eight: Results

This chapter will be dedicated to sharing the performance of the each novel aspect of the complex lens and will be broken up by physical element. I will first cover the permanent magnetic hexapole lens, followed by the beam brightening techniques and finish with an analysis of the adjustable magnetic hexapole lens.

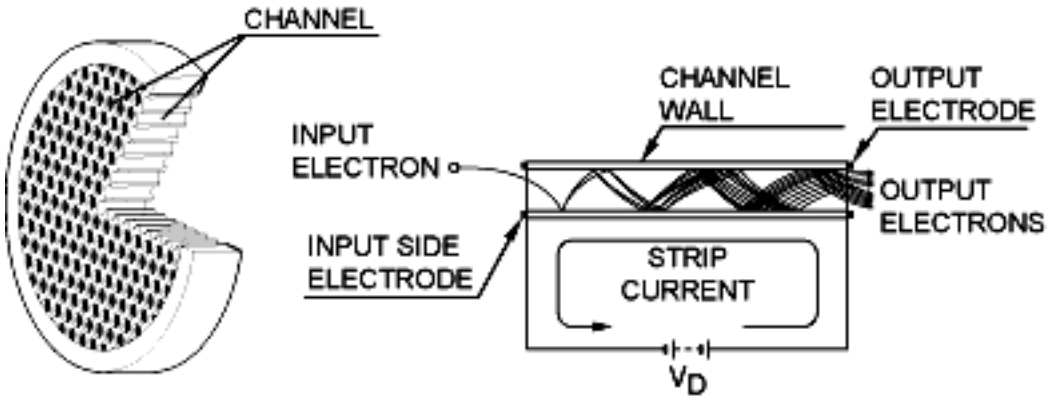

Figure 8.1: A schematic of a microchannel plate. Source: Del Mar Photonics. [64]

Experimentally, we analyze the performance of each element using a microchannel plate (MCP) and phosphor screen. The MCP itself consists of thousands of 10 µm channels nearly perpendicular to the face of the plate, a drawing of which is shown in Figure 8.1. When metastable atoms impinge on the MCP, they release a cascade of electrons along a microchannel. This cascade of electrons exits the back of the MCP and reaches a phosphor screen. When the electrons reach the phosphor screen, the screen phosphoresces, releasing light over the course of several milliseconds. We then capture a digital image of this light using a charge-coupled device (CCD) camera. Using software from Maxim DL, we can determine size, shape and relative density of our atomic beam.

8.1 Permanent magnetic hexapole

We analyze the performance of the permanent magnetic hexapole by placing the MCP and phosphor screen a distance 22 cm downstream from the permanent magnetic lens. We took images of the beam for five configurations of the permanent magnetic hexapole corresponding to zero, one, two, three, and four sets of hexapole magnets. When I refer to a set of hexapole magnets, I refer to a set of six magnets in a circle, each separated 60 degrees from the next, with alternating inward-outward polarization. Recall that each magnet is 3/4 in. long, so that each configuration corresponds to a permanent magnetic hexapole an integer multiple of 3/4 in. in length.

As shown in Figures 8.2, 8.3, and 8.4, as we start from taking an image of an unfocused beam and add magnets to the hexapole lens, the resulting image becomes brighter and narrower, corresponding to a denser and narrower atomic beam at the image plane 22 cm downstream from the lens.

Our magnetic lens mount can only hold four sets of hexapole magnets, so we cannot test longer magnetic lenses. In order to determine that four is in fact the optimal number of magnets, we extend the image distance of the system by placing the MCP further downstream from the magnetic lens. If four were an insufficient number of sets of magnets to bring the beam from its unfocused size of 6.4 mm FWHM to its narrowest extent of 1.5 mm FWHM, we would expect to see the beam continue to narrow as the image length increased, however throughout our tests, we did not see any decrease in spot size or increase in beam density for longer image lengths.

The MCP can also be operated in current collection mode, in which case instead of applying a voltage to the phosphor screen to produce two dimensional images, we use the phosphor screen as a current collector to determine the incoming number of atoms. The current output is equal to the atomic flux in atoms per second times the gain caused by the electron cascade in the MCP. The net gain of the system depends on the voltage applied to the MCP and varies from 100 to 1,000,000 from an applied voltage of 700 V to 2000 V. We convert this current to a voltage using a 100 kΩ IV converter. We then estimate the peak density of the atomic beam by dividing our calculated number of atoms reaching the screen per second by the area of the measured atomic beam. As the gain of the MCP is difficult to determine and

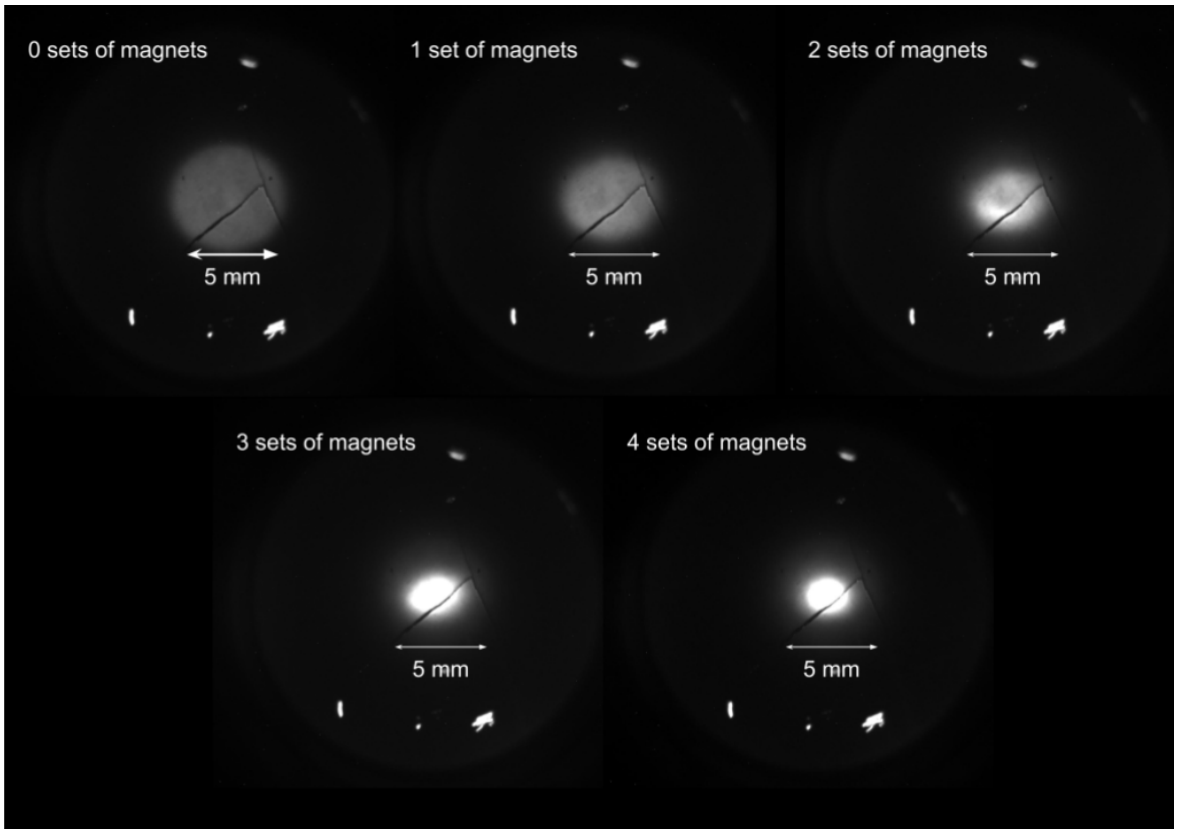

Figure 8.2: CCD images of a supersonic beam of metastable neon atoms focused by means of a permanent magnetic hexapole lens onto a MCP and phosphor screen for various lengths of permanent magnetic hexapole. The central circles are the atomic beam, which clearly come into focus as the number of sets of magnets approaches four. As you can see, there are several small light spots that correspond to scratches on the phosphor screen and two cracks on the MCP, which were actually quite convenient as they made focusing the camera on the screen rather easy.

varies across different MCP's, this gives us only a rough order of magnitude estimate of the atomic flux.

We estimate that for zero magnets ie. an unadulterated beam, we calculate our atomic beam to have a density of $1 \times 10^{12}\,\mathrm{s}^{-1}\,\mathrm{cm}^{-2}$, which is roughly in line with the number quoted from the literature on the Even-Lavie valve [33].

It is relative easy to calculate relative changes in beam density as the Maxim DL software gives relative brightness for each pixel. The relative brightness of the center of the atomic beam increases by a factor of 12 when the full magnetic lens consisting of four sets of magnets is added. This roughly corresponds to an increase from a

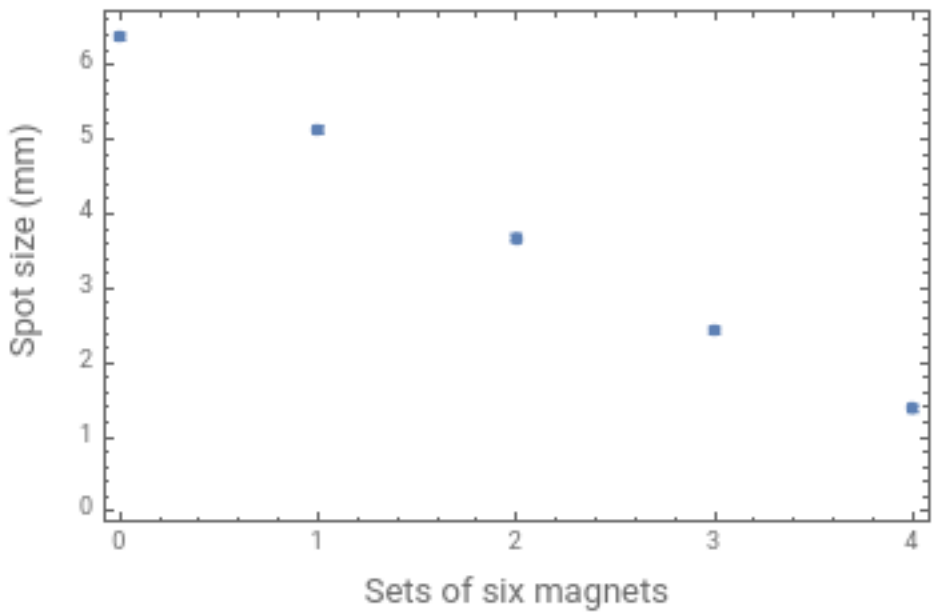

Figure 8.3: A graph depicting the width of the atomic beam (FWHM) as it is focused by a permanent magnetic hexapole lens onto an MCP. As the number of sets of hexapole magnets is increased from zero to four, the spot size decreases from 6.4 mm to 1.5 mm.

beam density of $1 \times 10^{12}\,\mathrm{s}^{-1}\,\mathrm{cm}^{-2}$ to $1 \times 10^{13}\,\mathrm{s}^{-1}\,\mathrm{cm}^{-2}$.

As the phase space profile of the beam entering the lens is difficult to define and we are subject to the many permanent magnetic lens aberrations as outlined in Chapter 5, this order of magnitude improvement in density and fourfold decrease in beam width reasonably agrees with expectation. This dense and narrow but divergent beam gives us an excellent starting point for beam brightening through transverse laser cooling.

8.2 Beam brightening

Beam brightness depends on both beam density and divergence angle. As we cannot measure divergence angle directly, we need a proxy. We measure the beam size at a distance 102 cm downstream from the beam brightening region and calculate the difference in beam size at this downstream spot from the beam size at the beam brightening region. This difference divided by the distance between the two measure-

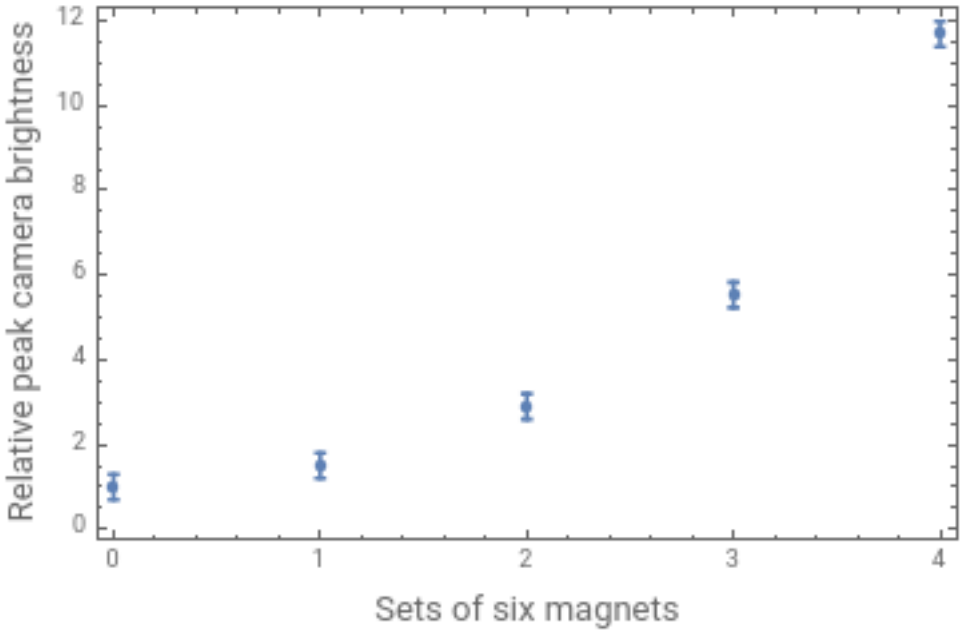

Figure 8.4: A graph depicting the detected relative peak brightness of the CCD image of a focused beam on an MCP with phosphor screen for varying length of permanent magnetic lens

ment points gives as an approximate divergence angle.

We compare the results of the beam brightened by means of focusing and cooling to a beam that is focused and not cooled, a beam that is cooled but not focused, and a beam that freely propagates without cooling or focusing.

We also take the same measurements of the beam, but with a 100 µm slit placed after laser cooling. This slit allows to calculate divergence angle using a much smaller starting spot size than that with cooling alone.

8.2.1 Baseline, no focusing or brightening

To get a baseline measurement for our beam brightening technique, we measure the spot of a freely expanding unadulterated beam. In this configuration, we do not use any magnetic lens to focus the beam, nor do we attempt to collimate the beam using laser cooling, the results of which are shown in Figure 8.5.

The peak beam density corresponds to a relative pixel brightness of 1 and the beam width is estimated to be 12.54 mm. Note the brightness measured is a good

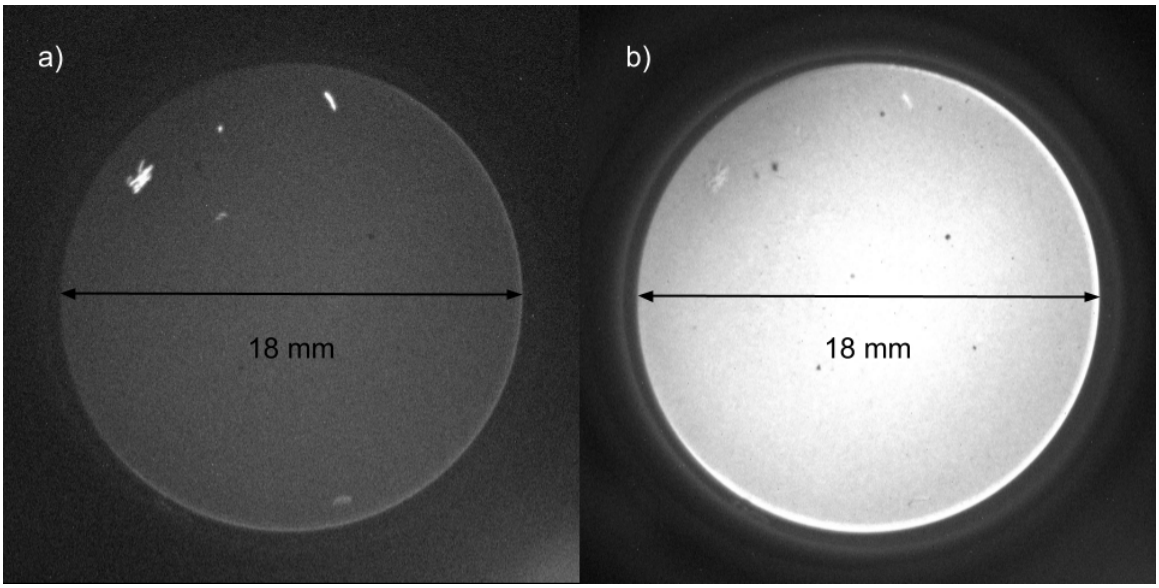

Figure 8.5: a) A CCD image of the atomic beam as it reaches the detector. In this case, the beam has been neither focused nor cooled. We set the relative peak pixel brightness to 1 and measure the width to be 12.54 mm b) A CCD image of a beam with the same parameters as in (a) but with higher gain and screen stretch to show beam features. The total beam size is on the order of the area of the detector (18 mm diameter).

tool for measuring relative beam density, but does not necessarily correspond to measurements made at different places along the beamline such as in Section 8.1.

The expected spot size can be estimated based purely on geometric arguments. The width of the beam divided by its total propagation length should equal the width of the beam at the magnetic lens, which is defined by the inner bore of the titanium lens tube, divided by the propagation distance from the nozzle to the end of the lens tube:

$$w_{\text{expected}} = w_{\text{lens tube}} \frac{z_{\text{detector}}}{z_{\text{lens tube}}} \frac{\sqrt{3}}{2}. \tag{8.1}$$

The factor of $\frac{\sqrt{3}}{2}$ comes from the conversion from measuring the full beam diameter inside the 4.5 mm lens tube to measuring the FWHM at the detector. We plug in 173 cm for the distance from the nozzle to the detector and 50 cm for the distance from the nozzle to the end of the lens tube:

$$w_{\text{expected}} = 4.5\,\text{mm}\frac{173\,\text{cm}}{50\,\text{cm}}\frac{\sqrt{3}}{2} \approx 13.48\,\text{mm}. \tag{8.2}$$

This is in reasonable agreement with our measured value of 12.54 mm as we made an assumption that the beam can be treated as coming from a point source at the nozzle, which is not strictly true.

8.2.2 Brightening without focusing

We next attempt to measure the effect of laser cooling without a magnetic lens. This is equivalent to collimating a divergent beam rather than collimating a focused beam, the results of which are shown in Figure 8.6.

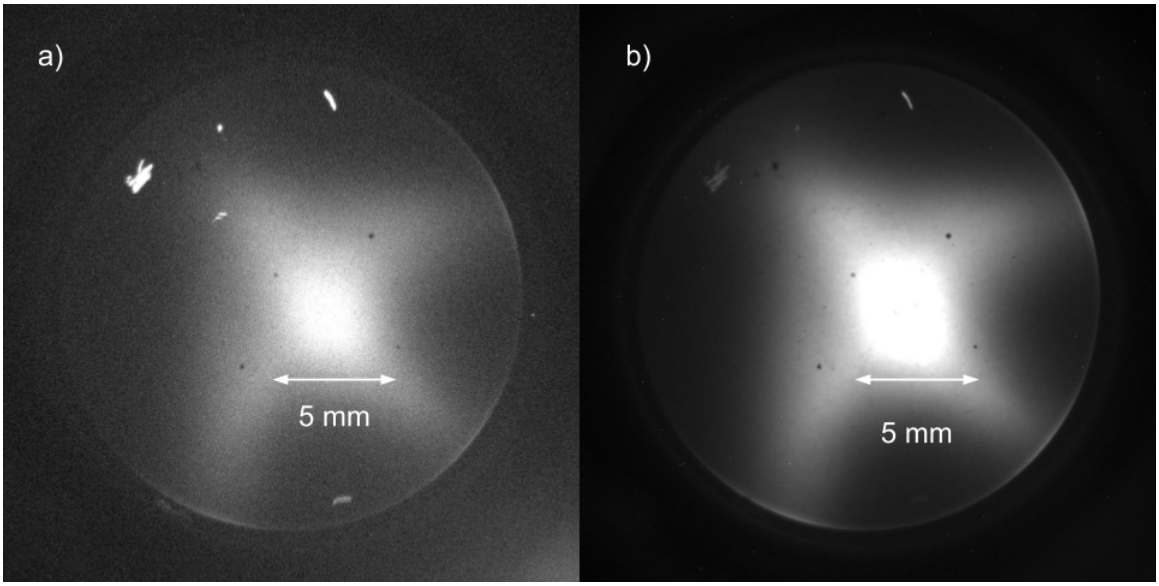

Figure 8.6: a) A CCD image of the atomic beam as it reaches the detector. In this case, the beam has collimated but not focused. The relative peak pixel brightness is 11.1 and the width is 4.73 mm. b) A CCD image of a beam with the same parameters as in (a) but with higher gain and screen stretch to show beam features.

The peak beam density corresponds to a relative pixel brightness of 11.1 and the beam width is 4.73 mm. From geometric arguments, we should expect the beam width to be equal to the beam width at the point of collimation which is determined by the geometry of the system, plus a small factor to account for further expansion due to the nonzero collimating limit of Doppler cooling.

We can calculate this expected Doppler limited beam spreading. Our beam is travelling longitudinally at $490\,\mathrm{m\,s^{-1}}$ for a distance of 102 cm. The Doppler limit is $28.5\,\mathrm{cm\,s^{-1}}$. The ratio of beam spreading to beam propagation should be the ratio of the Doppler limit to the longitudinal velocity:

$$\Delta w_{\mathrm{Doppler}} = \Delta z \frac{v_{\mathrm{Doppler}}}{v_z}, \tag{8.3}$$

$$\Delta w_{\mathrm{Doppler}} \approx 625\,\mu\mathrm{m}. \tag{8.4}$$

We are working in full width half maximum, so we need to multiply the ratio of FWHM to standard deviation:

$$\frac{FWHM}{\sigma} \approx 2.355. \tag{8.5}$$

$$\Delta w_{\mathrm{DopplerFWHM}} \approx 1.47\,\mathrm{mm}. \tag{8.6}$$

We add this to to the width of the unfocused beam measured at the collimation region in section 8.1:

$$w_{\mathrm{expected}} \approx 1.5\,\mathrm{m} + 6.4\,\mathrm{mm} \approx 7.9\,\mathrm{mm}. \tag{8.7}$$

Our measured value is significantly smaller than this expected value, so we know that other dynamics must be at play. The reader should note the X shape in Figure 8.6. This X shape is a result of the laser cooling beams being designed to collimate a focused beam rather than collimate a several millimeter wide beam. The corners of the atomic beam are outside the range of the laser cooling beams and will not be focused. It is these atoms that form the wings of the X shapes. When calculating the FWHM of the collimated beam, these atoms do not factor into the equation as they are well outside the region enclosed by the FWHM, rendering our measured FWHM artificially small.

When compared to the non-collimated case, laser cooling results in an increase of a factor of 11 in beam density and a decrease by a factor of 2.65 in beam diameter. We can set an upper limit on the brightness increase by treating the beam width to be proportional to the divergence angle. This is not strictly true as the initial spot size is nonzero, but this is a reasonable upper bound. The two dimensional phase

space density increase will then be measured by the net change in peak beam density as divergence angle should be reasonably correlated with transverse position. This corresponds to increase by a factor of 11 in brightness, however with a large margin of error in that estimate.

8.2.3 Focusing without brightening

Another interesting test is focusing the beam without brightening it, the results of which are shown in Figure 8.7. Keep in mind, we have not moved the detector and are in essence measuring the beam 102 cm downstream from its focus.

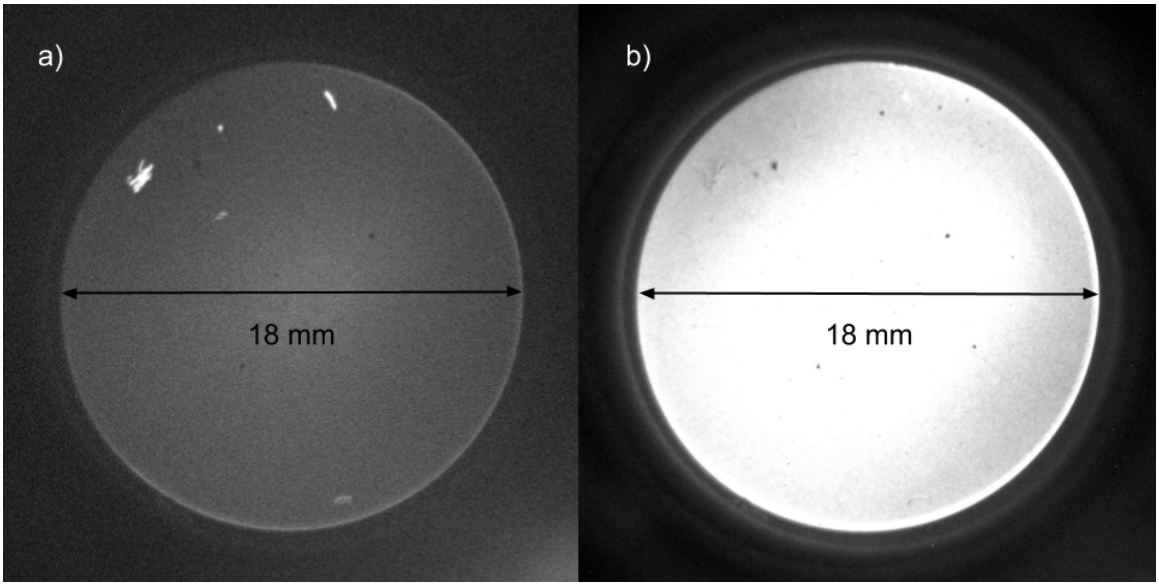

Figure 8.7: a) A CCD image of the atomic beam as it reaches the detector. In this case, the beam has been focused but not collimated. The relative peak pixel brightness is 2.0 and the width is 7.81 mm b) A CCD image of a beam with the same parameters as in (a) but with higher gain and screen stretch to show beam features.

The peak beam density corresponds to a relative pixel brightness of 2.0 and the beam width is 7.81 mm. This corresponds to a badly out of focus beam. Geometrically, we expect the beam to defocus at the same angle at which it focused. Mostly, this image is included to show the effects of laser cooling on a focused beam.

8.2.4 Focusing and brightening

Our final beam brightening measurement without using a slit consists of our complete focusing and beam brightening mechanism, the results of which are shown in Figure 8.8. Both the magnetic lens and laser cooling have been restored.

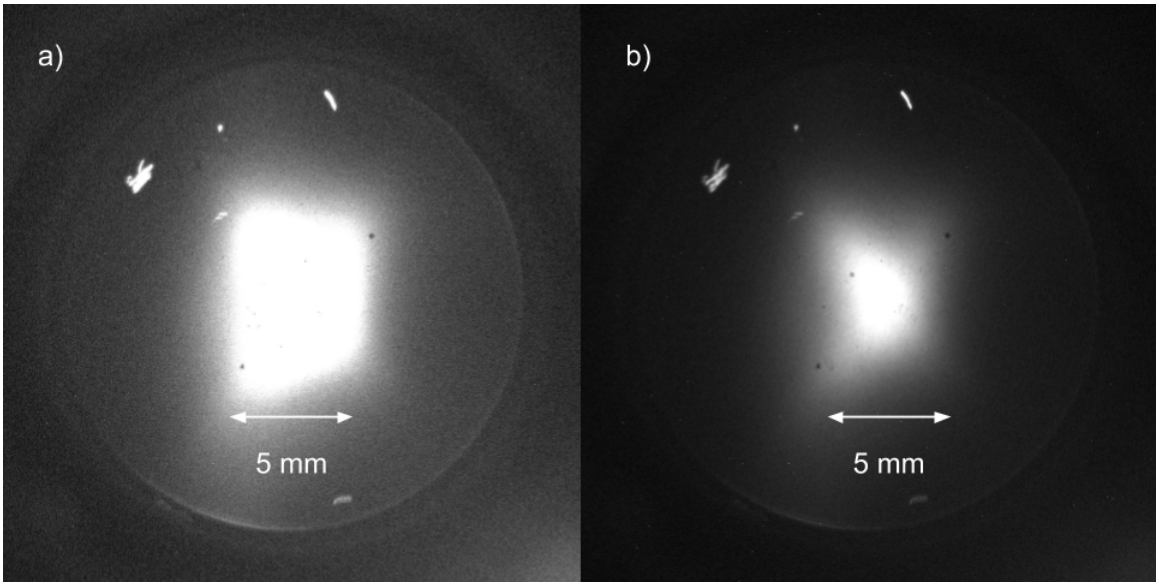

Figure 8.8: a) A CCD image of the atomic beam as it reaches the detector. In this case, the beam has been both focused and collimated. The relative peak pixel brightness is 36.3 and the width is 3.39 mm b) A CCD image of a beam with the same parameters as in (a) but with lower gain and screen stretch to show beam features.

The peak beam density corresponds to a relative peak pixel brightness of 36.3 and the beam width is 3.39 mm. This represents an increase by a factor of 36.3 in density and 3.7 in width over the free propagating case and a factor of 3.25 in density over the collimated but not focused case.

The expected spot size is given by the spot size at the focus given by the permanent magnetic lens measurements plus the expected beam spreading due to Doppler limited cooling. The width at the focus is 1.5 mm, plus a Doppler limited spreading of 1.47 mm gives an expected beam extent of 3 mm.

Note, the X shape of the beam due to poorly collimated atoms is still slightly present, however in this case, the wings of the X are inside the FWHM region, artificially inflating the measured FWHM.

The transverse velocity spread is given by the net change in spot size divided by the propagation time.

For the brightened case, this is

$$v_{\rho\mathrm{FWHM}} \approx \frac{3.4\,\mathrm{mm} - 1.5\,\mathrm{mm}}{102\,\mathrm{cm}} 490\,\mathrm{m\,s^{-1}} \approx 93\,\mathrm{cm\,s^{-1}}. \tag{8.8}$$

For the non-brightened case this is

$$v_{\rho\mathrm{FWHM}} \approx \frac{12.5\,\mathrm{mm} - 6.4\,\mathrm{mm}}{102\,\mathrm{cm}} 490\,\mathrm{m\,s^{-1}} \approx 298\,\mathrm{cm\,s^{-1}}. \tag{8.9}$$

For the brightened case, the divergence angle (standard deviation) is

$$\alpha_\rho \approx \frac{3.4\,\mathrm{mm} - 1.5\,\mathrm{mm}}{102\,\mathrm{c} \times 490\,\mathrm{m\,s^{-1}} \times 2.36} \approx 8 \times 10^{-4}\,\mathrm{rad}. \tag{8.10}$$

For the non-brightened case the divergence angle (standard deviation) is

$$\alpha_\rho \approx \frac{12.5\,\mathrm{mm} - 6.4\,\mathrm{mm}}{102\,\mathrm{cm} \times 490\,\mathrm{m\,s^{-1}} \times 2.36} \approx 2.6 \times 10^{-3}\,\mathrm{rad}. \tag{8.11}$$

Using our previously calculated value of atom density of $10^{13}\,\mathrm{cm^{-2}\,s^{-1}}$ at the image plane of the permanent magnetic hexapole lens and our estimated value of divergence angle of $10^{-6}\,\mathrm{sr}$, we estimate a total brightness of $10^{19}\,\mathrm{cm^{-2}\,s^{-1}\,sr^{-1}}$.

At this point, we cannot merely divide the relative beam density by the square of the divergence angle to get a relative beam brightness as we do not know the correlation coefficients between transverse position and transverse velocity.

We can estimate the correlation between transverse position by assuming that the correlation is proportional to the propagation distance from the collimation region to the detector. For the non-brightened case, there is no collimation region, but we can use the lens tube as a proxy for collimation region.

The beam brightness will be proportional to the beam density multiplied by the square of the collimation region, which is 102 cm for the brightened case and 123 cm for the unbrightened case. We take the square of the distance to account for one power for each transverse dimension:

$$\frac{B_{\mathrm{brightened}}}{B_{\mathrm{non\text{-}brightened}}} \approx \frac{\rho_{\mathrm{brightened}}}{\rho_{\mathrm{non\text{-}brightened}}} \frac{\Delta z^2_{\mathrm{brightened}}}{\Delta z^2_{\mathrm{non\text{-}brightened}}}, \tag{8.12}$$

$$\frac{B_{\mathrm{brightened}}}{B_{\mathrm{non\text{-}brightened}}} \approx 36.3 \frac{(123\,\mathrm{cm})^2}{(173\,\mathrm{cm})^2} \approx 23. \tag{8.13}$$

We estimate our method of beam brightening through magnetic focusing and transverse cooling to increase the brightness of our atomic beam by a factor of 23. However, as assumptions were made regarding the propagation region and associated correlation between the transverse positions and velocities, we need a second mechanism to estimate the increase in beam brightness.

8.2.5 Focusing and collimating through a slit

To better measure the divergence angle and its correlation with beam width, we insert a 100 µm slit a distance 15 cm after the collimating region and repeat the measurements from the previous section. This gives us a much clearer initial conditions for our beam, allowing us to more accurately estimate the increase in brightness.

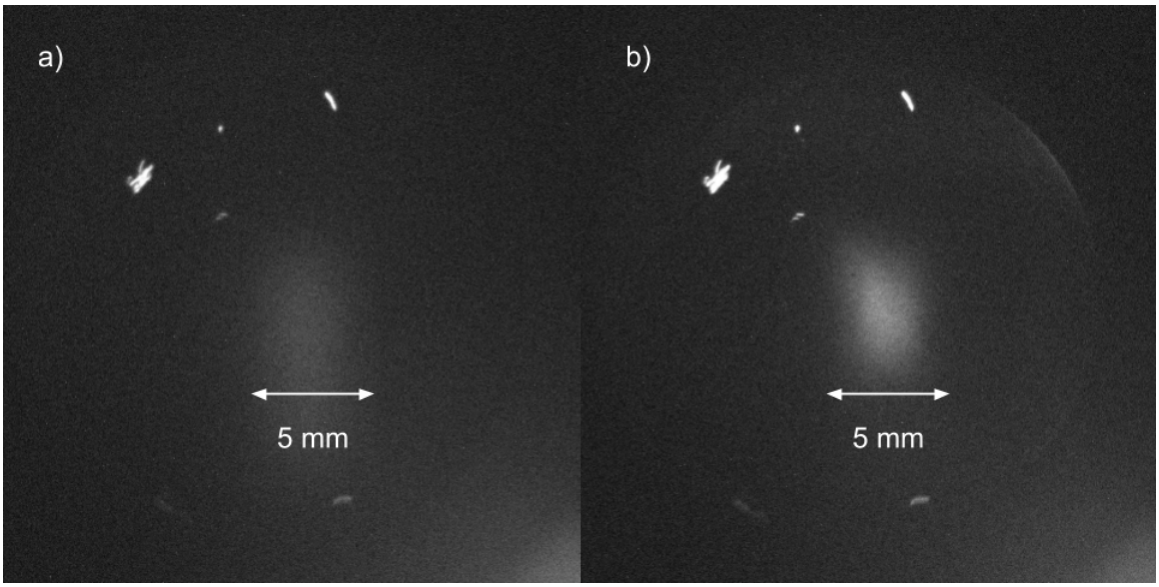

Figure 8.9: a) A CCD image of the atomic beam as it reaches the detector. In this case, the beam has been neither focused nor collimated. We set the relative peak pixel brightness to be 1 and measure the width to be 8.67 mm. b) In this case, the beam has been collimated but not focused. The relative peak pixel brightness is 2.8 and the width is 2.38 mm.

For the baseline case of no focusing or cooling, we set the relative peak beam density to be 1 and measure a beam width of 8.67 mm. Figure 8.9, section (a) shows an image of the beam as it reaches the detector. We estimate the transverse velocity

to be equal to the beam width divided by the propagation distance 87 cm from the slit to the detector multiplied by the longitudinal velocity:

$$v_{\rho\mathrm{FWHM}} \approx 490\,\mathrm{cm\,s^{-1}}. \tag{8.14}$$

For the case of laser cooling without focusing, we measure a relative peak beam density of 2.8 and a beam width of 2.38 mm. Figure 8.9, section (b) shows an image of the beam as it reaches the detector. This gives a transverse velocity of

$$v_{\rho\mathrm{FWHM}} \approx 130\,\mathrm{cm\,s^{-1}}. \tag{8.15}$$

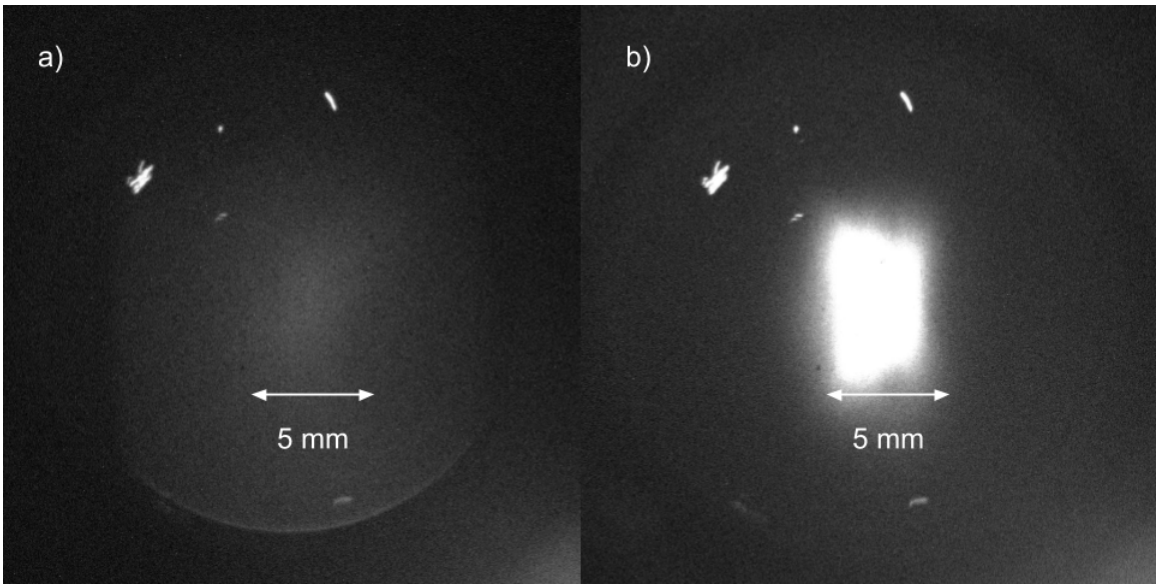

Figure 8.10: a) A CCD image of the atomic beam as it reaches the detector. In this case, the beam has been focused but not collimated. The relative peak pixel brightness is 1.4 and the width is 6.56 mm. b) In this case, the beam is both focused and collimated. The relative peak pixel brightness is 21 and the width is 2.42 mm.

When we add the magnetic lens back in, and send the focused, collimated beam through the 100 µm slit, we measure a beam with relative peak density 21 and width 2.42 mm. Figure 8.10, section (b) shows an image of the beam as it reaches the detector. The width is not substantially different than the width of the beam that had been collimated but not focused, but is significantly denser. This makes sense as the transverse temperature of both beams should be the same, but the focused beam is able to funnel significantly more atoms through the 100 µm slit.

Combining focusing and collimating gives an increase of a factor of 21 in beam density. As we know both the brightenend and non-brightened beam had the same 100 µm starting size, we know that transverse position will be nearly proportional to transverse velocity. This means that the correlation coefficient will be proportional to the divergence angle of the beam. When calculating the relative increase in brightness, the transverse velocity and correlation coefficient cancel out:

$$\frac{B_{\text{brightened}}}{B_{\text{non-brightened}}} \approx \frac{\rho_{\text{brightened}}}{\rho_{\text{non-brightened}}} \frac{w^2_{\text{non-brightened}}}{w^2_{\text{brightened}}} \frac{v^2_{\rho\text{FWHMbrightened}}}{v^2_{\rho\text{FWHMnon-brightened}}}, \tag{8.16}$$

$$\frac{B_{\text{brightened}}}{B_{\text{non-brightened}}} \approx \frac{\rho_{\text{brightened}}}{\rho_{\text{non-brightened}}} \approx 21. \tag{8.17}$$

This estimated 21 fold increase in beam brightness is in relative agreement with the previously estimated brightness increase of a factor of 23. Given the uncertainty in the system, we conservatively set the lower bound of our increase in beam brightness to be a factor of 20.

8.3 Adjustable magnetic hexapole

We next characterize the ability of our adjustable electromagnetic lens to focus our brightened beam of atoms. We operate the magnetic lens in a pseudo -DC mode for which the magnetic lens is pulsed for 400 µs, longer than the duration of travel through the lens.

We operate the magnetic lens in the pseudo-DC mode for four different beam configurations. The first method is imaging a 100 µm slit an object distance 92 cm upstream from the magnetic lens with an image distance of 42 cm. The second is imaging the brightened beam after a propagation distance of 107 cm and image distance of 42 cm with no aperture other than the magnetic lens aperture defined by the 1/16 in. inner diameter of the PEEK lens tube. The third maintains the propagation distance 107 cm but shortens the image distance to 13.5 cm. In the fourth method, we shorten the propagation distance to 37 cm and maintain the image distance of 13.5 cm.

The pseudo-DC mode allows all atoms to feel the focusing force at the same place, but does not correct for fringe fields or chromatic aberration. This does not

introduce as much chromatic aberration as would be caused by using a quickly pulsed lens without a taper.

8.3.1 Imaging a slit

We begin by analyzing the lens' performance imaging a slit. We set up the experiment by passing the beam through a 100 µm slit after being brightened and optically pumped back to the low field seeking state. The beam then propagates for 92 cm toward the magnetic lens before being imaged onto an MCP and phosphor screen a distance 42 cm downstream from the lens. We vary the current passing through the lens and measure the beam width and relative beam density at each value of lens current. The optimal lens current will correspond to the imaged beam with narrowest width or highest brightness as shown in Figures 8.11 and 8.12.

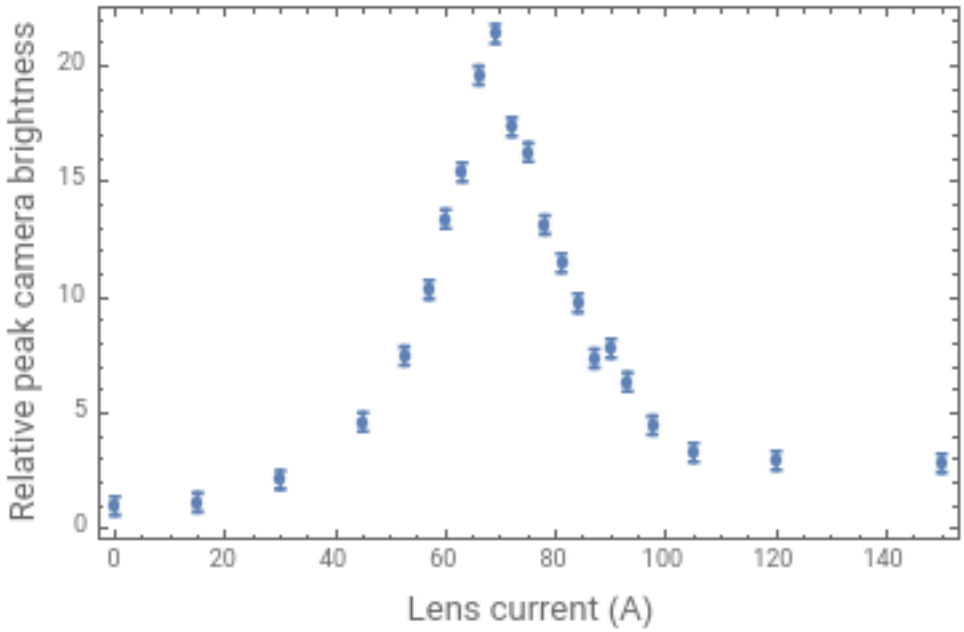

Figure 8.11: The relative brightness of an imaged slit with respect to lens current.

The peak beam density for a beam imaged by a lens with current 69 A is a factor of 21.4 times greater than that of an unfocused beam.

According to our calculations of lens focal in length in section 6.3, the expected focal length is given by

$$f \approx \frac{\pi a^3 m v_z^2}{18 \mu_0 \mu_B} \approx 32\,\text{cm}. \tag{8.18}$$

Based on geometric optics, we can estimate a focal length based on the object and image lengths. For image length $i = 42\,\text{cm}$ and object length $o = 92\,\text{cm}$

$$\frac{1}{f} = \frac{1}{i} + \frac{1}{o} \approx \frac{1}{29\,\text{cm}}. \tag{8.19}$$

This is reassuring as the expected lens focal length based on the lens current is within 10 % of the estimated value based on geometric optics.

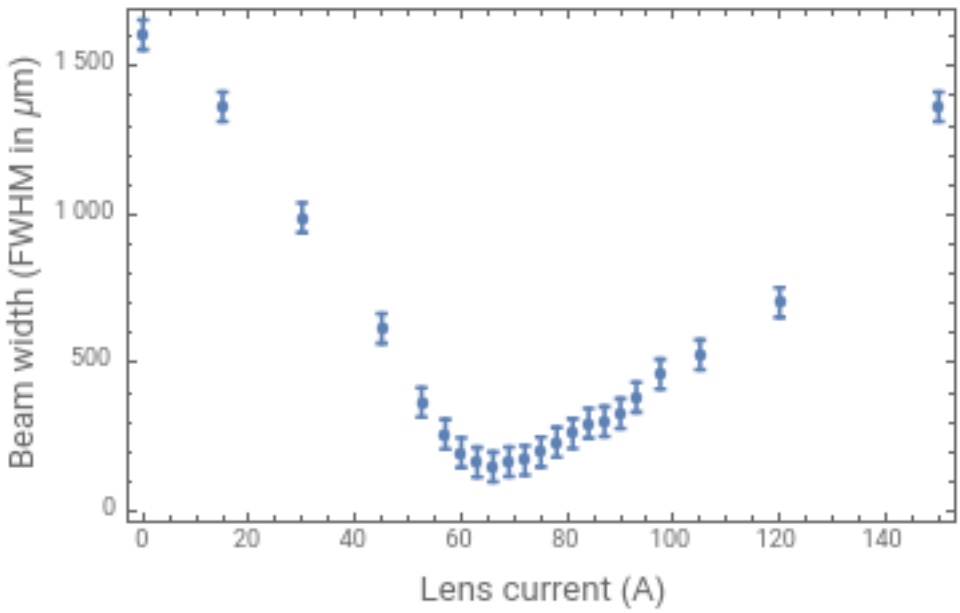

Figure 8.12: The FWHM of the imaged slit with respect to lens current.

The minimum measured beam width is 150 µm corresponding to a lens current of 66 A and a corresponding expected lens focal length of 33 cm.

The focal length checks out, however imaging a 100 µm slit down to a 150 µm width is not terribly impressive. According to geometric optics, we should expect a magnification factor given by

$$M = \frac{i}{o} \approx \frac{42\,\text{cm}}{92\,\text{cm}} \approx .46. \tag{8.20}$$

This would correspond to a spot size of 46 µm.

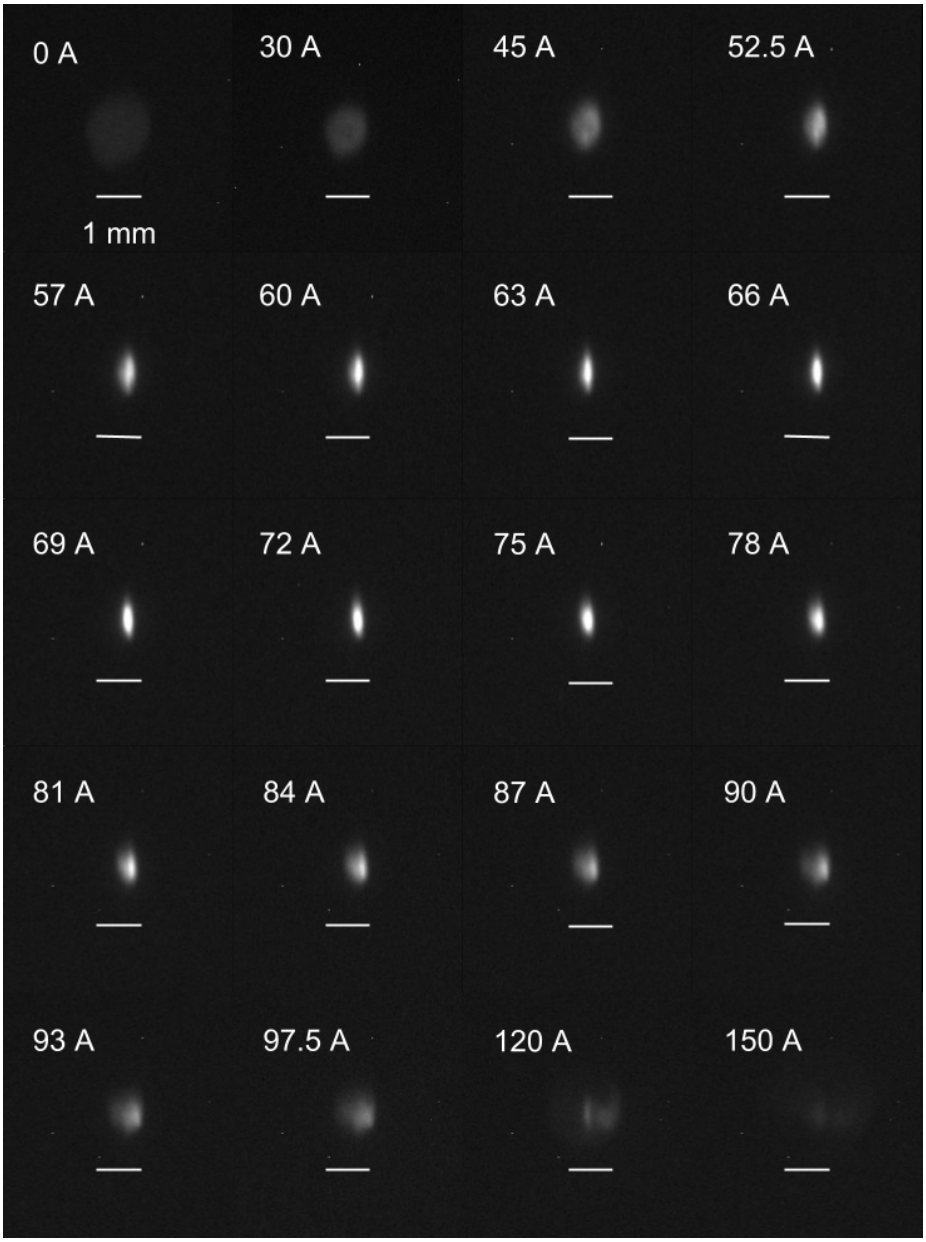

Figure 8.13: CCD images of an imaged 100 µm slit coming into and out of focus as the magnetic lens current is increased. The narrowest image measured has a width of 150 µm and corresponds to a lens current of 66 A.

There are multiple factors at play that limit the effectiveness of the imaging system. The first is the 150 µm resolution limit of the detector. Even if our beam width was smaller than 150 µm, we would have no means of detecting changes below the 150 µm limit.

A second form of error is chromatic aberration resulting from the nonuniform speeds of the beam. The focal length of the magnetic lens is proportional to the square of the speeds of the atoms travelling through the lens.

A third form of error is geometric aberration stemming from both fringe fields outside the lens and deviations from the ideal hexapole field inside the lens. While it is difficult to see the effects of the fringing fields, we can pinpoint the effects of deviations from the ideal hexapole field.

Figure 8.13 shows CCD images of the imaged slit coming into and out of focus as the lens current is varied. In several of the out of focus images, the reader can clearly see two distinct bright spots on the camera. These bright spots are an artifact of the splitting of the magnetic field zero within the hexapole lens. Recalling from Section 6.2, when there is either a background magnetic field within the hexapole, or the position of one or more of the lens rods deviates slightly from its ideal position, there will be two regions of minimum magnetic field strength within the hexapole field. When atoms pass through a lens with a slight deviation from the ideal hexapole field, they will be imaged to two distinct spots, rather than a single image.

We rectify this aberration by applying a small background field on the order of 1-10 Gauss using two sets of Helmholtz coils whose axes are transverse to both the atomic beam and each other. We optimize the applied magnetic bias field by optimizing the image size and shape when the imaged slit is in focus on the MCP.

The reader can see that there appears to only be a single peak for lens currents near the ideal current of 66-69 A, however the double peak phenomena re-emerges for values of current far from the ideal current. This implies that the Helmholtz coils have mitigated, but not eliminated the problem of geometric aberration.

8.3.2 Long propagation length, long focal length

The next case we analyze is focusing a beam that has been brightened by means of our permanent magnetic hexapole and transverse cooling, but is not shaped by a slit or any other aperture. In this case, the beam freely propagates a distance of 107 cm

from the collimation region to the magnetic lens and is focused onto an MCP and phosphor screen 42 cm downstream from the lens. The only aperture the brightened beam is subject to is the 1/16 in. inner bore of the adjustable hexapole lens tube.

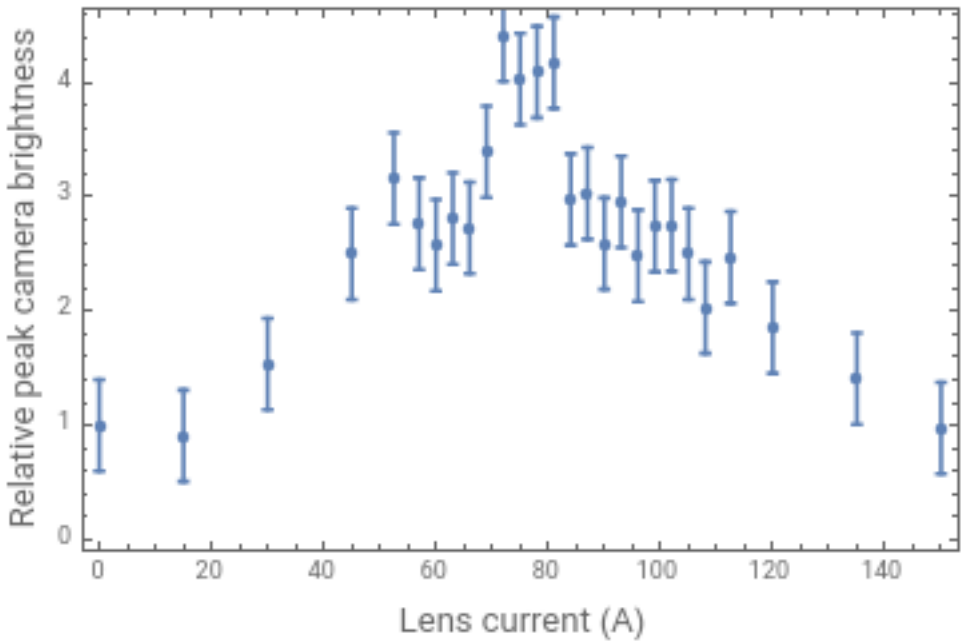

Figure 8.14: The relative brightness of a focused beam with respect to lens current. This beam propagated 107 cm from the collimation region to the lens and another 42 cm from the lens to the MCP. The beam is not defined by any aperture other than the lens tube. The inconsistency of the brightness of each data point can probably be chalked up to the poor mood of the laser system and nozzle while this data was taken.

Focusing the beam only results in an increase in peak beam density by a factor of four. This checks out as our expected spot width is roughly half the width of a non-focused beam, corresponding a decrease in total area of a factor of four. The relative beam density and spot size as functions of lens current are shown in Figures 8.14 and 8.15 respectively.

In this case, we can estimate the final expected spot size by one of two methods. The first method is the same geometric argument that we made in the case of imaging a slit, $M = \frac{i}{o}$. I refer to this estimation method as the imaging picture. Because there is no aperture at the object plane, the object size is somewhat poorly defined. We assume that the object size is roughly the size of the lens aperture 1.5 mm and

the object distance is the distance from the collimation region to the adjustable electromagnetic lens. This gives an expected spot width of $w \approx \frac{1.5\,\text{mm} \times 42\,\text{cm}}{107\,\text{cm}} \approx 590\,\mu\text{m}$.

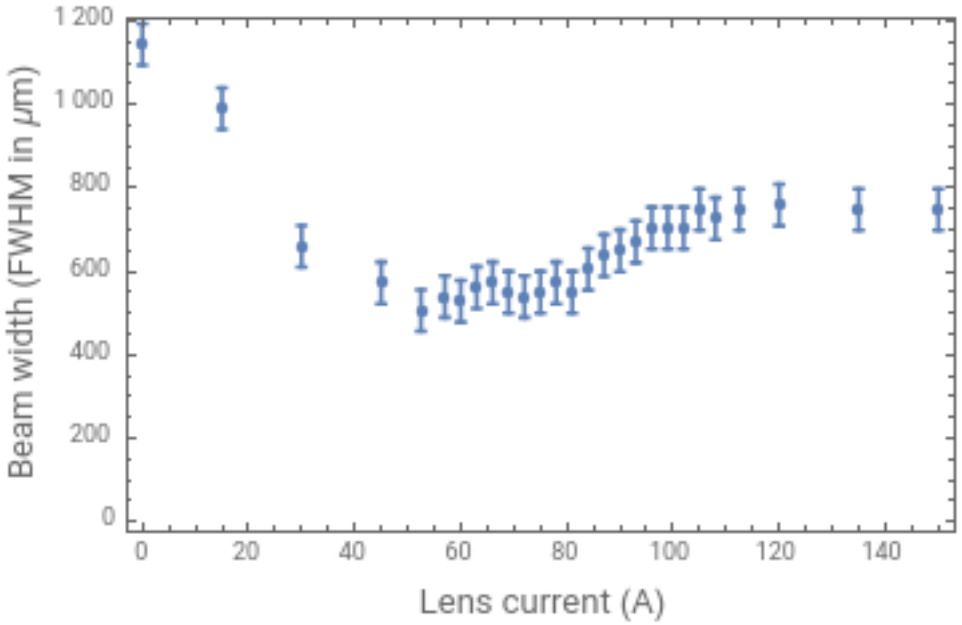

Figure 8.15: The FWHM of the focused beam with respect to lens current. The measured image distance is 42 cm and the distance from the collimation region to the lens is 107 cm. The minimum beam width is 506 µm FWHM.

The second method we use to estimate an expected spot is based off the assumption that the beam is highly collimated, which is true up to the Doppler limit. Any deviations from a perfectly collimated beam can be treated by estimating their first order effect. I refer to this estimation method as the focusing picture.

For a perfectly collimated and monochromatic beam, we would expect the beam to come to focus at a single point, regardless of the initial width of the beam. We estimate the deviation from this zero spot size by multiplying the divergence angle of the beam times the propagation distance from the lens to the image plane.

Using data from the beam brightening measurements, we estimate this divergence angle to be $\frac{1.9\,\text{mm}}{102\,\text{cm}} \approx 1.9\,\text{mrad}$.

Using this approximation, the expected spot size will therefore be given by

$$w_{\text{expected}} \approx \frac{1.9\,\text{mm}}{102\,\text{cm}} \times 42\,\text{cm} \approx 780\,\mu\text{m}. \tag{8.21}$$

Our measured minimum spot size of 506 µm beats both of those approximations, meaning either we're really good at focusing or there are other dynamics at play. I would posit the latter.

Both these methods set an upper bound on the expected size of the beam. The first method using arguments from geometric arguments is based on the assumption that the beam is highly divergent, when in reality it is nearly collimated. The second argument assumes that the beam has a large transverse extent, when in reality, it is less than 2 mm wide. Neither argument tells the whole picture, implying that we are in a hybrid regime between imaging an object and focusing a collimated beam, as discussed in Section 7.6.

8.3.3 Long propagation length, short image length

We next analyze the case of a freely propagating beam, similar in all respects to that analyzed in the previous section, but with image distance 13.5 cm. The beam propagates a distance of 107 cm from the collimation region to the magnetic lens and is focused onto an MCP and phosphor screen 13.5 cm downstream from the lens. Again, the only aperture the brightened beam is subject to is the 1/16 in. inner bore of the adjustable hexapole lens tube.

The relative beam density increases by a factor of nine when the atoms are focused onto the detector. This is a better ratio than the long image distance case. While a smaller ratio than the peak beam density increase when using a slit, this corresponds to significantly more total atoms as no atoms are being blocked by the slit. The relative beam density and spot size as functions of lens current are shown in Figures 8.16 and 8.17 respectively. The raw images are shown in Figure 8.18.

One factor limiting the peak beam density is pressure buildup within the lens tube. When high currents are applied to the lens, the PEEK lens tube heats up and outgasses, limiting the total flux of the beam. Future iterations of this project will use glass or another non-outgassing material as a lens tube.

We notice the beam is brightest and narrowest for a lens current of 159 A. This corresponds to a focal length of 13.9 cm, very similar to the image distance of 13.5 cm.

In the focusing picture, we expect a final spot size given by the product of the divergence angle and the image distance:

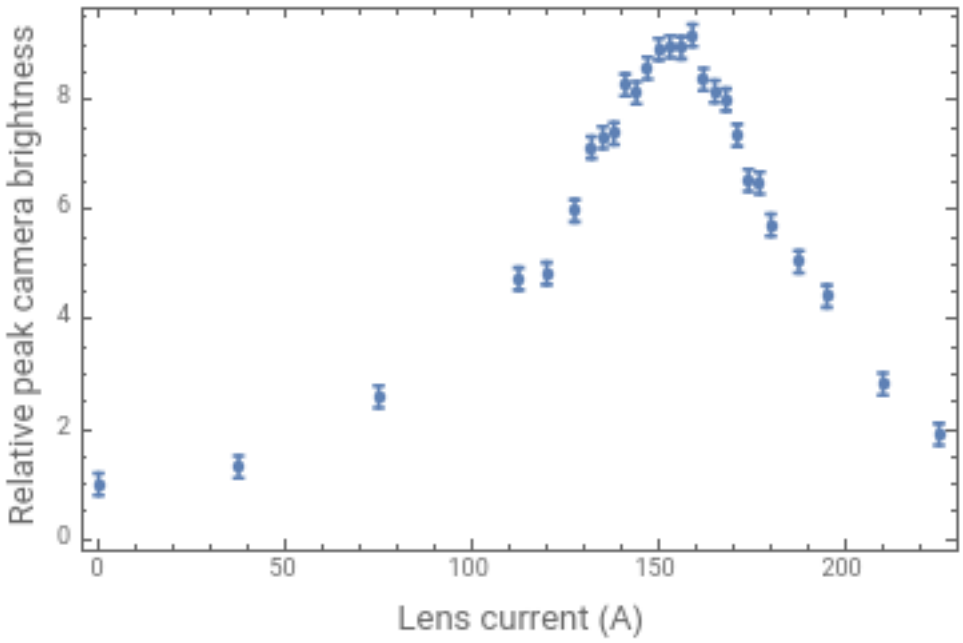

Figure 8.16: The relative brightness of an imaged slit with respect to lens current. The measured image distance is 13.5 cm and the distance from the collimation region to the lens is 107 cm.

$$w_{\text{expected}} \approx 1.9\,\text{mrad} \times 13.5\,\text{cm} \approx 256\,\mu\text{m}. \tag{8.22}$$

In the imaging picture, assuming an object size of 1.5 mm, an object distance of 107 cm and an image distance of 13.5 cm, we would get an expected image width of

$$w_{\text{expected}} \approx 1.5\frac{13.5\,\text{cm}}{107\,\text{cm}} \approx 189\,\mu\text{m}. \tag{8.23}$$

As our beam is larger than the upper bound set by the imaging picture, we know that aberrations play a role in limiting our spot size.

8.3.4 Short propagation length, short image length

The final case for which we test our adjustable magnetic hexapole lens in the pseudo-DC mode is with a propagation length of 37 cm and an image length of 13.5 cm.

The benefits of using a short object distance are twofold. First, the shorter propagation distance allows for more atoms to pass through the lens. Second, it requires less space on an optical table. This will be a major factor when more lenses and beam

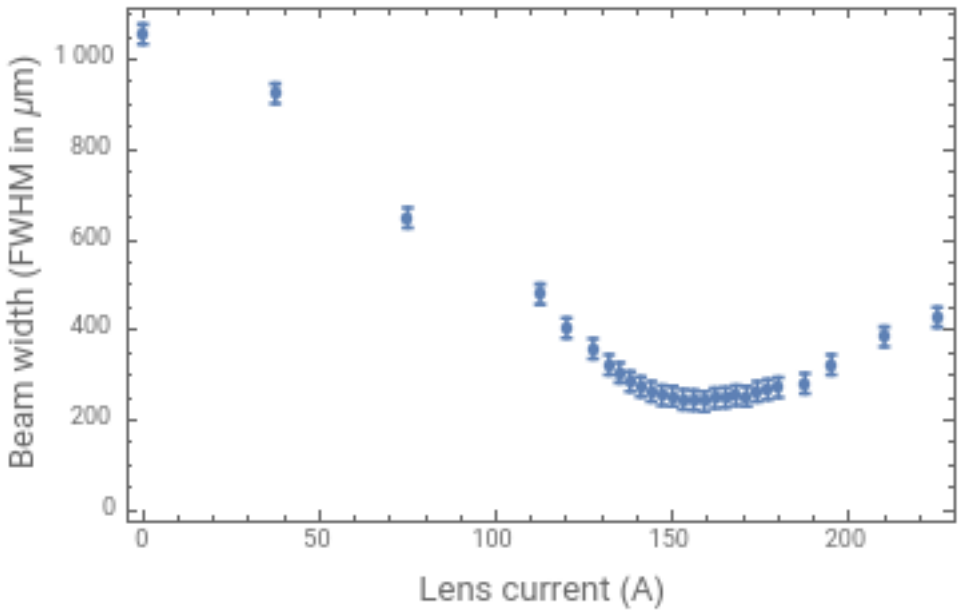

Figure 8.17: The FWHM of the focused beam with respect to lens current. The measured image distance is 13.5 cm and the distance from the collimation region to the lens is 107 cm. The minimum beam width is 242 µm FWHM.

brightening stages are added to the beamline. The drawback is the larger spot size due to the shorter object distance.

While the peak beam density increases by a factor of five for the short focal length versus a factor of nine, for the longer focal local length, this is actually an increase in peak atom density as more atoms pass through the bore of the lens. We estimate a beam density of $5 \times 10^{13}\,\mathrm{cm}^{-2}\,\mathrm{s}^{-1}$. The relative beam density and spot size as functions of lens current are shown in Figures 8.19 and 8.20 respectively.

The peak beam density and minimum spot size of 510 µm both occur with a lens current of 168 A. This corresponds to an estimated focal length of 13.2 cm, close to the image distance of 13.5 cm. It makes sense that a slightly higher lens power is needed for the short object length case as the effective divergence angle is larger for short object lengths.

In the focusing picture, the expected spot size does not depend on object length, so therefore the upper bound for the spot size remains 256 µm. Aberrations prevent us from reaching this limit.

In the imaging picture, we expect a spot size given by

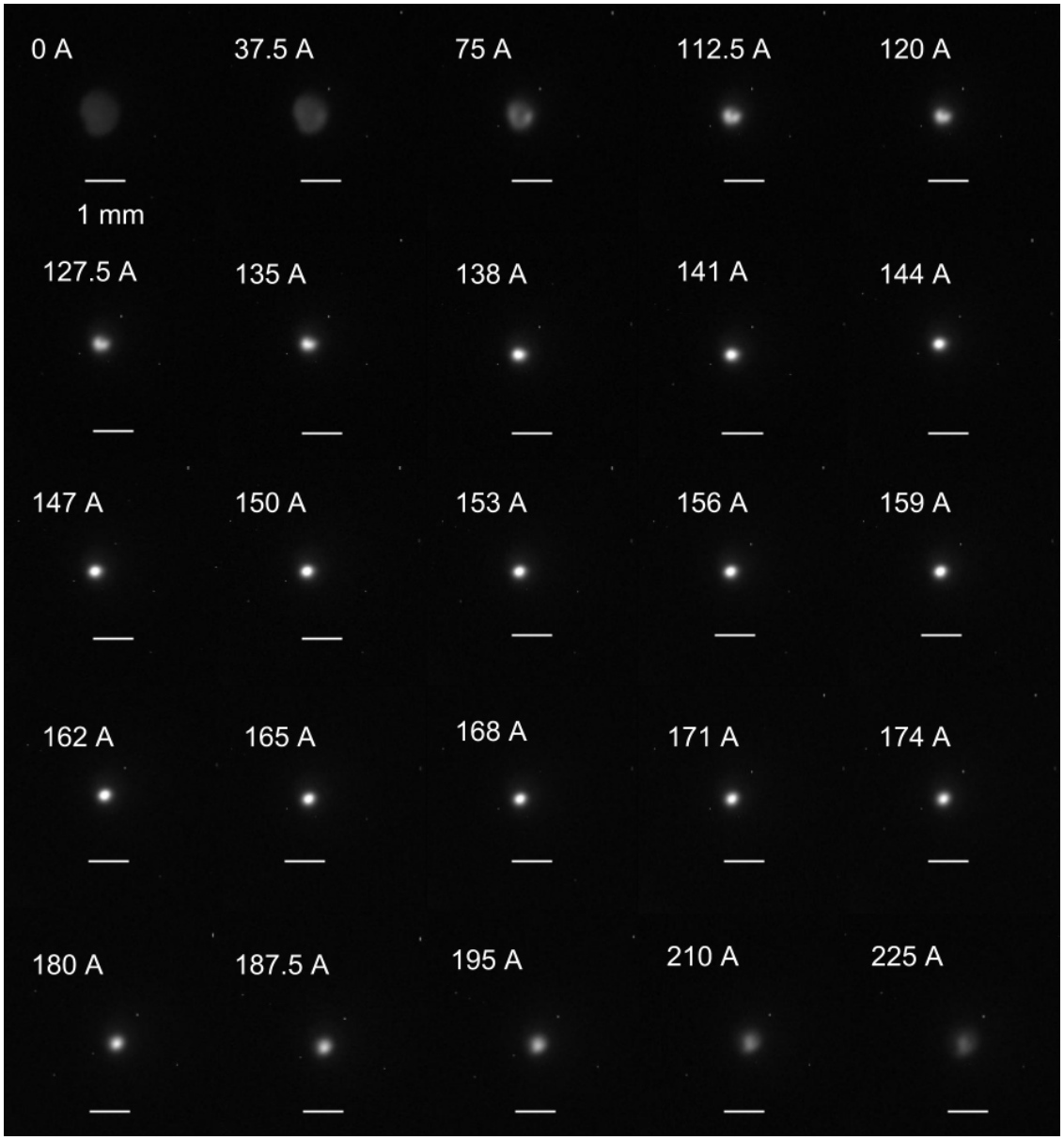

Figure 8.18: CCD images of focused beam coming into and out of of focus as the magnetic lens current is increased. The narrowest image measured has a width of 242 µm and corresponds to a lens current of 159 A.

$$w_{\text{expected}} \approx 1.5\,\text{mm}\frac{13.5\,\text{cm}}{37\,\text{cm}} \approx 547\,\mu\text{m}. \tag{8.24}$$

As the expected spot size is much smaller in the focusing regime, this picture is a much more realistic picture for the dynamics of the beam.

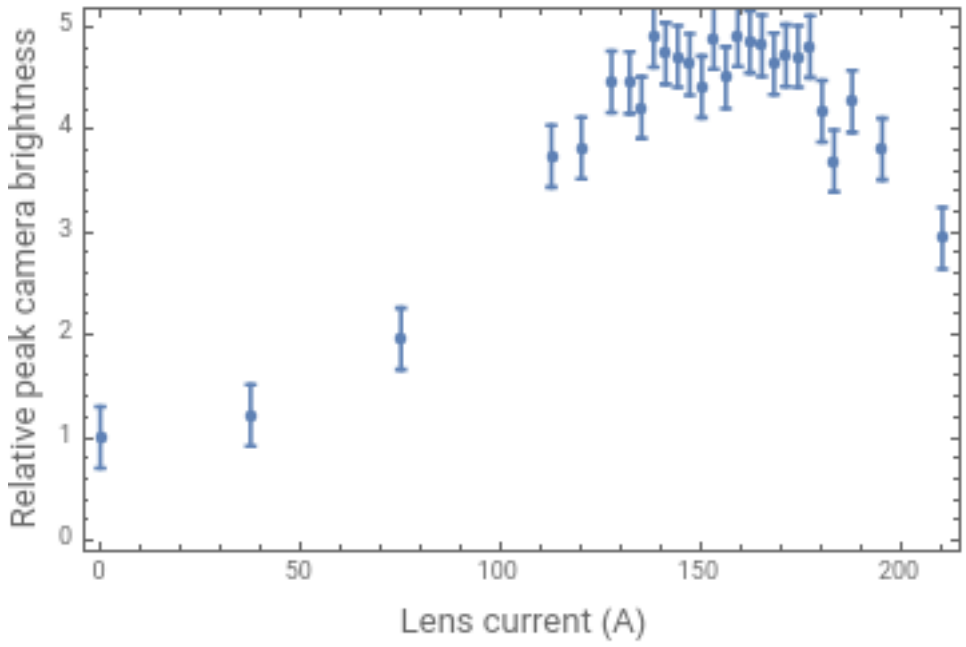

Figure 8.19: The relative brightness of an imaged slit with respect to lens current. The measured image distance is 13.5 cm and the distance from the collimation region to the lens is 37 cm. Similar to the case of the long object and long image distance, the nozzle and laser were in bad moods when this data was taken.

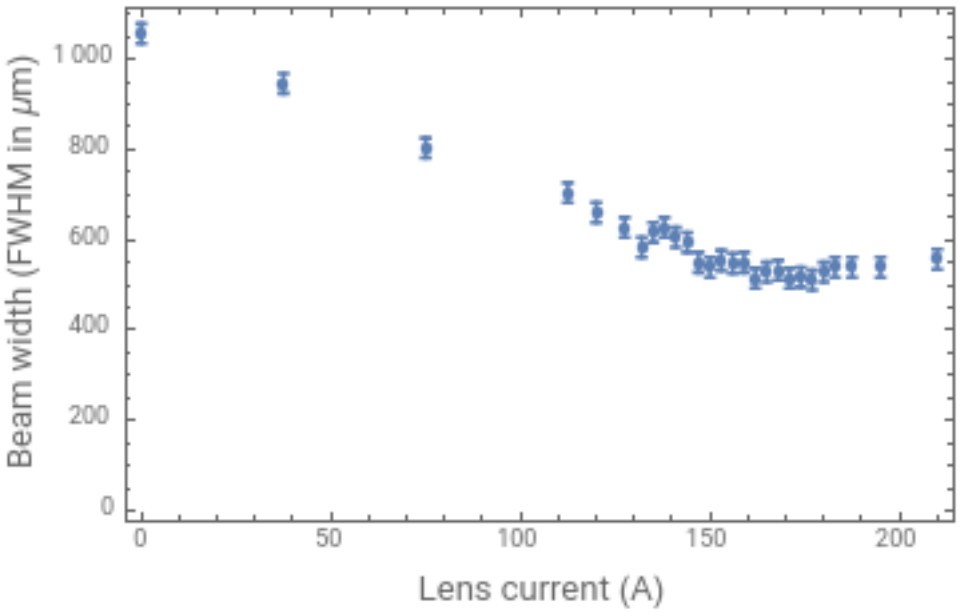

Figure 8.20: The FWHM of the focused beam with respect to lens current. The measured image distance is 13.5 cm and the distance from the collimation region to the lens is 37 cm. The minimum beam width is 510 µm FWHM.

Chapter Nine: Summary and future work

Metastable atom electron spectroscopy has shown great promise as a means of spectroscopically probing two-dimensional surfaces in a surface sensitive, non-damaging manner. Compared with electron and photon based spectroscopy methods, metastable atoms have much lower kinetic energies and shorter deBroglie wavelegths, allowing for truly surface sensitive spectroscopy without probing the bulk states of a sample.

To this point, a major limitation of metastable atoms as a tool for microscopy has been the lack of a bright, high-flux, high-resolution source of metastable atoms. In this dissertaion, I presented and demonstrated initial progress on a scheme of metastable atom beam brightening and focusing that paves the way towards true nanoscale atomic focusing, which will realize the potential of neutral atom microscopy.

9.1 Summary of work

Over the course of the experiment, we have designed, built and tested our scheme for atomic beam brightening and focusing, which showed an increase in beam brightness over an unadulterated supersonic beam by a factor of twenty and a detector resolution limited spot size of 150 µm.

We have optimized a pulsed supersonic Even-Lavie valve with a dielectric barrier discharge to create a sub-Kelvin beam of metastable neon atoms.

We then used a method of single beam longitudinal cooling to slow and cool the beam to a longitudinal temperature below 50 mK. We then spin polarized the beam to the low field seeking $m_j = 2$ magnetic state using standard methods of optical pumping.

We passed this spin polarized atomic beam through a permanent magnetic hexapole lens. We demonstrated that this lens was able to focus the divergent beam from an initial spot size of 6.4 mm FWHM to a final spot size of 1.5 mm FWHM.

At the image plane of the permanent magnetic hexapole lens, we collimated the converging atomic beam using standard methods of transverse laser cooling. We achieved near-Doppler limited collimation corresponding to a velocity distribution of

$93\,\mathrm{cm\,s^{-1}}$ FWHM compared to a Doppler limit of $71\,\mathrm{cm\,s^{-1}}$ FWHM. This focusing and collimation corresponds to a 20-fold increase in beam brightness.

We demonstrated the effectiveness of our adjustable electromagnetic hexapole lens both by imaging a small slit and by focusing our brightened beam without an aperture. While imaging the slit, we demonstrated a detection limited minimum spot size of 150 µm. When we focused our beam without a slit, we demonstrated a minimum spot size of 242 µm. By reducing the object distance from 107 cm to 37 cm, we noted an increase in the spot size of our beam to 506 µm, but also a twofold increase in peak beam density over the long object case.

9.2 Future directions

While we have demonstrated the ability of a complex atom lens to brighten and focus an atomic beam, we have not yet created a beam capable of realizing the promise of nanoscale neutral atom microscopy. In order to reach the beam brightness, beam density and spatial resolution necessary for neutral atom microscopy, we must continue to upgrade and develop our complex atom lens.

9.2.1 A more complex lens

In principle, there is no reason our beam brightening and focusing scheme needs to be limited to two lenses. Our method can be repeated several times in series to increase the brightness of our atomic beam. In practice, this amounts to employing a second round of laser cooling at the focus of the adjustable electromagnetic lens, followed by a propagation distance to another magnetic lens, followed by further rounds of transverse cooling and magnetic focusing until the desired brightness and resolution are reached.

When analyzing beam focusing for a short and long object distance, we found that we achieved a higher density beam for a shorter object length. This result will not hold for downstream lenses as the initial spot size will be significantly smaller than the bore of the lens. Longer object lengths will be necessary as we will be in the imaging a finite object regime rather than focusing a nearly collimated beam regime as discussed in section 7.6.

This gives us a maximum spatial demagnification ratio equal to the image distance divided by the object distance.

9.2.2 Aberration correction

Future lenses downstream in the beamline will be slightly tapered so as to account for chromatic aberration. The six tungsten rods will each be anchored at a fixed distance from the axis of the magnetic lens at the lens output, but will be a further, adjustable distance from the lens axis at the lens input. The angle will be such that the atoms toward the back of the atomic pulse will feel a weaker focusing force than atoms at the front of the pulse, allowing atoms at both the front and back of the atomic pulse to be focused to the same focal plane. In Section 6.3, we calculated the focal length for a pulsed electromagnetic hexapole with no taper to be

$$f \approx \frac{\pi a^3 m v_z}{18 \mu_0 \mu_B I \tau}. \tag{9.1}$$

When we add in the taper, both the focal length and lens radius will be functions of z, where z is the position within the magnetic lens. The zero point is arbitrary. In order for atoms longitudinally separated by a distance Δz, to both focus at the same plane, their focal lengths must also differ by Δz in order to offset their longitudinal separation. This implies that the derivative of the effective focal length $\frac{\partial f}{\partial z} = -1$.

$$\frac{\partial f}{\partial z} = -1 \approx \frac{\pi 3 a(z)^2 \frac{\partial a}{\partial z} m v_z}{18 \mu_0 \mu_B I \tau}. \tag{9.2}$$

The derivative of the radius a with respect to longitudinal position z corresponds to the taper angle in radians,

$$\frac{\partial a}{\partial z} \approx -\frac{6 \mu_0 \mu_B I \tau}{\pi a_0^2 m v_z} \approx \frac{a_0}{3 f_0}, \tag{9.3}$$

where a_0 and f_0 are the radius and focal length of a non-tapered lens.

For a focal length of 10 cm and lens radius of $3/32\,in. \approx 2.38\,\mathrm{mm}$, the ideal taper angle will be given by

$$\alpha \approx 7.94\,\mathrm{mrad} \approx 0.455^\circ. \tag{9.4}$$

This gives us a first order approximation for the ideal angle at which to taper our pulsed electromagnetic lens so as to reduce chromatic aberration by focusing all atoms to the same focal plane regardless of their longitudinal position.

9.2.3 Longitudinal electromagnetic hexapole

In order for the first order approximation for the ideal taper angle to be valid, the longitudinal extent of the atomic beam must be sufficiently small. To this point, we have shown that we can slow the longitudinal expansion of an atomic beam through Doppler cooling, however we have not shown a method for reducing the extent of the beam below its initial length.

In Subsection 4.1.1.4, we analyzed a configuration of three coaxial coils with current flowing in alternating directions, the current of the middle coil with current $16/(7\sqrt{7})$ times that of the outer coils, each separated by a distance $\sqrt{3}/2$ times their radii:

$$B_z = \frac{972\mu_0 I z^2}{343\sqrt{7}r^3}, \tag{9.5}$$

This gives a longitudinal force on atoms of

$$F_z \approx -\frac{5832\mu_0 I z \mu_B}{343\sqrt{7}r^3} \tag{9.6}$$

This harmonic force profile has the same form as that of the permanent magnetic hexapole lens and that of the adjustable magnetic hexapole lens, except atoms passing through the set of coaxial coils will feel a longitudinal force proportional to the longitudinal position rather than a transverse force proportional to their longitudinal position. This serves as a lens that can focus the atomic beam in the longitudinal dimension rather than in the transverse dimension, thus shortening the longitudinal extent of the beam. This lens will be pulsed for a time τ such that the magnetic field will only be nonzero when atoms are entirely within the range of the outermost coils. They will feel an impulse given by $\Delta p_z = F_z \times \tau$.

Using arguments similar to those made in Section 5.2 and Section 6.3, we can use this parabolic magnetic field to calculate an equation for the focal length of this longitudinal magnetic hexapole as a lens:

$$f = -\frac{m v_z z}{F_z \times \tau}. \tag{9.7}$$

$$f \approx \frac{mv_z 343\sqrt{7}r^3}{5832\mu_0 I \mu_B \tau}. \tag{9.8}$$

As the atomic beam must be fully inside the range of the outer coils for the duration of the pulse, the maximum pulse time is on the order of r/v_z, and the minimum coil radius is 1 cm, giving a minimum focal length of

$$f \approx \frac{m343\sqrt{7}r^2}{5832\mu_0 I \mu_B}. \tag{9.9}$$

For coils with 5000 Amp-turns in the outer coils, this gives a focal length of 2.14 m. The current can be adjusted such that the focus of the longitudinal magnetic hexapole is at the same plane as the focus of the final adjustable, tapered, magnetic hexapole. The longitudinal hexapole would be placed immediately prior to transverse cooling as shown in Figure 9.1. Any transverse forces that arise due to the longitudinal magnetic hexapole would be mitigated by the ensuing transverse cooling.

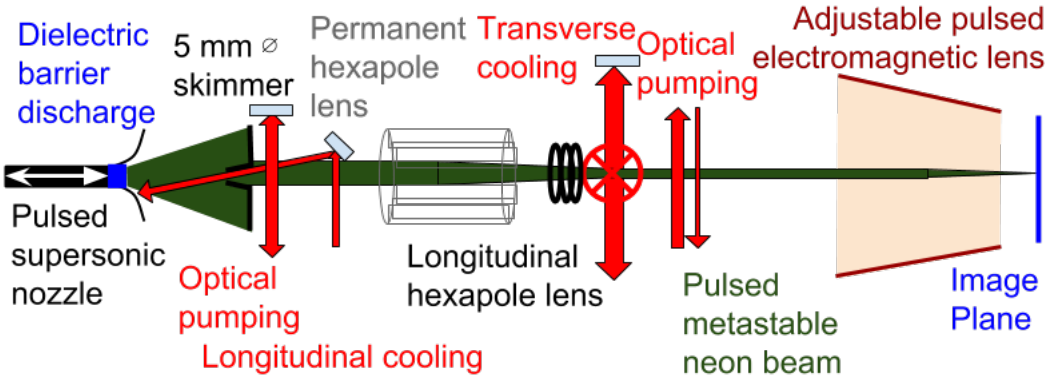

Figure 9.1: A diagram of the beamline including a longitudinal magnetic hexapole lens

This longitudinal focusing will reduce the longitudinal extent of the beam, thus reducing the amount of chromatic aberration that the tapered lens must overcome.

9.2.4 Particle detection

For all measurements presented in this dissertation, we have used an MCP with phosphor screen to measure beam density and size. As this gives us a two dimensional picture of the beam, it is a rather convenient method of detection, however the

resolution of the system is fundamentally limited. Each microchannel of the MCP is ten microns wide. Additionally, there is a 1 mm gap between the MCP and the phosphor screen. As the electrons propagate across this gap from the MCP to the phosphor screen, space charging effects will further smear the electron beams by an additional 25 µm-50 µm. The Apogee Alta CCD camera that we use is limited to roughly 50 µm in resolution. All told, these sources add up to a fundamental resolution limit of about 150 µm.

In order to beat the 150 µm resolution limit, we need to be more creative. We plan to be more creative by employing a detection scheme relying on scanning a knife edge across the waist of the focused beam as shown in Figure 9.2.

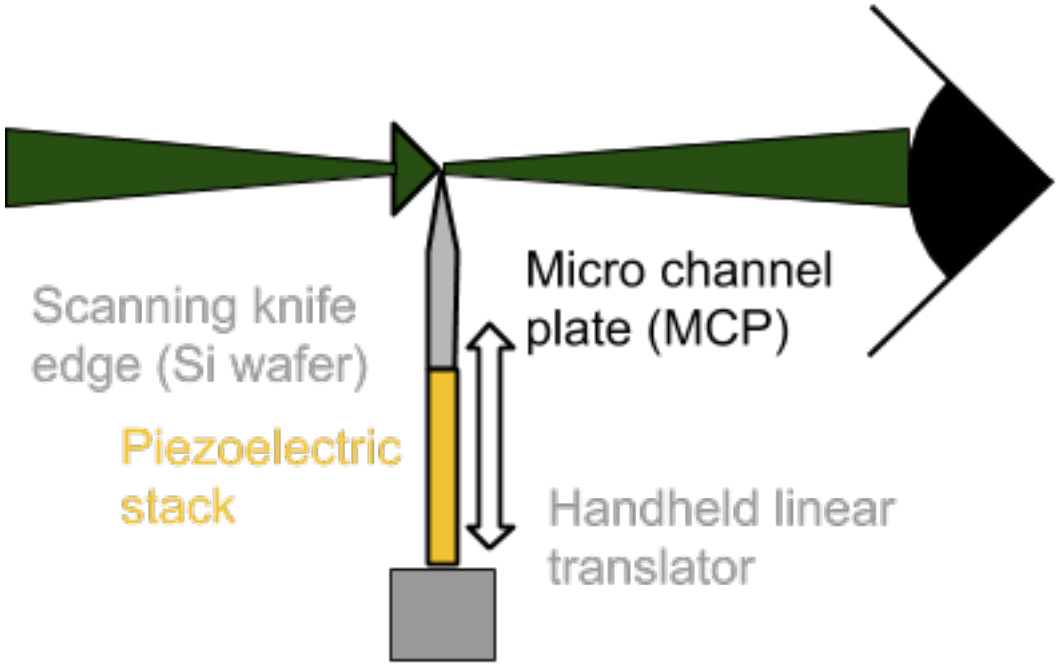

Figure 9.2: A diagram of our scheme for measuring the waist of a focused beam using a scanned knife edge.

Bibliography

[1] W. Gerlach and O. Stern, "Das magnetische moment des silberatoms," *Zeitschrift fur Physik,* vol. 9, no. 1, pp. 353355, 1922. 1

[2] W. Phillips and H. Metcalf, "Laser Deceleration of an Atomic Beam," *Physical Review Letters,* vol. 48, no. 9, pp. 596-599, 1982. 1

[3] E. Narevicius and M. Raizen, "Towards Cold Chemistry with Magnetically Decelerated Supersonic Beams." *Chemical Reviews* vol. 112, Special issue, pp. 4879-4888, 2012. 1, 43

[4] T. Mazur, B. Klappauf, and M. Raizen,"Demonstration of magnetically activated and guided isotope separation," *Nature Physics,* vol. 10, pp. 601-605, 2014. 1

[5] P. Hamilton, M. Jaffe, J. Brown, L. Maisenbacher, B. Estey, and H Müller, "Atom Interferometry in an Optical Cavity," *Physical Review Letters,* vol. 114, no. 10, pp. 100405, 2015. 1

[6] K. Liu, P. Avouris, J. Bucchignano, R. Martel, and S. Sun, "Simple fabrication scheme for sub-10 nm electrode gaps using electron-beam lithography," *Applied Physics Letters,* vol. 80, no. 5, pp. 865-867, 2002. 1

[7] L. Chang, C. Nien, J. Ye, C. Chung, V. Su, C. Wu, and C. Kuan, "A comprehensive model for sub-10 nm electron-beam patterning through the short-time and cold development," *Nanotechnology,* vol. 28, no. 42, pp. 425301, 2017. 1

[8] J. Roberts, T. Bacuita, R. Bristol, H. Cao, M. Chandhok, S. Lee, M. Leeson, T. Liang, E. Panning, B. Rice, U. Shah, M. Shell, W. Yueh, and G. Zhang, "Exposing extreme ultraviolet lithography at Intel," *Microelectronic Engineering,* vol. 83, no. 4. pp. 672-675, 2006. 1

[9] J. Courtland, "Leading Chipmakers Eye EUV Lithography to Save Moores Law," *IEEE Spectrum,* 2016, retrieved from https://spectrum.ieee.org/semiconductors/devices/leading-chipmakers-eye-euv-lithography-to-save-moores-law. 1

[10] T. Schulze, B. Brezger, P. Schmidt, R. Merterns, A. Bell, T. Pfau, and J. Mlynek, "Sub-100 nm structures by neutral atom lithography," *Microelectronic engineering,* vol. 46, special issue, pp. 105-108, 1999. 1

[11] M. Mützel, D. Haubrich, and D. Meschede, "Nanoscale focusing of atoms with a pulsed standing wave," *Applied Physics B,* vol. 70, no. 5, pp. 689-694, 2000. 1

[12] D. Meschede and H. Metcalf, "Atomic nanofabrication: atomic deposition and lithography by laser and magnetic forces," *Jounral of Physics D,* vol. 36, no. 3, pp. R17-R38, 2003. 1, 6

[13] A. Camposeo, F. Cervelli, F. Tantussi, M. Lindholdt, F. Fuso, M. Allegrini, and E. Arimondo, "Atomic nanofabrication by laser manipulation of a neutral cesium beam," *Materials Science and Engineering C ,* vol. 23 no. 6 pp. 1087-1091, 2003. 1

[14] P. Witham, "A simple approach to neutral atom microscopy," *Review of Scientific Instruments,* vol. 82, no. 10, pp. 103705, 2011. 1

[15] R. Flatabø, M. Greve, S. Eder, M. Kallane, A. Palau, K. Berggren, and B. Holst, "Atom sieve for nanometer resolution neutral helium microscopy," *Journal of Vacuum Science and Technology,* vol. 35, pp. 06G502, 2017.

[16] Y. Harada, S. Masuda, and H. Ozaki, "Electron Spectroscopy Using Metastable Atoms as Probes for Solid Surfaces," *Chemical Reviews,* vol. 97, no. 6, pp. 1879-1952. 1

[17] B. Chambers, C Neumann, A. Turchanin, C. Gibson, and G. Andersson, "The direct measurement of the electronic density of states of graphene using metastable induced electron spectroscopy," *2D Materials,* vol. 4, no. 2, pp. 025268, 2017. 1

[18] C. Adams, M. Sigel, and J. Mlynek, "Atom Optics," *Physics Reports,* vol. 240, no. 3, pp. 143-210, 1994. 1

[19] J. Gardner, R. Castillo-Garza, S. Zisman, and M. Raizen, "Manipulation of supersonic beams with static magnetic fields," *Journal of Chemical Physics,* vol. 139, no. 9, pp. 096103, 2013. 2

[20] V. Balykin, P. Borisov, V. Letokhov, P. Melentiev, S. Rudnev, A. Cherkun, A. Akimenko, P. Apel, and V. Skuratov, "Atom 'Pinhole Camera' with Nanometer Resolution," *JETP letters,* vol. 84, no. 8, pp. 544-547, 2006. 2

[21] P. Melentiev, A. Zablotskiy, D. Lapshin, E. Sheshin, A. Baturin, and V. Balykin, "Nanolithography based on an atom pinhole camera," *Nanotechnology,* vol. 20, no. 23, pp. 235301, 2009. 2, 3

[22] T. Reisinger and Bodil Holst, "Neutral atom and molecule focusing using a Fresnel zone plate," *Journal of Vacuum Science and Technology B,* vol. 26, no. 6, pp. 2374-2379, 2008. 2

[23] S. Eder, X. Guo, T. Kaltenbacher, M. Greve, and M. Kallane, L. Kipp, and B. Holst, "Focusing of a neutral helium beam with a photon-sieve structure," *Physical Review A,* vol. 91, no. 4, pp. 043608, 2015. 2, 4

[24] T. Sleator, T. Pfau, V. Balykin, and J. Mlynek "Imaging and Focusing of an Atomic Beam with a Large Period Standing Light Wave," *Applied Physics B,* vol. 54, no. 5, pp. 375-379, 1992. 2, 5

[25] J. McClelland, "Atom-optical properties of a standing-wave light field," *Journal of the Optical Society of America,* vol. 12, no. 10, pp. 1761-1768, 1995. 2

[26] W. Anderson, C. Bradley, J. McClelland, and R. Celotta, "Minimizing feature width in atom optically fabricated chromium nanostructures," *Physical Review A,* vol. 59, no. 3, pp. 2476-2485, 1999. 2

[27] T. Zhang, Y, Zhao, and C, Yin, "Laser stabilization in atom lithography based on LIF signal from the chromium beam," *Proceedings of SPIE,* vol. 9948, pp. 99480S, 2016 6

[28] W. Kaenders, F. Lison, A. Richter, R. Wynands, and D. Meschede, "Imaging with an atomic beam," *Nature,* vol. 375, no. 18, pp. 214-216, 1995. 6

[29] W. Kaenders, F. Lison, I. Muller, A. Richter, R. Wynands, and D. Meschede, "Refractive components for magnetic atom optics," *Physical Review A,* vol. 54, no. 6, pp. 5067-5075, 1996. 6, 7

[30] R. Chaustowski, V. Leung, and K. Baldwin, "Magnetic hexapole lens focusing of a metastable helium atomic beam for UV-free lithography," *Applied Physics B,* vol. 86, no. 3, pp. 491-496, 2006. 6

[31] R. Castillo-Garza, J. Gardner, S. Zisman, and M. Raizen, "Nanoscale imaging of neutral atoms with a pulsed magnetic lens," *ACS Nano,* vol. 7, no. 5, pp. 4378-4383, 2013. 7, 8

[32] J. Gardner, E. Anciaux, and M. Raizen, "Neutral atom imaging using a pulsed electromagnetic lens," *Journal of Chemical Physics,* vol. 146, no. 8, pp. 081102, 2017. 7

[33] K. Luria, N. Lavie, and U. Even, "Dielectric barrier discharge source for supersonic beams," *Review of Scientific Instruments,* vol. 80, pp. 104102, 2009. 8

[34] K. Luria, W. Christen, and U. Even, "Generation and propagation of intense supersonic beams," *The Journal of Physical Chemistry A* vol. 115, no. 25 pp. 7632-7637, 2011. 13, 102

13, 15, 17, 19

[35] M. Hillenkamp, S. Kienan, and U. Even, "Condensation limited cooling in supersonic expansions," *Journal of Chemical Physics* vol. 118, no. 19, pp. 8699-8705, 2003. 13

[36] M. Riedel, "Elastic slowing of supersonic beams," *University of Texas at Austin* 2006. 13

[37] J. Gardner, "Neutral atom imaging using a pulsed electromagnetic lens ," *University of Texas at Austin* 2016. 13

[38] C. Herrero, "Isotope effects in structural and thermodynamic properties of solid neon," *Physical Review B* vol. 65, no. 1 pp. 014112, 2001. 13

[39] Wikipedia contributors, "de Laval nozzle," *Wikipedia, the free encyclopedia,* 2008, retrieved from: https://en.wikipedia.org/wiki/De_Laval_nozzle. 15

[40] U. Even, J. Jortner, D. Noy, N. Lavie, and C. Cossart-Magos, "Cooling of large molecules below 1 K and He clusters formation," *Journal of Chemical Physics* vol. 112, no. 18 pp. 8068-8071, 2000. 15

[41] M. Zimmer, P. Spoden, T. Kraemer, G. Birkl, and W. Ertmer, "Precision measurement of the metastable $^3P_2$ lifetime of neon," *Physical Review A*, vol. 67, no. 1, pp. 010501, 2003. 24

[42] B. Brutschy and H. Haberland, "A high-intensity beam of metastable helium atoms with good velocity resolution," *Journal of Physics E*, vol. 10 no 1, pp. 90-94, 1977. 24

[43] B. Razavi, "A study of injection locking and pulling in oscillators," *IEEE Journal of Solid State Circuits,*" vol. 39, no. 9, pp. 1415-1424, 2004. 28

[44] A. Arnold, J. Wilson, and M. Boshier, "A simple extended-cavity diode laser," *Review of Scientific Instruments,* vol. 69, no. 3 pp. 1236-1239, 1998. 25

[45] W. Bennett, "Hole Burning Effects in a He-Ne Optical Maser," *Physical Review,* vol. 126. no. 2, pp. 580-594, 1962. 27

[46] C. Huygens, "Horologium Oscillatorium," 1673. 29

[47] Cohen-Tannoudji, C. Diu, B. and Laloë, F. "Quantum Mechanics," vol. 2, Wiley, New York, 1977. 30

[48] "Plinko," *The Price is Right Wiki,* 2018, retrieved from: http://priceisright.wikia.com/wiki/Plinko. 31

[49] D. Wineland, H. Drullinger, and F. Walls, "Radiation-Pressure Cooling of Bound Resonant Absorbers," *Physical Review Letters*, vol. 40, no. 25 pp. 1639-1642, 1978. 33

[50] M. Anderson, J. Ensher, M. Matthews, C. Wieman, and E. Cornell, "Observation of Bose-Einstein Cooling in a Dilute Atomic Vapor," *Science*, vol. 269, no. 5221 pp. 198-201, 1995. 33

[51] "The Nobel Prize in Physics 1997," *Nobel Media AB,* 2014, retrieved from: http://www.nobelprize.org/nobel_prizes/physics/laureates/1997/index.html. 33, 43

[52] "The Nobel Prize in Physics 2001," *Nobel Media AB,* 2014, retrieved from: http://www.nobelprize.org/nobel_prizes/physics/laureates/2001/index.html. 33

[53] "The Nobel Prize in Physics 2012," *Nobel Media AB* 2014, retrieved from: http://www.nobelprize.org/nobel_prizes/physics/laureates/2012/index.html. 33

[54] H. Metcalf and P. van der Straten, *Laser Cooling and Trapping,* Graduate Texts in Contemporary Physics, Springer, New York, 2001. 33

[55] J. Dalibard and C. Cohen-Tannoudji, "Laser cooling below the Doppler limit by polarization gradients," *Journal of the Optical Society of America B*, vol. 6, no. 11, pp. 2023-2045, 1989. 37

[56] M. Kasevich and S. Chu, "Laser cooling below a photon recoil with three level atoms," *Physical Review Letters*, vol. 69, no. 12, pp. 1741-1744, 1992. 37

[57] M. Raizen, D. Budker, S. Rochester, J. Narevicius, and E. Narevicius, "Magneto-Optical cooling of atoms," *Optics Letter*, vol. 39, no. 15, pp. 4502-4505, 2014. 37

[58] Kurt J. Lesker Company, "Quick connect couplings," 2018, retrieved from: https://www.lesker.com/newweb/flanges/adapters_couplings_quickconnect.cfm?pgid=0. 71, 81

[59] KJ Magnetics Inc, "Neodymium magnet physical properties," retrieved from: https://www.kjmagnetics.com/specs.asp, 2018. 71

[60] McMasterCarr, "Tungsten electrodes for aluminum and magnesium," retrieved from: https://www.mcmaster.com/tungsten-electrodes/=1byfcia, 2018. 80

[61] A. Murari and A Barzon, "Comparison of new PEEK seals with traditional helicoflex for ultra high vacuum applications," *Vacuum,* vol. 72, no. 3, pp. 327-334, 2003. 80

[62] C. Townsend, N. Edwards, C. Cooper, K. Zetie, and C. Foot, "Phase-space density in the magneto-optical trap," *Physical Review A,* vol. 52, no. 2, pp. 1423-1440, 1995. 93

[63] D. Nolte, "The tangled tale of phase space," *Physics Today,* vol. 63, no. 4, pp. 33-38, 2010. 93

[64] Del Mar Photonics, "Microchannel Plates," 2018. retrieved from: http://www.dmphotonics.com/MCP_MCPImageIntensifiers/microchannel_plates.htm. 100